ETH
Eidgenössische Technische Hochschule Zürich
Swiss Federal Institute of Technology Zurich

l'Observatoire de Paris | LERMA
Laboratoire d'Étude du Rayonnement et de la Matière en Astrophysique

Barthélémy Launet

Transition from star formation to quiescence in galaxies with SITELLE observations of Andromeda.

New analysis of the planetary nebulae population.

Master Thesis

Supervision

Prof. Dr. Marcella Carollo
Prof. Dr. Françoise Combes
Dr. Anne-Laure Melchior

March 2018

Contents

Abstract

The nature of the mechanisms governing the star formation quenching in galaxies since $z = 2$ is an open question. Low ionization emission line regions (LIERs) appear to represent the transition between star forming and quenched galaxies (the so-called 'green valley'), and might be the key to understand galaxy evolution.
We present in this work new spectral observations of Andromeda bulge region, a close-by example of a typical green valley galaxy, and therefore an ideal testbed to understand the processes at stake in LIERs. We obtained with SITELLE instrument installed at CFHT unprecedented spatial and spectral resolution on Andromeda central kiloparsec, enabling the detection of 766 Planetary Nebulae candidates (whose progenitors, post-AGB stars, are presumed to be responsible for the ionization in LIERs), confirmed with emission-line diagnostic diagrams. The analysis of the Planetary Nebulae Luminosity Function (PNLF) of this extended sample shows a bimodal distribution, which seems to correlate with a separation between disc and bulge populations. Preliminary results concerning the background stellar continuum and the diffuse gas components are promising and have already led to an observation time request with LOFAR instrument.

Chapter 1

Introduction

1.1 Motivation

One striking property of large samples of galaxies is their bimodality (Driver et al., 2011; Lilly et al., 2007; York et al., 2000). Galaxies can be classified in a star forming blue cloud and in a passive red sequence. The mechanisms responsible for the star formation shutdown between the former and the latter, also called 'quenching', are actively studied. Madau and Dickinson (2014) estimate that this quenching started around $z = 2$, and two types of channels are discussed in the literature. The environment could play a key role as the quenching time and amplitude of star formation rate decrease towards higher density environments (e.g. Coenda et al., 2018). This baryon cycle of galaxies is complex. The main idea is that cool gas needed to form stars can be removed by several known plausible mechanisms, such as strangulation, harassment and ram-pressure stripping. Hatfield and Jarvis (2017) argues that most quenching is due to the halting of fresh inflows of pristine gas, as opposed to by tidal stripping. Similarly, McGee et al. (2014) argue that satellite galaxies, which could constitute one significant gas reservoirs, could be quenched by over-consumption: the interruption of the fresh gas supply may quench satellite galaxies long before stripping events occur. In parallel, the presence of supermassive black holes in the heart of galaxies, with a mass proportional to the bulge mass (Merritt et al., 2001), could also be related to the star formation efficiency through Active galactic Nucleus (AGN) feedback. Alternatively, the star formation activity could slow down with the increase of the galaxy mass.

On the observational side, Belfiore et al. (2016) has shown, using spatially resolved spectroscopy on large sample of 646 local galaxies (SDSS, MANGA), that low ionization emission line regions (LIERs) are witnessing the intermediate stage of the quenching, the so-called 'green valley'. It is discussed that contrary to star forming regions, the gas is not heated by hot stars but rather by post-asymptotic giant branch (AGB) stars.

A correlation between the specific star formation rate and the Active Galactic Nucleus (AGN) luminosity has been found (e.g. Barrows et al., 2017), and positive feedback from an AGN (e.g Concas et al., 2017), can reduce the central star formation of a galaxy Woo et al. (2017). Kaviraj et al. (2015) also showed on 550 nearby galaxies that the AGN is unlikely to regulate the star formation for galaxies in the green valley. Fang et al. (2013) discuss the quenching as an interplay between the inner structure of a galaxy and its surrounding dark matter halo. Fraser-McKelvie et al. (2018) conclude that the quenching results most probably from a mixture of mechanisms related to their internal structure and

galactic environment, as also discussed by Carnall et al. (2017).
What triggers quenching ? And what are the dominating mechanisms responsible for the LIER ionization ?

1.2 Andromeda as a local testbed

Located at 780 kpc (de Grijs and Bono, 2014), Andromeda is a typical example of a green valley galaxy in the Local Group, with a significant bulge showing a central LIER (Mutch et al., 2011). It is an ideal testbed to analyze and understand star formation quenching in galaxies. Its proximity allows to get great spatial coverage of the phenomena at stake and to conduct detailed analysis of the contribution of the different mechanisms to the gas ionization.
Despite a long-lived study, many questions are still left unanswered about M31 stellar substructures and how it has formed. The nucleus first observed double (Lauer et al., 1993), is now known to host an inner eccentric disk with a super-massive black hole of $\sim 1 - 3 \times 10^8 M_\odot$ Bender et al. (2005). The bulge has been classified as a "classical bulge with pseudobulge trimmings" by Mould (2013), but other studies argue for a barred bulge (Beaton et al., 2007; Opitsch et al., 2017). M31 neighborhood is populated by many relics of past interactions (McConnachie et al., 2009), and the kinematics are difficult to disentangle.
Concerning star formation history, the bulge is considered as mostly old ($\geq$12 Gyr, Saglia et al., 2010), but might host some recent star formation events, possibly from minor-mergers (Saglia et al., 2010). There is no obvious HII regions above the spatial resolution. However, there are molecular gas clumps in the region following approximately the dust emission (Melchior and Combes, 2011, 2016). Dong et al. (2015) discuss the possible presence of a 300 Myr-1 Gyr stellar population which could contribute to 2% of the stellar light in this region.
Beside the presence of a supermassive black hole, no clue for recent AGN activity has been observed to date, but Melchior and Combes (2017) observed holes in the gas distribution close to the Black Hole that could mark a feedback mechanism.
A close spectroscopic study of M31's bulge is needed to disentangle these phenomena.

1.3 Planetary Nebulae

According to Frew and Parker (2010) working definition, Planetary Nebulae (PNe) are descendants of low- and intermediate-mass (1–8$M_\odot$) stars at the end of the AGB phase. They consists of a shell of gas (the previously expelled envelope) of usually radius $\leq$ 1.5 pc, ionized by a central star becoming a white dwarf (WD). As Belfiore et al. (2016) discussed, the ionization sources in LINER galaxies are probably post-AGB stars, i.e. precisely the progenitors of PNe. By understanding their population, one can constrain post-AGB star populations and thus estimate their contribution to the ionization in LINERs. They show strong characteristic emission lines, particularly [OIII]5007 and [OIII]4959 emission-lines, which make them fairly easy to detect. They have been therefore extensively studied throughout objects from the Local Group (Parker et al. (2006) in the Galaxy, Reid and Parker (2010) in the Large Magellanic Cloud (LMC), Jacoby and De Marco (2002) in the Small Magellanic Cloud (SMC), Leisy et al. (2005) in NGC 6822).

According to Merrett et al. (2006), PNe are excellent tracers of the overall stellar population of a galaxy, as their transition from the Red Giant Branch (RGB) is quite rapid ($\leq 10^5$ yr, Frew and Parker (2010)). With their strong emission lines, they are ideal to probe kinematics, and thus investigate the structure of a galaxy; for example Merrett et al. (2006) has used PNe to identify stellar streams in M31 neighborhood. With a large enough sample of PNe, Halliday et al. (2006) discuss the ability to efficiently reconstruct the full galaxy gravitational potential, which can help calibrating micro-lensing studies.
There is an observational consensus on the absolute magnitude of the bright-end cutoff of the [OIII]5007 Planetary Nebulae luminosity function (PNLF). Ciardullo (2012) report a value for the cutoff of $M^*_{5007} = -4.47$, surprisingly independent of age and metallicity of the population considered. It has even proved its efficiency as a distance indicator, with a precision of about $\sim 10\%$ (Ciardullo, 2010).
This is in strong contradiction with synthetic models of evolutionary tracks for PNe from the main sequence to the post-AGB phase developed by Marigo et al. (2004), which predict that progenitors of such bright PNe should have a mass of $\sim 2.5 M_\odot$, and be an indicator of a star formation event younger than ~ 1 Gyr. In parallel, the bright-end cutoff has been consistently measured in old elliptical galaxies, as well as in M31 bulge. Explaining this discrepancy would help a better constraint of evolutionary models, especially of the so called initial mass-final mass relation, hence a better understanding of the chemical enrichment of the galaxy.

1.4 Outline of the thesis

With an international collaboration, we have observed the central kpc of Andromeda with the Imaging Fourier Transform Spectrometer (iFTS) SITELLE on the Canadia-France-Hawaii Telescope (CFHT), in two different filters. The field of view (FOV) of $11' \times 11'$ covers the whole bulge area, and the unprecedented spatial sampling (pixel scale = $0.321''$), the good spectral resolution and the quality of the instrument enables to detect emission lines across the whole field, in particular Hα and Hβ, [OIII]5007 and 4959 doublet, [NII]6548 and 6583 doublet, and [SII]6716 and 6731 doublet. This mine of data provides an access to many of the key points discussed above. First, it enables access to a large population of resolved point sources, mostly PNe, and their kinematics. It also provides insights on the background stellar continuum of the galaxy, with potential constraints on its kinematics, age and metallicity, three major elements to investigate star formation. Finally, the diffuse gas of the disc extending in our FOV can be investigated, both in terms of kinematics and ionization level. Having a 2D spatial measure of line ratios, one could conduct Belfiore et al. (2016) analysis based on Baldwin, Phillips & Terlevich (Baldwin et al., 1981) diagrams and observe AGN-like, star-forming-like and LINER-like regions in the galaxy, and disentangle the different mechanisms.
We first present in Section 2 the instrument and the obtained data in details, to understand the strength and weaknesses of our observations, and we perform a careful calibration of the measures. From this calibrated data, we carry out in Section 3 a thorough analysis to detect emission-line point-like sources in the FOV, most of them being new PNe detections. Results based on this large PNe population are presented in Section 4, and we discuss preliminary results, ongoing and future work Section 5.

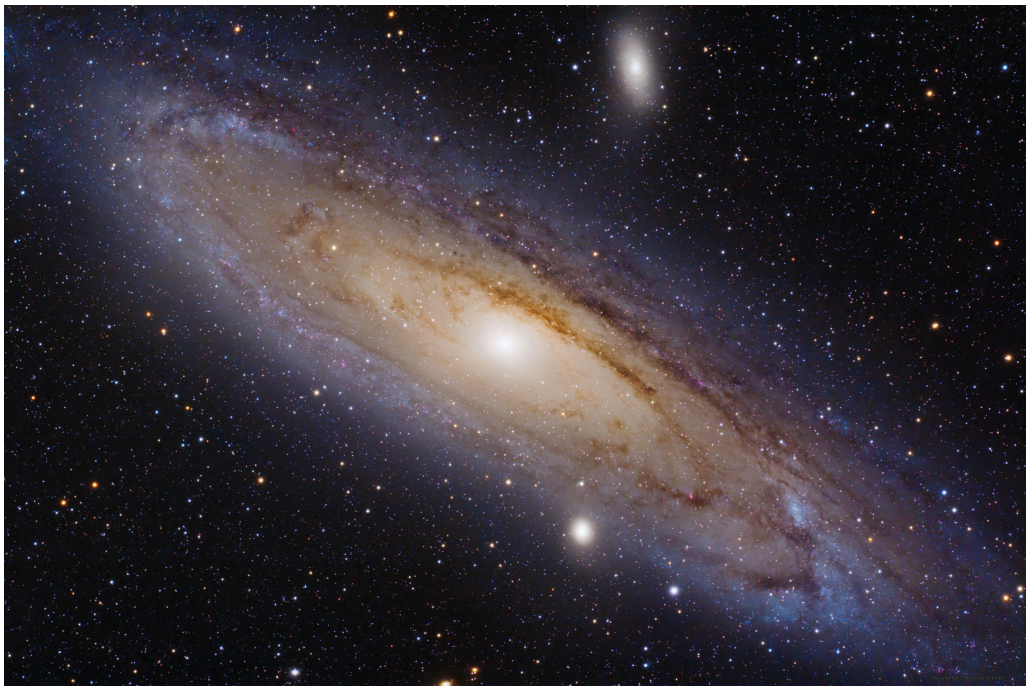

Figure 1.1: NASA picture of the day June 26, 2013 of M31, credits : Lorenzo Comolli

Chapter 2

Observations and Data reduction

2.1 SITELLE instrument

SITELLE (***S**pectromètre **I**mageur à **T**ransformée de Fourier pour l'**É**tude en **L**ong et en **L**arge de raies d'**É**mission*) is an imaging Fourier Transform Spectrometer (iFTS) installed at the Canadian French Hawaii Telescope (CFHT) since July 2015, available for scientific use since early 2016. Its $11' \times 11'$ field of view (FOV) makes this instrument one of the biggest spectra imager to date, with a pixel resolution of 0.321". The observation method is described in details in Drissen et al. (2010). Observations of M31's bulge, characterized by a strong background continuum, were quite challenging due to the so-called multiplex disadvantage of iFTS (see Section 2.1.2 and Maillard et al. (2013)). We present in this section a few of the instrument technical characteristics, affecting our data.

2.1.1 Configuration

SITELLE observation technique is based on a off-centered Michelson interfometer (see Figure 2.1). A moving mirror scans the optical path difference (OPD) and creates an interferometric pattern, recorded on two 2048 x 2048 pixels CCD detectors[1]. Both interferometric cubes are then combined to obtain at each pixel an interferogram, that is then Fourier transformed to recover more than 4 millions physical spectra. The natural unit of the spectral axis is the inverse of a distance, i.e. wavenumbers (namely, the unit is cm^{-1}). The spectral resolution of the instrument can be tuned from 2 to 10^4 as it only depends on two factors : the maximum path difference one can reach, and the number of moving steps of the mirror.

2.1.2 Technical specificities

Because of the off-centered configuration, incoming beams are not perpendicular to the planes of the CCD detectors. The path difference, i.e. the phase of the interferograms, thus depends on the incident angle of the beam at each pixel. This directly influences the spectral calibration of the spectra, as a phase shift on the interferograms directly translates into wavelength shift on the spectra. Errors on the phase of the interferograms can also be

[1]For each path difference, one image on a detector is actually the negative of the other, in the sense that due to conservation of the incoming flux from the source, a constructive interferometric pattern on one detector is observed as a destructive pattern on the other.

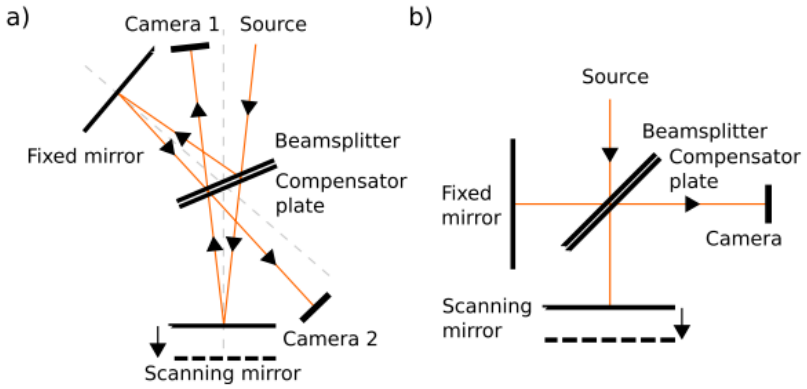

Figure 2.1: Sketch of a classical Michelson interferometer (b) and SITELLE's configuration (a), taken from Martin and Drissen (2017). The off-centering allows to recover half more flux (that would have been reflected back to the source in a classical configuration), at the cost of a pixel dependent path difference on the detectors. As discussed in the text, this path difference is subsequently corrected in the reductions pipeline.

induced by dispersive effects or bad sampling of the path difference and have been carefully studied in Martin and Drissen (2017). They can affect both the LSF (deformation) and the flux of the lines.
Moreover, as the range of mirror movement is physically limited, the sampling of the interferometric pattern is restricted to a box. When the Fourier transformation is performed, the signal is then convolved with the Fourier transform of this box, i.e. a cardinal sine function (sinc) (see Maillard et al. (2013) for details): this defines our instrumental Line Shape Function (LSF).
Last, as opposed to dispersive techniques, where the photon noise in a given spectral channel is only linked to the number of photons acquired in this channel, with interferometric techniques all photons of a source are collected in the interferogram, and the noise gets redistributed over all the channels. This is called the multiplexing disadvantage (well described in Maillard et al. (2013)), and is of great importance for us, as M31 bulge emits a very strong background continuum. To limit this noise, SITELLE has been equipped with different narrow filters to limit the bandpass.

2.1.3 Data Reduction Pipeline

The raw data, i.e. two interferometric datacubes, is fully reduced at CFHT with the ORBS software described in details in Martin et al. (2015) and Martin and Drissen (2017). First, thermal and electronic biases on the detectors are corrected. A flat-field image is obtained at the beginning of each night to correct for illumination patterns. Both cubes are then aligned using stars present in the field of view, to correct for the misalignment of the two cameras, and interferograms are combined on a pixel-to-pixel basis, correcting for variations of sky transmission during the observation.
A phase correction is then performed, to correct errors due to the incident-angle dependent path difference, mapped with the measurement of a Helium-Neon laser source at 543.5 nm, and errors due to the absolute uncertainty on the zero optical path difference. This step is critical as it can induce many different biases (line shape function deformation, incorrect

Filter	SN2	SN3
Spectral range [Å]	4825-5132	6467-6857
Observation date	29/11/2016	24/08/2016
Field of view	11'×11'	11'×11'
Pixel scale	0.321"	0.321"
Exposure time / step [s]	15.8	13.7
Step nb.	556	840
Total exposure time [h]	3.0	4.1
Spectral Resolution	$\sim$ 1800	$\sim$ 4800
Channel width at mean wavelength [km.s^{-1}]	83.0	42.0
Line width at mean wavelength [km.s^{-1}]	168.3	63.3

Table 2.1: Observation parameters.

wavelength calibration) and will be discussed throughout the calibration Section (2.3).
A discrete Fourier transformation is then performed on these phase corrected interferograms. Last, to estimate the instrumental Modulation Efficiency (ME) and obtain an absolute flux calibration, a standard star is measured right before or after the data acquisition.
The final science product is a spectral datacube of 2048 × 2064 pixels, calibrated in flux, with an intrinsic wavelength calibration but no astrometric calibration. A flux uncertainty map, representing the detection photon noise, is provided as well.

2.2 Observations of the central field of Andromeda

M31 was observed with SITELLE in two different bandpasses, first on August 24, 2016 using the SN3 filter, designed to detect Hα (6563 Å), [NII] 6548, 6583 and [SII] 6716, 6731 doublets, and second on November 29, 2016 using the SN2 filter, designed to detect Hβ (4861 Å), [OIII] 5007 and [OIII] 4959 emission lines. The filter transmission curves are presented in Figure 2.2 and Table 2.1 gather details of the observation parameters. The $11' \times 11'$ FOV was centered on M31 bulge (RA = 0h42m44.371s, DEC = 41°16'08.34", Crane et al. (1992)), displaying a projected area of +/- 1.7 kpc centered on the galaxy center.
Technical difficulties occurred at CFHT during the SN2 observations. Hence, the resolution of this cube ($\sim$ 1800) is significantly lower than requested (the initial goal was to reach $\sim$ 5000, as obtained for SN3 cube), and it introduced some phase errors and deformations (both spatially and spectrally) that we had to take into account for the analysis.
In Figure 2.3, we present maps of the total flux and of the flux uncertainty delivered by the reduction pipeline (see 2.1.3) for the two datasets, acquired with each filter SN2 and SN3. As expected, this region presents a very strong intensity gradient, which will be one of the difficulty of the subsequent analysis. Figure 2.4 displays two examples of spectra. One can recognize the shape of the filters, while the useful positions of the emission lines are indicated at the systemic velocity of Andromeda, -300 km.s^{-1}. Structures in the continuum correspond to the stellar background. The left (resp. right) panel exhibits the spectra of a strong [OIII] (resp. Hα) source. Each line displays their characteristics cardinal sine LSF.As explained in Section 2.1.2, the noise seems to be uniformly distributed along all

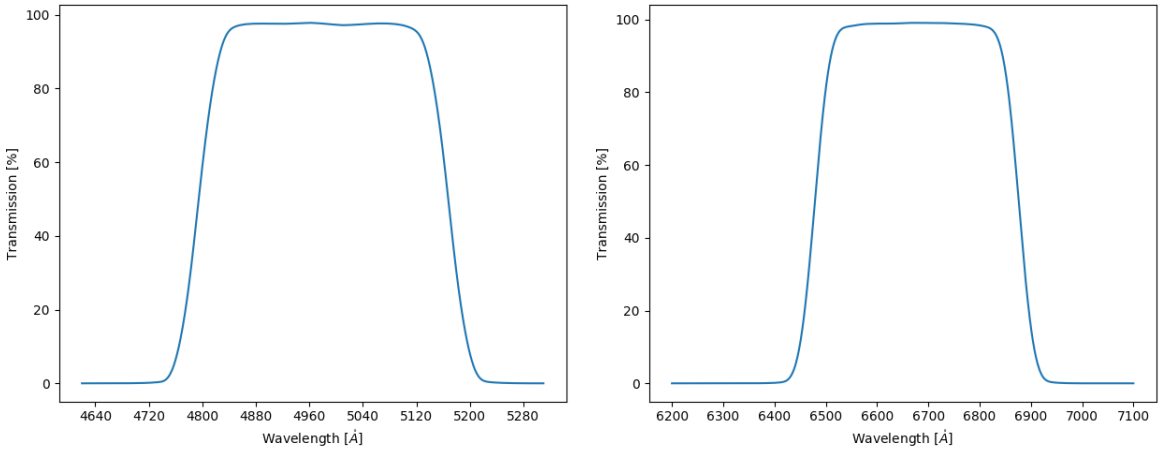

Figure 2.2: Transmission curves for the filters used with SITELLE. Left : SN2 filter, specifically designed to study Hβ (4861 Å), [OIII] 4969 and [OIII] 5007 emission lines. Right : SN3 filter, specifically designed to study Hα (6563 Å), [NII] 6548 and 6583 doublet and [SII] 6716 and 6731 doublet emission lines.

the spectral channels, even outside the bandpass of the filters.

2.3 Data Calibration

Before the beginning of this master thesis, the SN3 data cube has been calibrated and analyzed, and the procedures have been presented in details in Martin et al. (2018), hereafter Ma18. After the reduction steps performed at CFHT (see 2.1.3), a few calibration steps are still necessary. Relying on Ma18 procedures, we present in the following sections the astrometric, wavelength and flux calibrations of the SN2 datacube. They have been conducted within the ORCS software package (Martin et al., 2015), which has been supplemented for the occasion.

2.3.1 Astrometric calibration

To correct for misalignment and distortions, we followed a 3-steps astrometric calibration method as described in Ma18.
The first step re-calibrates the center of the frame and its orientation towards North, based on histogram comparison between GAIA DR1 (Gaia Collaboration, 2016) star positions and detections in the deep frame of our data. This basic calibration is not sufficient as it leads to positional errors up to 8", mostly in the corners of the field due to distortion patterns induced by the optics and structure deformations.
To correct for structural deformation of the instrument, a second calibration step adjusts a Simple Image Polynomial (SIP Shupe et al., 2005) of order 4. As suggested in Ma18, we looked for a much more crowded field (GAIA lists only $\sim 10^3$ stars in our M31 field, and we actually detect $\sim$ 400 of them). Unfortunately, no other observations have been conducted with SN2 filter during the same science run. The closest is the observation of NGC 6822 on June 30, 2017, more than 7 months later. We tried to fit a distortion model

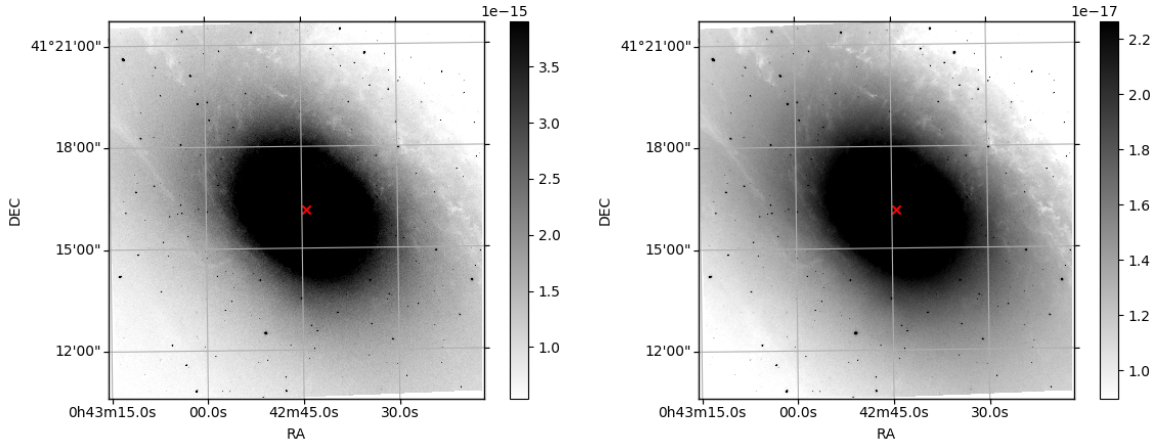

(a) SN2 Total Flux map

(b) SN2 Flux Uncertainty map

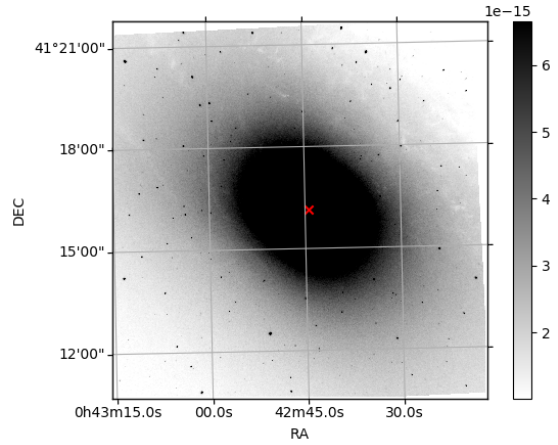

(c) SN3 Total Flux map

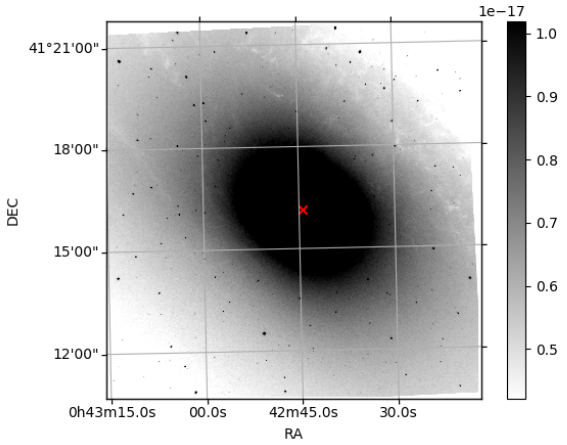

(d) SN3 Flux Uncertainty map

Figure 2.3: Maps of the total flux and flux uncertainty for each filter. Color-maps unit is erg.cm^{-2}.s^{-1}.A^{-1}. M31 center (RA = 0h42m44.37s , DEC = 41°16'08.2") is displayed as a red cross. Because of the multiplex disadvantage, the values reported on the uncertainties maps affect each spectral channel.

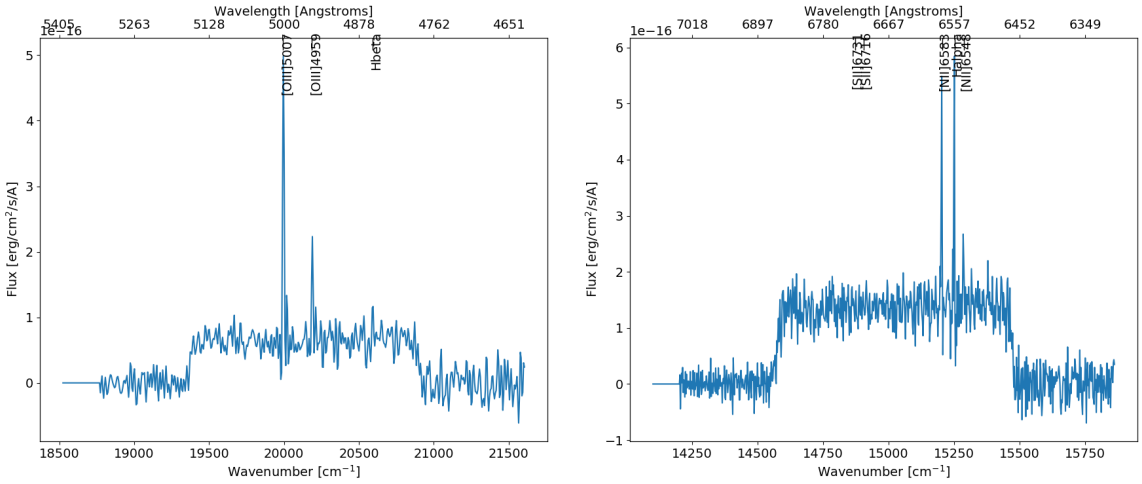

Figure 2.4: Examples of emission line spectra seen in the SN2 cube (left) and SN3 cube (right). The positions of the emission lines we are looking for are plotted, at a velocity of -300 km.s^{-1}, M31's systemic velocity. Note the natural unit of the spectral dimension, wavenumbers in cm^{-1}, due to the Fourier transformation. The conversion in Angströms is provided in the top axis. Note also the line shape of the emission lines, a cardinal sine. Finally, note how the noise impacts the whole spectrum, even outside the bandpass.

on this field and applied it to our data, but it did not correct properly the distortion bias. The instrument most likely underwent some operations (e.g. dis-mounted and re-mounted) during the 7 months gap, which changed its structure deformation. We used therefore the same GAIA stars to perform this second calibration step, reducing the maximal error to ~ 3" (median : 0.67").

Last, to reduce this error below the pixel scale (i.e. below 0.321"), we interpolated two rectangular bivariate splines (one on each axis) on the residuals between real GAIA star positions and detected positions in the cube computed with the SIP correction, to obtain two distortion maps. These maps can be included in ORCS methods to compute the position, but cannot be represented in a classical FITS header (Greisen and Calabretta, 2002). This last step lowers the median error on the position to 0.17". Figure 2.5 shows the error distribution at each step, corresponding to different levels of refinement, and Figure 2.6 shows an excerpt of the deep frame, with the computed position of GAIA stars.

We want to stress that the real calibration error is probably higher than the one computed with the 3^{rd} level of calibration above, as the distortion maps obtained tend to overfit the 400 detected GAIA stars in our field. Moreover, the ORCS software used for the extraction of spectra in the cubes (see Section 3.1.3) only works on integer position. This will add an uncertainty of half of a pixel scale, i.e. ~ 0.16" on all astrometric measurements. We will present in Section 3.4 astrometric comparison with other surveys.

2.3.2 Wavelength calibration

The intrinsic wavelength calibration performed at CFHT (see 2.1.3) is subject to systematic and relative biases from one pixel to another. The first one is due to the uncertainty on the exact wavelength of the He-Ne laser source used for the calibration. Martin and Drissen

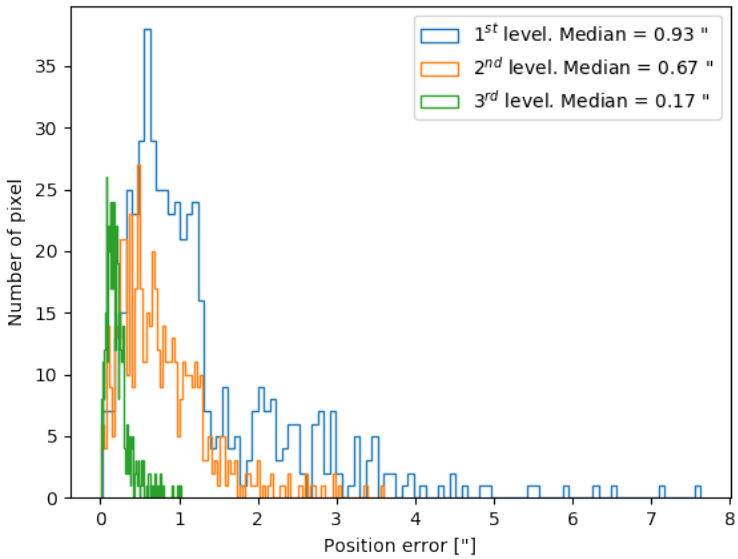

Figure 2.5: Distribution of positional errors with different levels of calibration, computed on GAIA DR1 star positions. At 3^{rd} level, the median error is below the pixel scale.

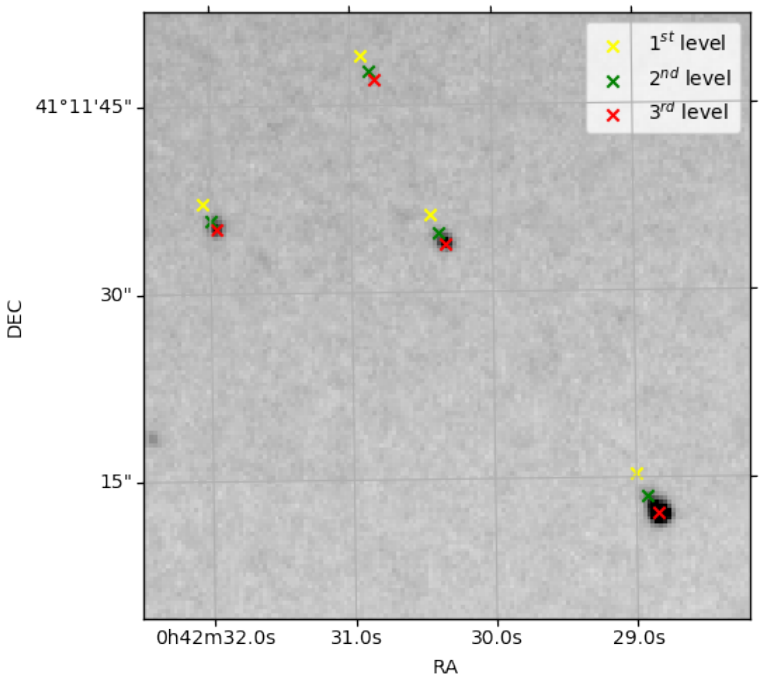

Figure 2.6: Example of GAIA star positions in the deep frame of our observation, with the corrections corresponding to different astrometric calibration levels.

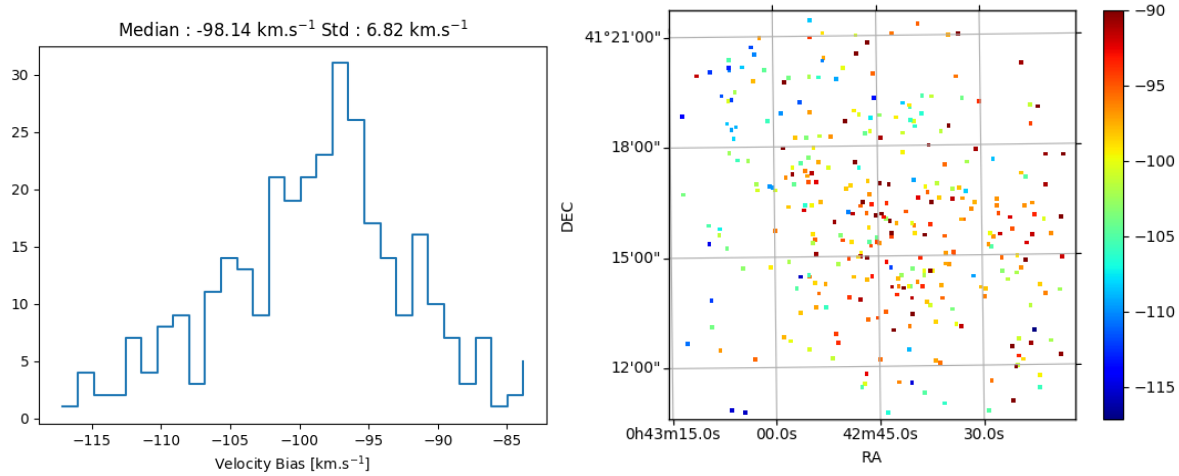

Figure 2.7: Left : Histogram of the velocity difference between values quoted in Ma18 and measurements in the SN2 cube. Right : Color-map of the difference (unit is km.s^{-1}). The median bias of -98.14km.s^{-1} is way above the quoted uncertainties of 2.21 km.s^{-1} in Ma18. SN2 data thus need to be recalibrated.

(2017) evaluates that an uncertainty of 1 Å on the laser wavelength translates into a 55 km.s^{-1} uncertainty on the velocity. The second one is due to uncorrected deformation and distortions in the instrument and affect each pixel differently.
In Ma18, sky emission lines (Meinel OH bands, which should appear at 0 km.s^{-1} on the spectra) are visible across the whole field of view and are used to recalibrate the wavelength of each spectra. Because no strong sky emission lines appear in the bluer SN2 filter, we choose instead to use the velocities of the point-like emission lines sources presented in Ma18, where these sources could also be detected in the SN2 cube (see Section 3.2 for the matching method). We used ORCS tools to extract these sources, fit their spectra and measure their velocity (again, see Section 3.2 for details). We considered conservative exclusion criteria to keep only confident detections. We discarded fitted sources with a Signal to Noise Ratio (SNR) lower than 5 on the [OIII]5007 line, as well as those with an uncertainty on the velocity estimation of more than 5 km.s^{-1}. We thus kept 327 matches covering in a relatively uniform way the field of view. The histogram of the velocity difference between SN2 and SN3 measurement is presented in Figure 2.7, as well as a 2D map of this bias. The median of the difference, -98.14km.s^{-1}, is much higher than the quoted velocity uncertainties in Ma18 (2.21 km.s^{-1}), hence the need for a wavelength/velocity calibration of the SN2 data cube.
This bias seems to be structured. A global offset affects the whole FOV and is probably due to the uncertainty on the He-Ne laser source wavelength used for the calibration (see Section 2.1.3). We also observe spherical structures that might be due to optical distortions improperly corrected in the reduction pipeline. Zernike polynomials are well suited to model this kind of deformation (Noll, 1976, see). We show in Figure 2.8 a 4^{th} order Zernike polynomial fitting the velocity bias, as well as an histogram of the residuals. The residual bias is distributed around 0.13 km.s^{-1} with a standard deviation of 6.14 km.s^{-1}; this residual error has been added as a systematic uncertainty to all the following velocity measurements. This value is 3 times higher than the quoted 2.21 km.s^{-1} in Ma18. The

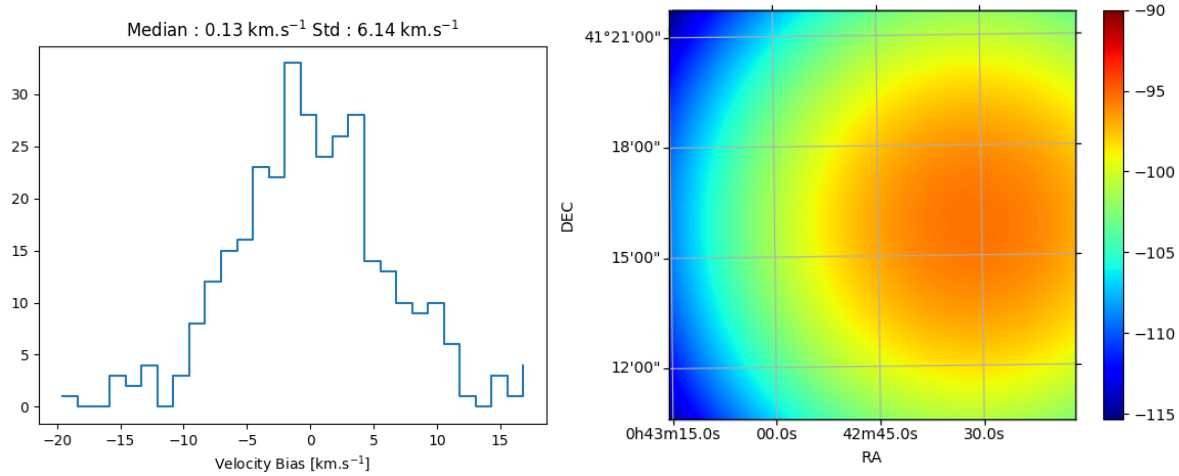

Figure 2.8: Right : 4^{th} order Zernike polynomial fit of the velocity bias map displayed in Figure 2.7. The color-map unit is km.s^{-1}. Left : histogram of the bias after wavelength correction. The residual error of 6.14 km.s^{-1} represents 7.4% of the spectral channel width, and 3.6% of the spectral resolution.

lower resolution of our cube is responsible for that. In terms of uncertainties relative to the channel width, our uncertainty represents 7.4% of the mean channel width (uncertainties in SN3 represented 5.2%).

2.3.3 Flux calibration

The SITELLE flux calibration method has been described in Martin and Drissen (2017), but is subject to some uncertainties. In particular the Modulation Efficiency (ME) loss, that is estimated with the observation of a standard star closely before or after the data acquisition, is corrected in the reduction pipeline at CFTH and needs to be checked. Like in Ma18, we try to assess the uncertainties on the flux calibration by comparing it with Hubble Space Telescope (HST) observation archives.
HST F502N narrow filter bandpass falls under SN2 bandpass (see Figure 2.9). By integrating SN2 spectra under HST transmission curve, one can obtain a flux map simulating an HST observation, that can be directly compared in terms of surface brightness with a real one from the same field of view, once properly aligned and corrected for the difference in pixel scale. Two fields of view observed by HST with the F502N filter match the SN2 FOV, and each of them contains two observations, hereafter called WFC3$_{1,2}$ and ACS$_{1,2}$ after the instruments used for their acquisition. We show a contour of these fields on top of SN2 deep frame in Figure 2.10.
For each observation, we interpolated the HST image on the SN2 pixel grid using the previous astrometric calibration (Sec. 2.3.1), and divided by HST pixel scale ($S_{WFC3} = 0.0393''^2$, $S_{ACS} = 0.050''^2$) to obtain a surface brightness map. In the meantime, we integrated each SN2 spectra contained in the FOV under F502N transmission curve, and corrected for SITELLE pixel scale ($S_{SITELLE} = 0.321''^2$). We thus obtained two flux maps in units erg.cm^{-1}.s^{-1}.arcsec^{-2} that could be directly compared pixel by pixel.
We show in Figure 2.11 an example of the ratio of a SITELLE map over an HST map

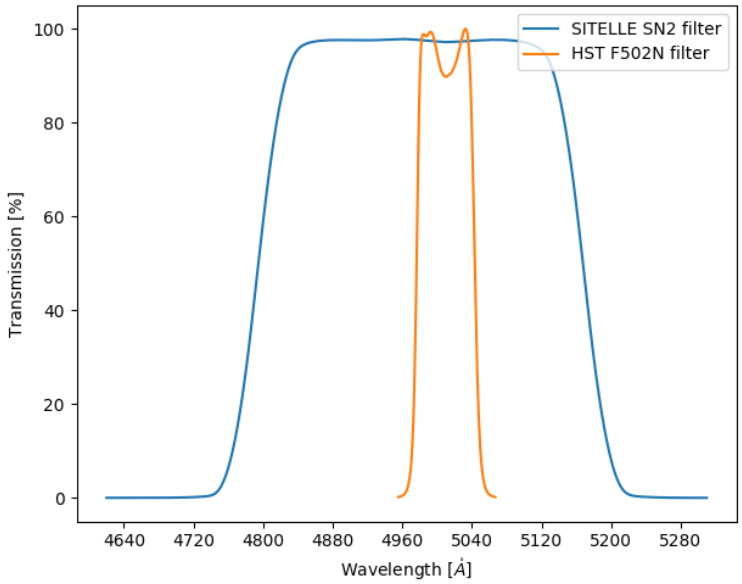

Figure 2.9: SN2 filter and HST F502N (λ_{mean} = 502.3 nm) filter transmission curves are displayed together. One can simulate an HST observation by integrating SN2 spectra under HST transmission curve.

computed with the $WFC3_1$ observation. We see a flat distribution and no gradient, confirming the quality of the astrometric calibration. We detect PSF residuals, especially in the center, due to the better spatial resolution of HST data.

We show in Figure 2.12 histograms of the 4 ratio maps obtained with this procedure, and in Table 2.2 a summary of their statistics, that we attempted to analyze in the same way Ma18 did. The disparity between ACS_1 and ACS_2 ratios is high (median of 1.052 for the first one, 1.267 for the second). Because the exact same procedure has been applied to both of them, only an intrinsic difference between HST observations themselves can explain such a bias. We show in Figure 2.13 direct comparisons of the two ACS observations. The absolute calibration of these archive data is indeed questionable, as the ratio of the images is not centered on 1. The median value of 1.204 indicates an absolute bias of ∼20% in their calibration and explains the difference observed when comparing with SITELLE data. Unfortunately, we cannot rely on these ACS/HST data to improve the quality of SITELLE absolute flux calibration.
Ratios of SITELLE data to $WFC3_1$ and $WFC3_2$ observations are more consistent with each other. They seem to indicate a ∼11% overestimation of the flux in SITELLE data in this FOV, and a dispersion of 4.4% in pixel-to-pixel relative calibration. But again, we directly compared the two WFC3 observations in Figure 2.13 and observed that the dispersion between them is itself 3.6%. We can therefore not correct any relative calibration error in SITELLE with this.
From this analysis, we can not obtain precise enough estimation of a bias in SITELLE flux calibration. The comparison with WFC3 suggests an overestimation of ∼11% but the FOV concerned is too small to extrapolate this value to the whole SN2 data. We conclude

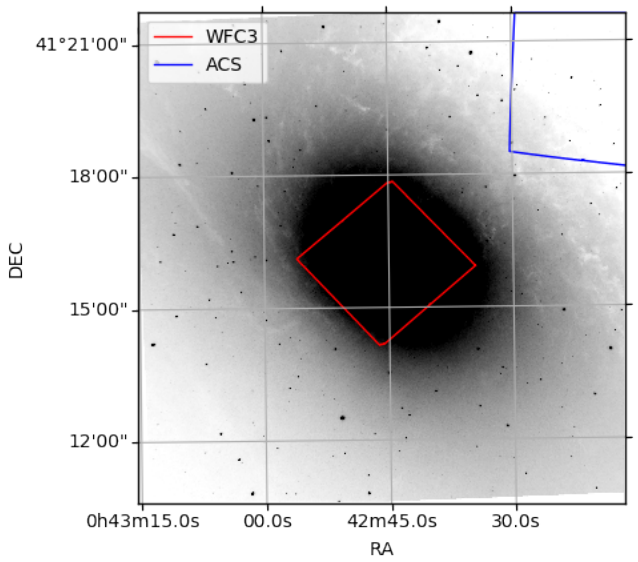

Figure 2.10: Contours of the two fields of view observed by HST with the F502N filter, plotted on top of the deep frame of the SN2 datacube. Each field contains two observations, denominated hereafter $WFC3_{1,2}$ and $ACS_{1,2}$.

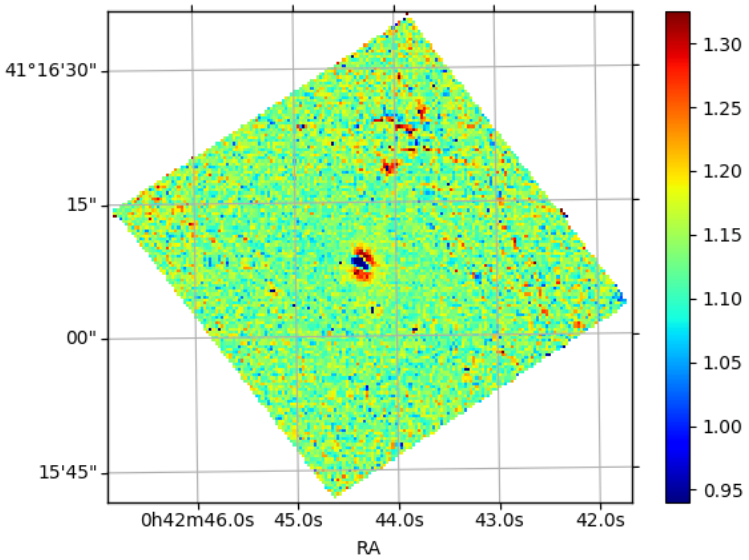

Figure 2.11: Ratio of the SITELLE flux map and HST flux map obtained from the WFC_1 observation. The pixel values are distributed around 1.12 with a standard deviation of 4.5. No gradient is detected, confirming the quality of the astrometric calibration. The bias around the center of the galaxy is due to the difference in pixel resolution between SITELLE and HST, SITELLE having a larger PSF than HST.

Instrument	Field	Median [Std] in %
WFC3 UVIS	WFC3 1	112.6 [4.5]
WFC3 UVIS	WFC3 2	111.5 [4.2]
ACS WFC	ACS 1	105.6 [14.6]
ACS WFC	ACS 2	126.7 [19.8]

Table 2.2: Statistics of the ratio maps between SITELLE data and HST observations. The disparity between ACS observations is big (105.6% vs. 126.7 %) and is explained by a calibration bias between themselves (see Figure 2.13). WFC observations are more consistent with each other and seem to indicate an overestimation of ∼11% of SN2 flux.

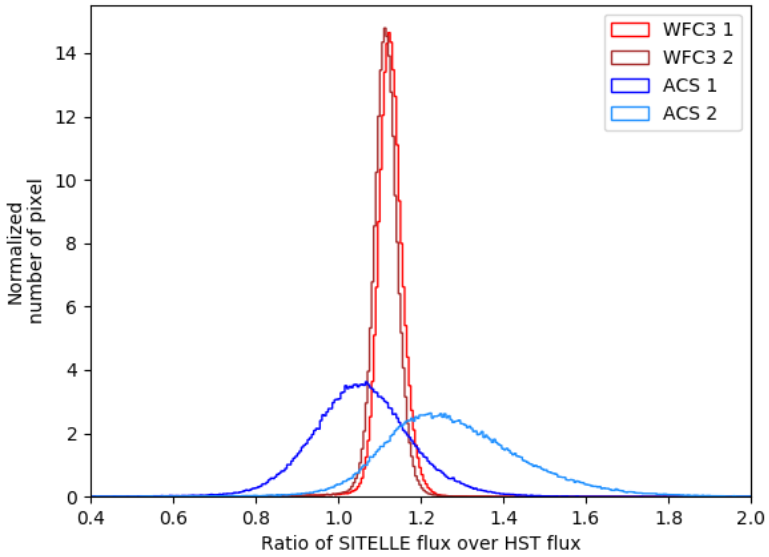

Figure 2.12: Histograms of the ratio between SITELLE and HST flux maps. Statistics are presentedn in Table 2.2. The disparity between ACS_1 and ACS_2 is explained by an absolute bias in HST calibration.

that despite the path taken in Ma18, HST archives are not the best material to perform a precise flux calibration analysis, as it contains itself disparities between observations on the same FOV. A better calibration estimation will be inferred from the comparison of source fluxes with previous studies in Section 3.4.

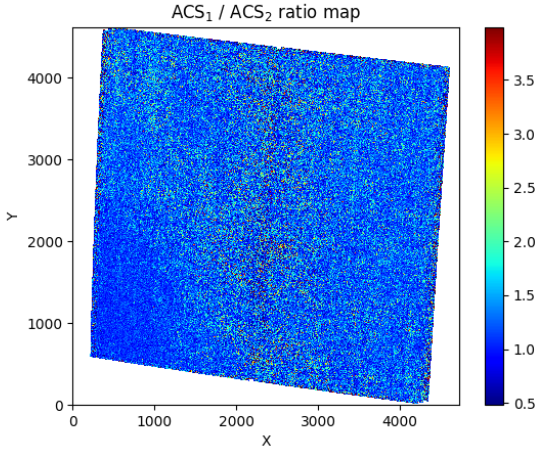

(a) Direct ratio map of the ACS_1 to ACS_2 observations

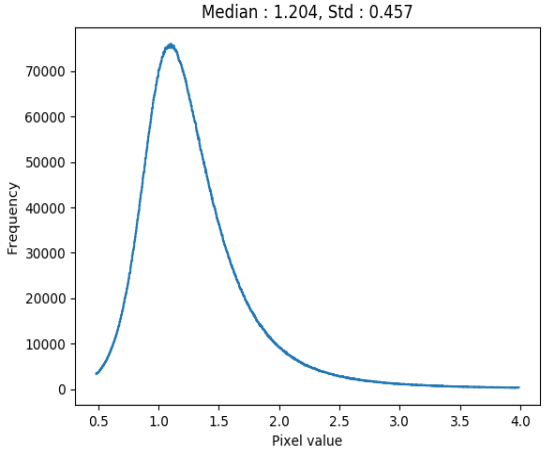

(b) Histogram of the ratio between ACS_1 and ACS_2 observations.

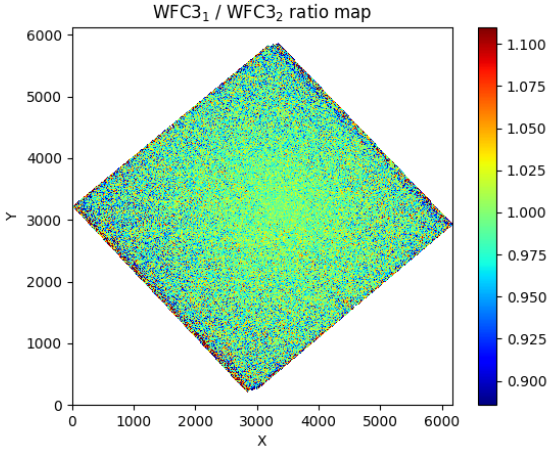

(c) Direct ratio map of the $WFC3_1$ to $WFC3_2$ observations

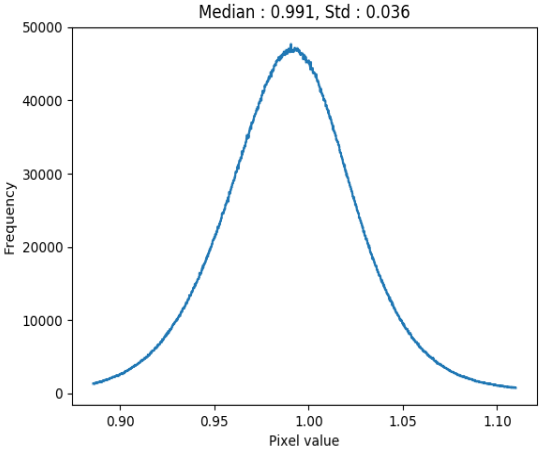

(d) Histogram of the ratio between $WFC3_1$ and $WFC3_2$ observations.

Figure 2.13: Direct comparison of the two HST observations in each FOV, with a 2D ratio map and an histogram. Top row : comparison of ACS_1 to ACS_2. The ratio is not centered on 1 (median 1.204) indicating a calibration bias between the two. Bottom row : comparison of $WFC3_1$ to $WFC3_2$.

Chapter 3

Analysis

SITELLE instrument, with its high resolution both spatially and spectrally, is perfectly designed for the study of point-like emission-line sources. Martin et al. (2018) already identified a catalog of more than 800 Hα point-like sources in the SN3 data cube, most of them probably being Planetary Nebulae.
This section describes the steps undertaken to analyze our now calibrated data. We completed Ma18 source catalog by looking for point-like emission line sources in the SN2 data cube and counterparts in the SN3 data.
With the combined analysis of the SN2 and SN3 data cubes presented here, we will be able for the first time to study the main strong emission lines of point sources in Andromeda bulge with standard diagnostic diagrams, and to compare its PNe population with the ones known in the Milky Way (Frew and Parker, 2010, e.g.). The comparison with the previous work of Merrett et al. (2006) in the same FOV will be a good test of the quality of our reduction and calibration procedures presented in Sec. 2, and we will extend his study due to better sensitivity. As discussed later in the thesis, we will also be able to study their kinematics, and to compare it to the stellar bulge and gas kinematics.

3.1 Source detection in the SN2 cube

In Ma18, sources in the SN3 data cube have been identified by visual inspection of the FOV. We adopt here for SN2 a more systematic approach.

3.1.1 Creation of a detection map

To optimally detect emission-line sources, we aimed at building a map where these sources would stand over the background, a so-called detection map or Signal to Noise Ratio (SNR) map. If we subtract the mean flux for each spectra, and divide by a noise estimate associated to each spectra, we expect, according to the Central Limit Theorem, that the distribution will be close to a standard normal distribution, i.e. a Gaussian distribution of mean 0 and standard deviation 1. In presence of point sources, this distribution should exhibit an upper tail corresponding to the sources we are looking for. The noise estimation is thus crucial to disentangle the genuine point sources above statistical fluctuations.
First, we subtract the strong stellar continuum of the galaxy, as it affects any standard source detection procedures. Due to the important luminosity gradient of M31 bulge, a local estimation of the background at each pixel has to be done. For each pixel, the

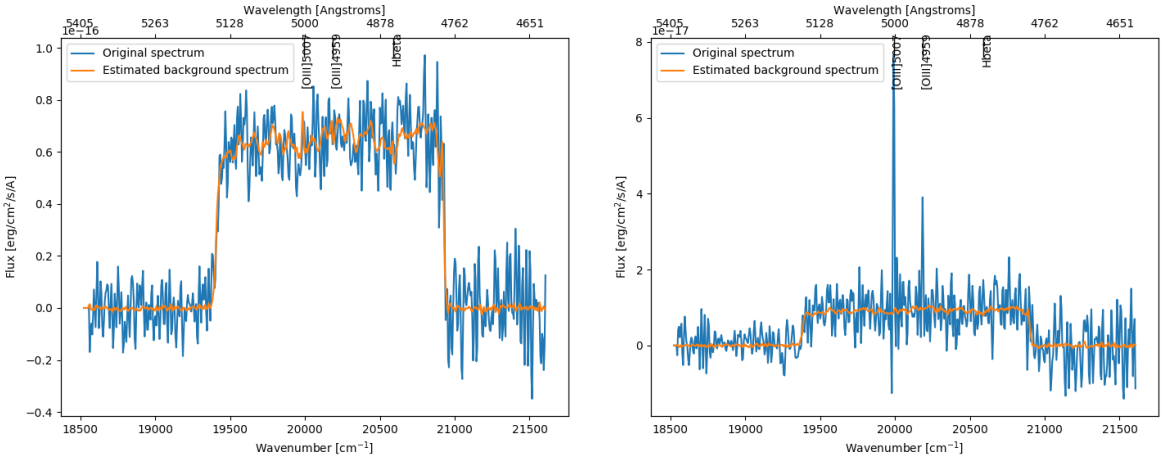

Figure 3.1: Background spectrum estimation examples (in orange) over the original spectrum (blue). This estimate intends to capture the local background spectral features without including flux from the point source, and represents a good approximation of the stellar continuum.

estimate is computed as the median of spectra taken into a 30×30 pixels box around the pixel of interest, excluding the central 5×5 pixels box (see Figure 3.1).

Second, we have to evaluate the noise impacting our spectra. As mentioned in Section 2.1, due to the interferometric technique, noise is proportional to the flux received by all spectral channels for this pixel, and is uniformly distributed across all channels. Figure 3.2 shows background subtracted spectra examples with the different noise levels discussed below. The flux-uncertainty map provided with the SN2 cube (see Figure 2.3) significantly overestimates the noise level (see Figure 3.2). As no obvious reason has been found for this, we tried to recompute this presumed photon noise, defined as the square root of the number of Analog to Digital Unit (ADU) (as a proxy of the number of photons) received per spectra (before removing the background). However, this led to another overestimation of the noise map (see see Figure 3.2), probably due to the flat-field and dark corrections the data underwent in the first step of the reduction (see 2.1.3), transforming the intrinsic noise.
We also tried to estimate the noise by measuring the standard deviation of the flux on the left and right sides of the filter bandpasses (18500 - 19300 cm^{-1} and 20950 - 21600 cm^{-1} ranges, see the SN2 and SN3 filter transmission curves in Figure 2.2). These regions should contain only noise and not be contaminated by stellar background spectral features. We found that the level was significantly higher on the right than on the left side (see Figure 3.3). Not only the noise but the whole signal seems to increase with wavenumber along a spectrum. This is probably be due to an instrumental effect beyond the scope of this work, like a wavenumber-dependent gain in the reduction pipeline. We did not try to correct for this effect, and discarded these estimations.

From this analysis, it appeared that the best way to estimate the noise level was to do it close to the signal, i.e. only inside the filter bandpass. However, as the emission lines can be strong with respect to the noise background, we compared two methods to clip them from the spectra:

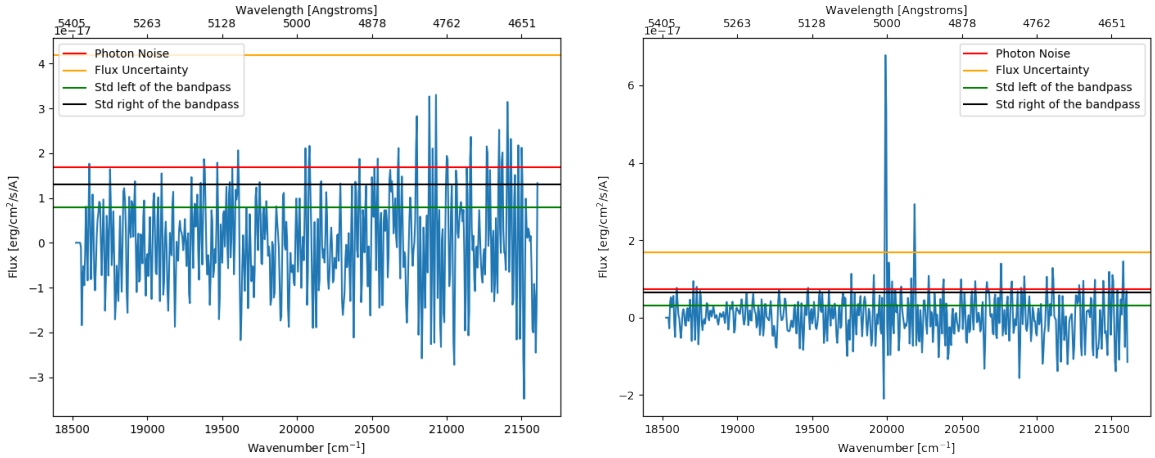

Figure 3.2: Levels of noise estimated with different methods, on a SN2 spectrum with a strong (resp. no) point-source signal on the right (resp. left) panel. These are the same sources as Figure 3.1, after background subtraction. The orange line represents the noise estimated by the flux uncertainty map for this spectrum and is way overestimated. The red line represents our estimation of the photon noise, which seems a bit overestimated. The green (resp. black) line represent the uncertainty estimated on the left (resp. right) hand side of the spectra, i.e. below 19300 cm^{-1} (resp. above 20950 cm^{-1}). There is a systematic difference between the left and right estimates of about a factor 2. None of these estimates evaluate correctly the noise level in the filter bandpass.

- by clipping channels around the position of each line at Andromeda systemic velocities of V_{syst} = -300 km.s^{-1}. We choose the clipped regions to be 5 line-width wide (i.e. $\sim$ 10 spectral channels, or 55 cm^{-1}) on each side of the line. We call this the "lines-clipped" method hereafter.
- by σ-clipping flux values above 3.5 σ. The two-sided p-value of 3.5 in a standard normal distribution is 4.65×10^{-4}, meaning on our 223 channels wide bandpass, we expect $\sim$ 0.1 pixel to lie that far from the mean. We thus expect that σ-clipping should only affect spectra showing emission lines. We call this the "σ-clipped" method hereafter.

Figure 3.4 displays examples where parts of the spectra are used to compute the standard deviation are highlighted, while Figure 3.5 shows how the two estimations are consistent with each other. We explain at the end of this Section which one was preferred.
We used the same clipping procedures to measure the mean flux in the spectra. Subtracting the mean flux allows to turn off objects with continuous emission, specifically resolved stars, from our detection map.
Having measured these quantities, our detection map pixels are then defined as

$$\text{Detection Map}_{i,j} = \max_{\text{along spectral axis}} \frac{\text{Spectra}_{i,j} - \text{Mean Flux}_{i,j}}{\text{Noise}_{i,j}}$$

i.e. similar to a signal-to-noise ratio map.
An excerpt of the detection map obtained by σ-clipping is shown in Figure 3.6.
To discriminate genuine signal from noise on these detection maps, we simulated a white noise data cube (mean 0, standard deviation 1) with the same dimensions as ours, and

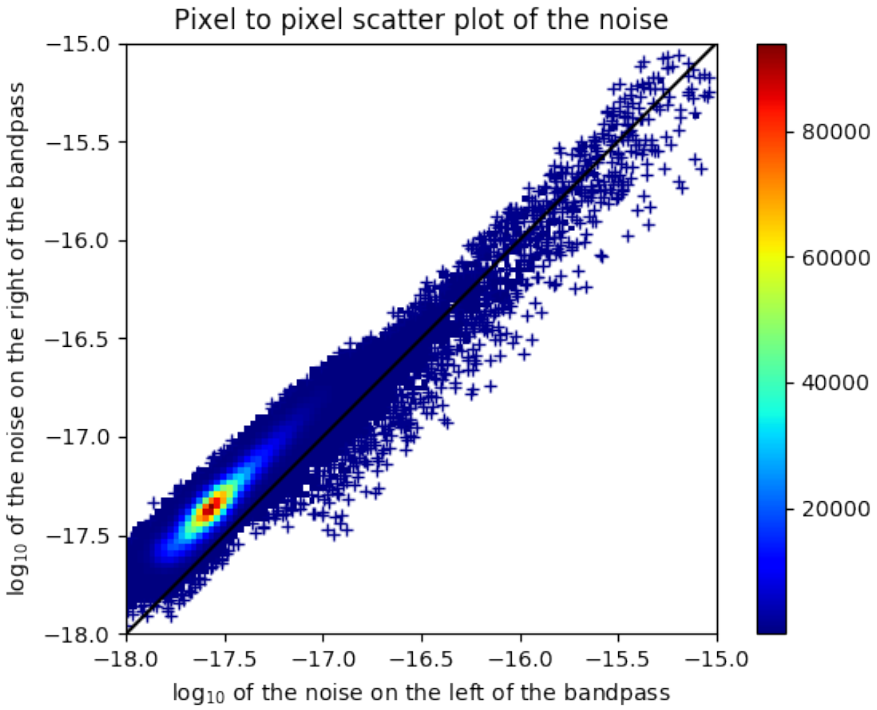

Figure 3.3: Pixel-to-pixel scatter plot of the standard deviations measured outside the filter bandpass on the left and right. Where there were too many points (N > 3) close to each other, we replaced the scatter markers by a colored pixel with the color representing the number of points in this pixel. The filled black line represent the one-to-one relation. There is a clear offset from this line, indicating a multiplicative bias between the two estimates.

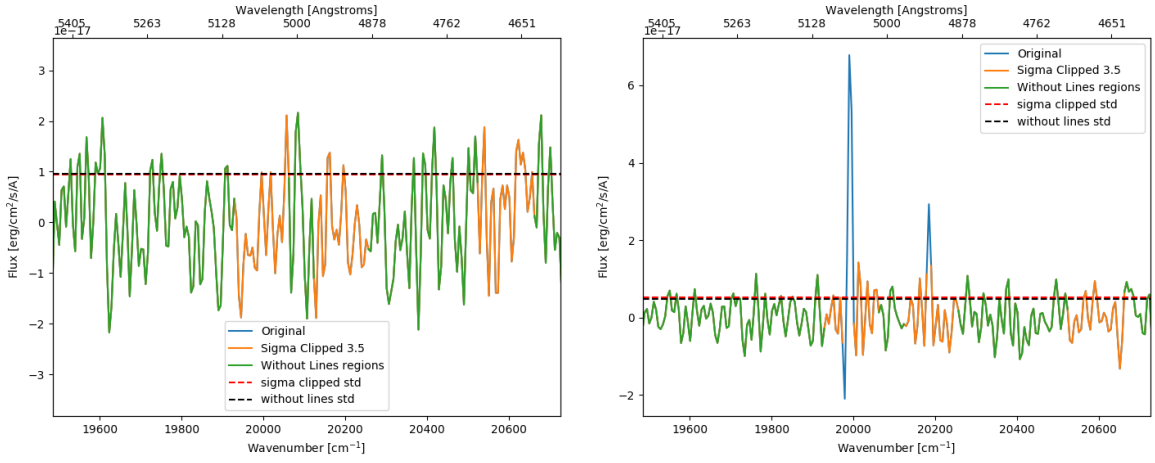

Figure 3.4: Examples of how the two methods affect different spectra (these are the same sources than Figure 3.1). We display in blue the original spectra (background subtracted), in orange the spectra after σ-clipping, and in green after line-clipping. Left : σ-clipping has no effect, whereas we clipped regions around lines whether or not a signal was present. Right : σ-clipping and line-clipping affect differently the spectra. We plot in dashed red (resp black) the standard deviation of the spectra after σ-clipping (resp. line-clipping).

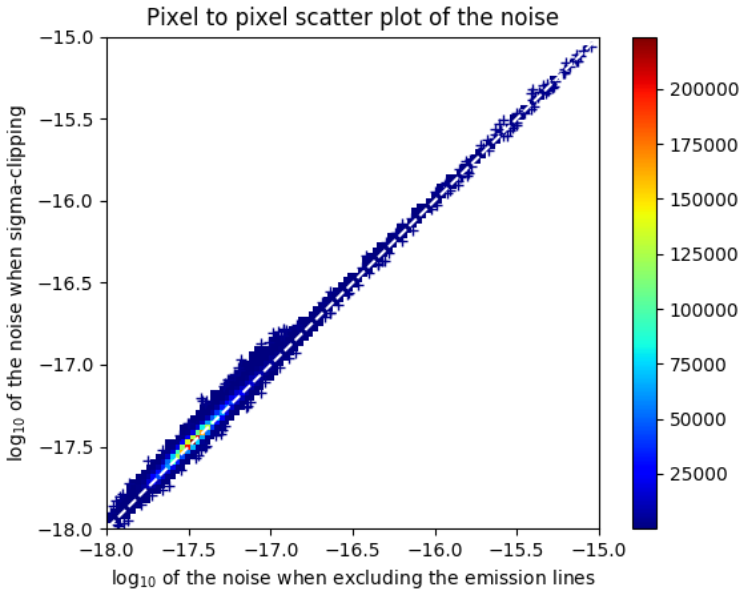

Figure 3.5: Pixel-to-pixel scatter plot of the standard deviations measured on σ-clipped spectra or line-clipped spectra. Where there was too many points close to each other (N $>$ 3), we replaced the scatter markers by a colored pixel with the color representing the number of points in this pixel. The dashed white line represents the one-to-one relation, which is in good agreement with the plot, showing the two noise estimation methods are consistent with each other.

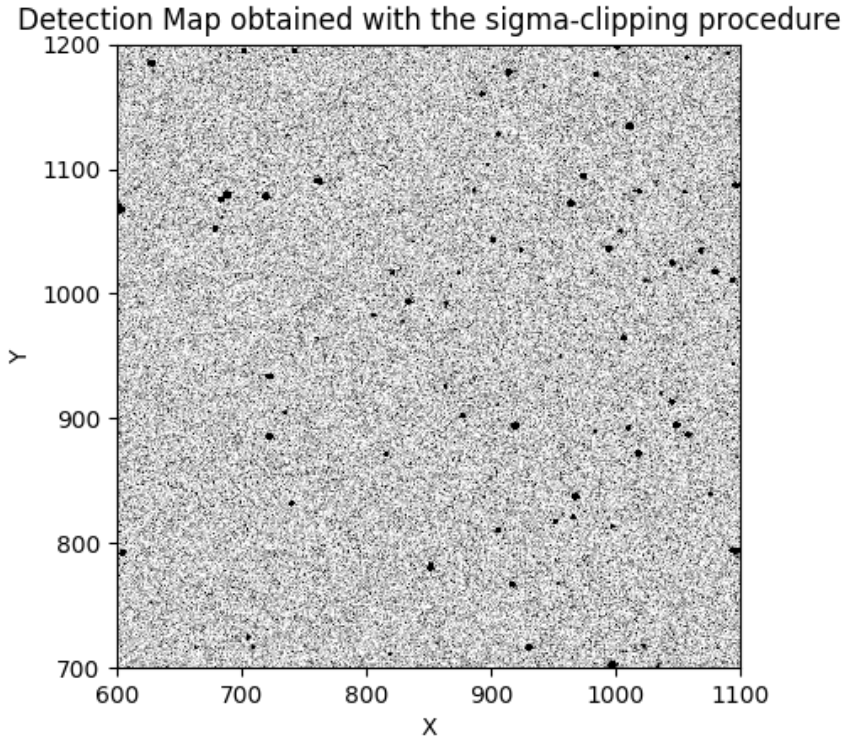

Figure 3.6: Detection map obtained with σ-clipping. Each black region is an emission-line object. This method enables to remove the effect of the strong luminosity gradient affecting the field, and shuts down continuous emission point-like sources like foreground stars.

Detection Map	Median	Std
White noise	2.73	0.38
σ-clipped	2.74	0.75
Lines-clipped	2.79	0.89

Table 3.1: Median and standard deviation of the different detection maps pixel distribution, whose histograms are shown in Figure 3.7.

created a detection map out of it by taking the maximum value at each pixel along the spectral axis.
Histograms of the detections maps computed on the white noise, σ-clipped and line-clipped detection maps are shown in Figure 3.7, with their statistics presented in Table 3.1. The match with the white noise histogram is good, validating our approach, and an excess toward high values is clearly visible. We observe in the σ-clipped histogram a strong artifact around a detection level of 3.5, exactly the value used for σ-clipping. It is likely that the noise in spectra containing low signal (lower than 3.5 σ) was here overestimated, lowering the SNR for these pixels. The induced bias is hard to estimate and we discarded this detection map. The lines-clipped method was thus preferred. The median value of the lines-clipped SNR detection map (2.79) is good agreement (1%) with the median value obtained with the white noise detection map, but the excess at high values seems a bit overestimated between ~ 3 and ~ 3.75. As later discussed, the detection of genuine source requires a spatial correlation of the pixels of the source due to the Point Spread Function (PSF) that is not included in the white noise simulation. Hence, many other criteria will be added to define sources, as described in the next sections.

3.1.2 Detection algorithm

The next step is to measure the positions of the detections corresponding to genuine signal on this map. Our detection map is a maximum map where flux continuity between adjacent pixels is not necessarily granted. Hence, we do not expect to see only point-like sources on this map, and often the Point Spread Function (PSF) is not well defined. For these reasons, dedicated algorithms for point-source detection such as DAOFIND (Stetson, 1987) and IRAF starfind (Tody, 1993), based on PSF fit, are not well suited, and failed at efficiently detecting sources.
We choose instead to define our sources as regions on the detection map containing at least 4 connected pixels with a value above a given threshold. The segmentation image method described in photutils (see Bradley et al. (2017)) was used for this purpose. It is of high importance to find a threshold that will guarantee the detection of a maximum of real sources and a minimum of false positives, and we aimed at optimizing this with respect to the noise level. We ran our detection algorithm on the white noise and lines-clipped maps to estimate how many credible sources could be detected for each level. The result is presented in Figure 3.8, and Table 3.2 summarizes the number of detections for a few values of threshold. The number of sources detected on the noise map steadily decrease to reach 0 before a threshold of ~ 4, whereas it reaches a constant limit for the lines-clipped map, clearly indicating the presence of sources. To guarantee the detection of a maximum of sources even at low SNR, we settled on a threshold value of 3.5, where according to this plot we should have $\sim$10% of false positive detections.

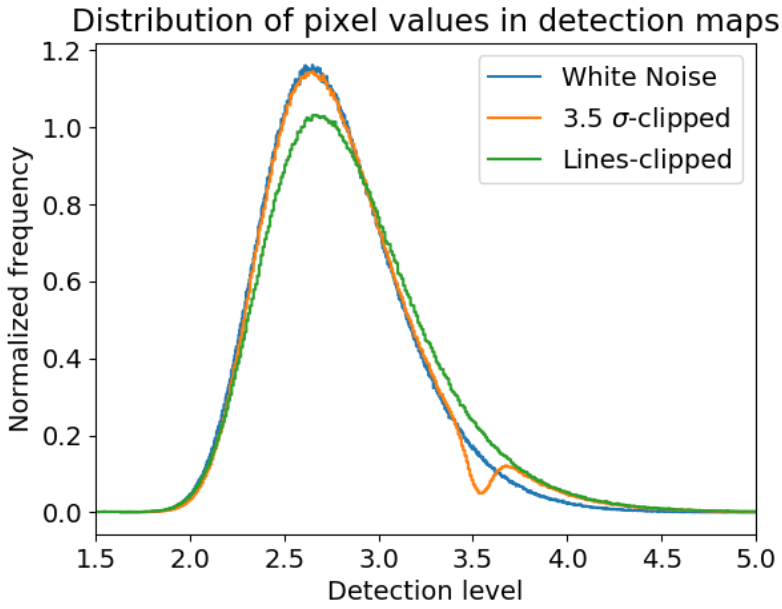

Figure 3.7: Histograms of the different detection maps. σ-clipped and lines-clipped detection maps agree well with the noise map, with a clear excess at high detection values. The artifact seen in the σ-clipped map around 3.5, the value used for σ-clipping, induces a bias in the SNR estimation that is hard to model. We preferred to keep the lines-detected map only. The excess seems a bit overestimated at detection levels between 3 and 3.75, but other criteria (especially the need for spatial correlation) will reduce the number of false positives.

$n\sigma$	White noise	σ-clipped	lines-clipped
3.5σ	1014	3008	8435
4σ	0	523	591
4.5σ	0	450	466
5σ	0	397	430

Table 3.2: Numbers of detections as function of the threshold. We adopt a loose threshold of 3.5σ as we will apply additional selection steps, based on the characteristics of the expected signal.

Doing so, we ended up with a list of more than 8400 detection candidates. They consisted of positions of the centroids of the sources, as well as morphological properties such as total area, ellipticity or area, i.e. useful quantities do discriminate between real detections and noise.

3.1.3 Spectra extraction and fit of the emission lines

At each source candidate position, we used ORCS tools (see Martin et al. (2015)) to extract and fit the spectra.
Because ORCS uses integer pixel position to extract spectra, we first had to round the centroid position of our detections. This will explain later why we have a higher than expected separation when cross-matching our sources with previous detections.
Like Ma18, in order to maximize the signal-to-noise ratio of the sources, spectra of a 3×3 pixels box around the detection position were summed, from which was subtracted a background spectrum defined as the median of spectra taken in a 30×30 pixels box minus the 5×5 central pixels (like in Section 3.1.1). As ORCS is highly sensitive to the velocity guess provided as input to the fit, a simple Gaussian function was first adjusted to the strongest line present in each spectra to estimate precisely its position. If this estimate was included in the [-1200; 300] km.s^{-1} velocity range, where we expect to see Andromeda's PNe, it was then used as an initial guess to simultaneously fit the [OIII]5007 [OIII]4959 and Hβ lines with a sinc LSF. We forced the fit to estimate the same velocity for each line, while letting all other parameters free. When the guess on the velocity was not included in this range, we do not expect the object to be a PNe, and we thus fitted only the Hβ line. These fast objects could be for example background galaxies, and will be discussed in Section 4.
ORCS also offers the possibility to use the convolution of a sinc and a Gaussian to model the lines, which can be useful when dealing with expanding objects having a velocity dispersion that would broaden the emission lines. For such a convolution, the resulting line width is given by $\sigma_{sinc\otimes G} = \sqrt{\sigma_{sinc}^2 + \sigma_G^2} = \sigma_{sinc}\sqrt{1 + \left(\frac{\sigma_G}{\sigma_{sinc}}\right)^2}$. In Ma18, where the fits where adjusted by visual inspection, they used this modified LSF where needed and report broadening values in the range 5-50 km.s^{-1}. In our lower resolution SN2 data cube (line width = 168 km.s^{-1}), this would represent a maximum broadening of about 9% of the lines. Besides, this type of fit is very sensitive on the input broadening guess, and is unstable when used in a systematic way with little visual inspection and correction. Given the low benefits such a LSF would give us (only a few percent in the broadest sources), we used only the simple sinc LSF to fit emission lines.

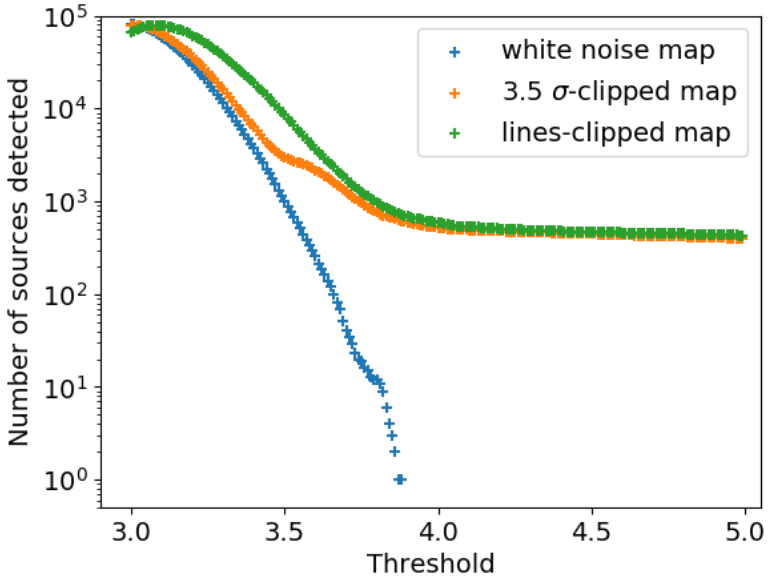

Figure 3.8: Scatter plot of the number of sources detected for different thresholds. After a threshold of ~ 4, no more detections are measured on the white noise map, whereas we reach a limit on the real detection map. We also plot the result obtained on the σ-clipped map, to show how the artifact seen in Fig. 3.7 impacts the detection procedure. We note also that a low threshold value, the number of sources detected tends to saturate or even drop a little. When the threshold is very low, the number of connected pixels exceeding the threshold increase and the algorithm is not able anymore to separate (or de-blend) sources next to each other. Multiple sources can be confound with a big one, and the number of detections reaches a limit.

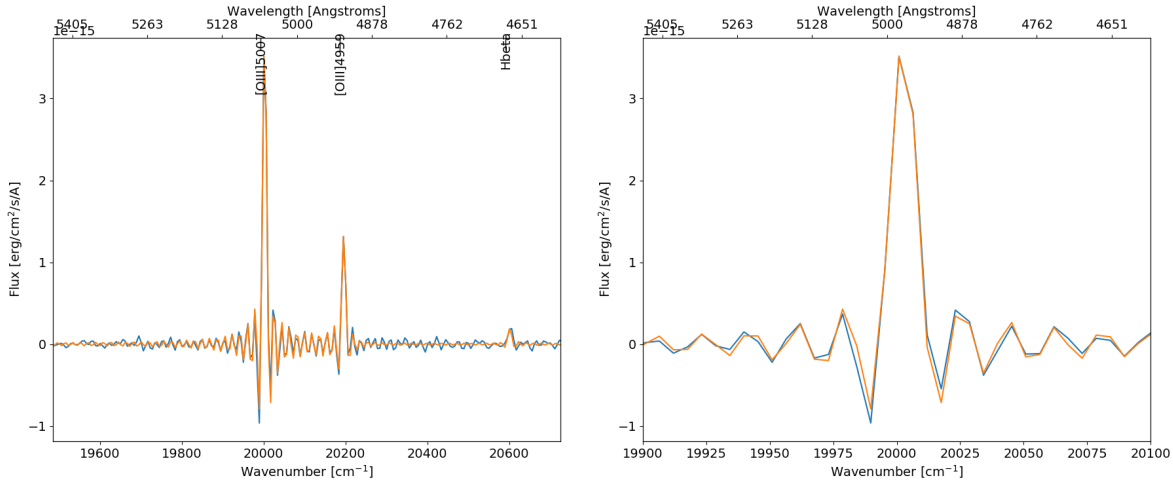

Figure 3.9: Example of a fit on a source candidate. All lines are fitted simultaneously at the same velocity. A sinc LSF is used to model the emission lines.

Finally, we used the estimated background spectrum to fit the local gas velocity, which is identified by its [OIII] emission line. For this line, the sinc FWHM is dominated by the kinematic broadening, and a simple Gaussian LSF was used. Only the velocity of the line could be safely determined as the absorption of the stellar background strongly affects the flux of the line and is hard to properly estimate. A different approach to determine this flux will be presented is Section 5.1.1.
We present in Figure 3.9 an example of a fitted spectra, with a zoom on the core of an emission line. The sinc LSF is well fitted with ORCS methods. The fitting procedure directly provides the velocity of the lines as well as the flux contained in each of them and their respective errors. For each line, a Signal to Noise Ratio (SNR) is also outputted, defined as the ratio between the flux of the line and its uncertainty.
We note that some spectra have a non symmetric LSF. An example is given in Figure 3.10. Martin and Drissen (2017) describes in detail this phenomena, that is due to an incorrect phase correction in the reduction process. Such a deformation leads to error both on the position of the centroid of the line as well as on the measured flux. When comparing with Figure 3 of Martin and Drissen (2017), the phase offset in our spectra seems small (less than $\frac{\pi}{4}$), and corresponding errors are of the order of a few percents. This affects differently different regions of the FOV, and its correction is beyond the scope of this work.

After fitting all the source candidates, we considered an emission line as detected if it had a SNR higher than 3, and kept only candidates having at least one line detected. This cut lowered the number of detections to only 3767, out of the 8435 candidates. The measured flux for the undetected lines has been replaced by 3 times the level of noise in the spectra; these will be used as upper limits. This cut lowered the number of detections by a factor of more than 2, which is puzzling as we tuned our detection method, presented in 3.1.2, to detect sources having a SNR higher than 3.5, and estimated only 8.5% of false detections. This discrepancy is due to the fact that the detection map build in Section 3.1.1 was made pixel by pixel, while here we use a 3×3 binning to extract spectra. This binning smoothed the signal in source candidates that were actually only fluctuations.

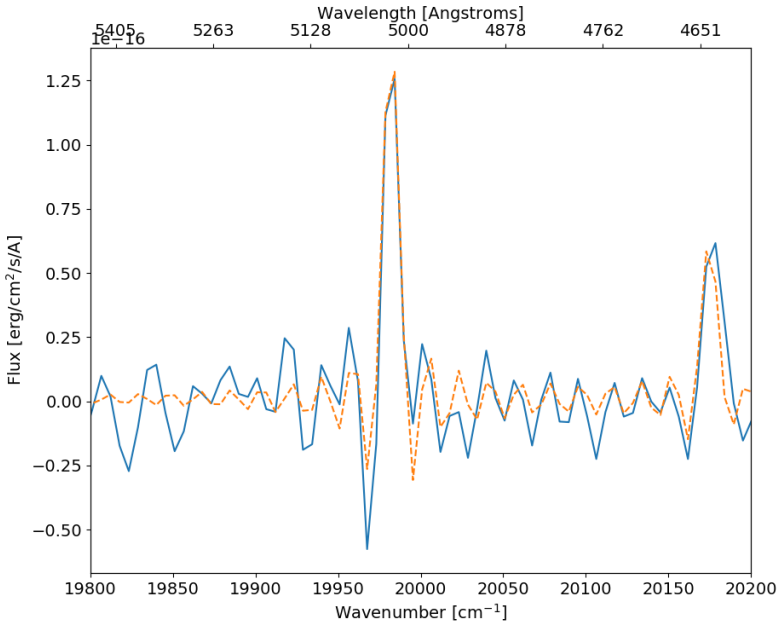

Figure 3.10: Example of a spectra with a non-symmetric LSF. The blue curve is the original spectra, while the orange one is a sinc fit. This deformation has been explained in Martin and Drissen (2017) and affect both the measured flux and velocity of the line.

We show in Figure 3.11 histogram of the maximum measured SNR (between the 3 lines) for each source. This limit of 3 on the SNR is rather a lower bound, as after visual inspection, it is not obvious that sources having such a low SNR really exhibits emission lines. Our sample is actually polluted by a lot of sources whose dominant line is Hβ at very low SNR. We redefined our criteria for detection to reduce this population. We kept only sources having either:

- a SNR in the [OIII]5007 line higher than 3. This is the strongest line for Planetary Nebulae. This threshold still includes some noise, that will be used to estimate our limit of detection (see Section 3.6. This represents 1090 objects.
- OR a SNR in the Hβ line of at least 5. 205 objects match this sole criterion. They can be HII region (no strong [OIII] emission but still part of M31) or background objects at high velocities.

We summarize the number of detections with respect to the different cuts in Table 3.3. The final detection catalog to be analyzed thus consists of 1295 objects. It certainly still contains some noise, that will be discussed when computing the luminosity function in Section 4. Table 3.4 summarizes the number of sources where the different emission-lines were detected.

3.2 Source matching in SN3

To fully understand our detection and be able to classify them using diagnostic diagrams (see Section 4.1, we need to measure Hα, [NII] and [SII] fluxes, or at least obtain lower

Cut	Number of detections
4 pixels connnected with a value above 3.5 on the lines-clipped detection map	8435
At least one emission line with a SNR higher than 3	3667
[OIII]5007 SNR $>$ 3 OR Hβ SNR $>$ 5	1295

Table 3.3: Numbers of detections with the different cuts.

Line	Number of sources showing this line
[OIII]5007	1090
[OIII]4959	430
Hβ	474

Table 3.4: Numbers of sources showing a measured flux higher than 3σ for the different SN2 lines in the final catalog.

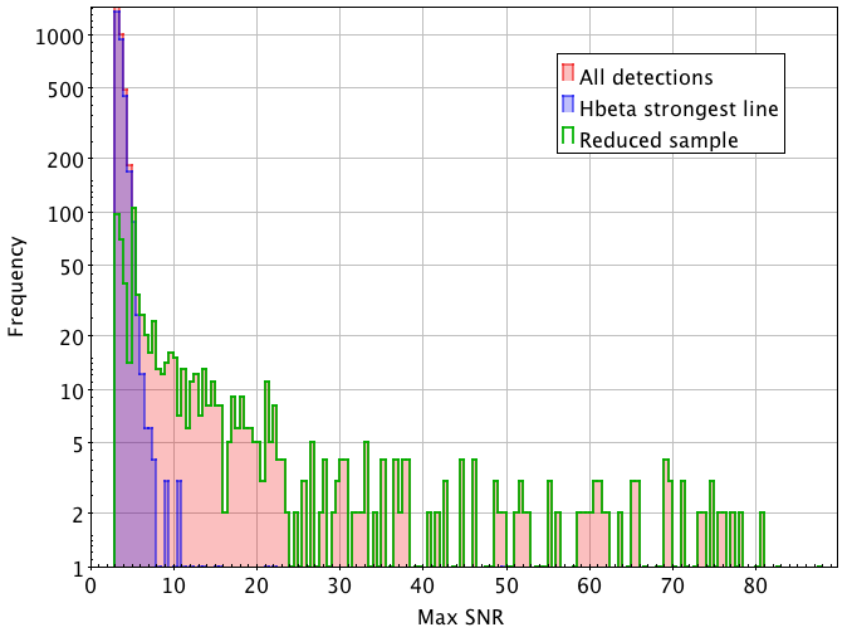

Figure 3.11: Histogram of the maximum SNR of lines [OIII]5007, [OIII]4959 and Hβ for each detection. The red histogram corresponds to the 3767 sources having at least one line with a SNR higher than 3, and the blue histogram corresponds to detections where Hβ is the strongest line detected (highest SNR). One can see that this sample generates the most detections at low SNR. It probably gathers both low ionized interstellar medium such as filaments or clouds, and noise. The disentanglement of this phenomena is beyond the scope of this thesis, and we focused therefore on more truthful detections when no [OIII]5007 line were observed. The criteria quoted in the text define the green sample on this diagram. Detections at low SNR have been reduced by a factor 10.

Line	Number of sources showing this line
Hα	533
[NII]6583	256
[NII]6548	117
[SII]6716	18
[SII]6731	10

Table 3.5: Numbers of sources showing a measured flux higher than 3σ for the different SN3 lines in the final catalog.

bounds on their level. Ma18 catalog contains ∼800 sources with detections in Hα and flux estimations of the [NII] and [SII] doublet. Many sources can be cross-matched ($\sim$ 440 actually, see later) with this catalog, but a lot do not have counterparts. We thus decided to re detect ourselves sources in the SN3 data.
Even if SN2 and SN3 cubes are taken on the same FOV, there is no guarantee that they can be compared pixel-to-pixel, due to different optical deformation of the instrument and possible misalignments. We thus used the previous astrometric calibration (Section 2.3.1) to get physical positions of our SN2 detections, and computed back their pixel coordinates in SN3. Because the spectrum extraction and fit with ORCS has to be done on integer pixel positions, a rounding is necessary. To avoid a bias induced by this rounding, we looked for a local maximization of the SNR ± 1 pixel away of the computed position, in each direction.
The fit was then performed in the same manner than in SN2 : the spectrum was extracted in a 3×3 pixel box, and corrected for the local background. The 5 lines Hα, [NII]6583,6548 and [SII]6716,6731 were fitted simultaneously, at a velocity bounded in a ± 30 km.s^{-1} range around the velocity measured in SN2. This time, the LSF used is the convolution of a sinc and a Gaussian, as the broadening can be comparable to the intrinsic line width (∼42 km.s^{-1} in SN3) and thus affect its shape and flux (see Section 3.1.3). A constant broadening guess of 20 km.s^{-1} has been used.
Like in SN2, we declared a line as identified when its SNR was higher than 3 (again, this is more like a lower bound); flux of the undetected lines have been replaced by 3 times the level of the noise on the spectra, and are therefore upper limits. On the 1215 candidates, 533 objects show a detection in Hα. We gather in Table 3.5 the number of sources where the different emission-lines were detected.
Using Ma18 analysis, we corrected the measured fluxes for the modulation efficiency bias (1.13) and the HST flux calibration ($\frac{1}{0.969\pm0.014}$) leading to a correction of 1.17 ± 0.017. The aperture loss correction is discussed in the next Section.

3.3 Aperture-Loss Correction

The 3×3 binning we used to extract and fit the spectra does not capture the whole extent of the source, and the flux measured in the previous Sections need to be corrected for this. In Ma18, they performed a statistical analysis on mock PSF and concluded on a 1.88 ± 0.07 factor to apply everywhere in the cube.
But the exact Point Spread Function (PSF) is actually not well-known, and does not have the same shape in the whole FOV. In Figure 3.12, we show a excerpt of the deep frame

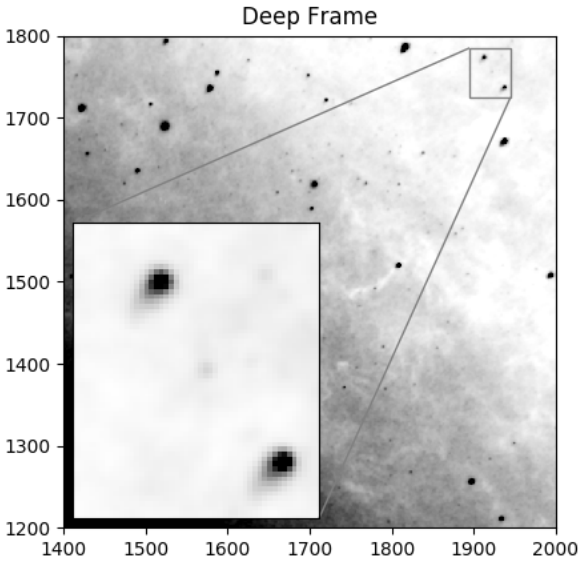

Figure 3.12: Excerpt of the SN2 deep frame showing an elongation of the PSF. This elongation is stronger in the corners of the frame, and always seems to be oriented toward the center. This leads us to believe this artifact is an instrumental optical effect.

in a corner of the SN2 field, where the PSF is clearly elongated toward the center. This can be due do a misalignment of the two interferometric cubes in the reduction steps, or uncorrected optical distortions in the instrument spreading the PSF in one direction.

We developed for SN2 a more systematic approach to correct the source flux depending on its position in the FOV. To properly analyze this corrective factor, we used only our strongest and most reliable detections, defined as the ones having a SNR on the [OIII]5007 line higher than 10 (381 sources). We build for each of them a 30×30 pixels flux map centered on the source position, consisting of the sum of the (background subtracted) spectral channels around the detected lines up to 1 spectral full width at half maximum (FWHM) (see Figure 3.13 for a more graphical explanation). The flux of up to 3 emission lines can thus be summed on this frame. This map does not pretend to hold the whole flux coming from the object, but can be used to study how the flux behaves when moving away from the center of the source.

To estimate the corrective factor to apply, we performed on this map aperture photometry in squares of increasing side length, to build a growth function of the flux of the source when moving away from the center. We modeled the PSF with a 2D Gaussian, meaning that our 1D growth function could be computed as :

$$\mathrm{Flux}(r) = \frac{\mathrm{A}}{2\pi} \int_{-\frac{r}{2}}^{\frac{r}{2}} \int_{-\frac{r}{2}}^{\frac{r}{2}} \mathrm{e}^{-\frac{X^2}{2}} \mathrm{e}^{-\frac{Y^2}{2}} \mathrm{d}X \mathrm{d}Y$$

with $X = \frac{x-x_0}{\sigma_x}, Y = \frac{y-y_0}{\sigma_y}$, x_0, y_0 being the coordinates of the center of the source, σ_x, σ_y the standard deviations along each axis, and A the amplitude of the Gaussian.

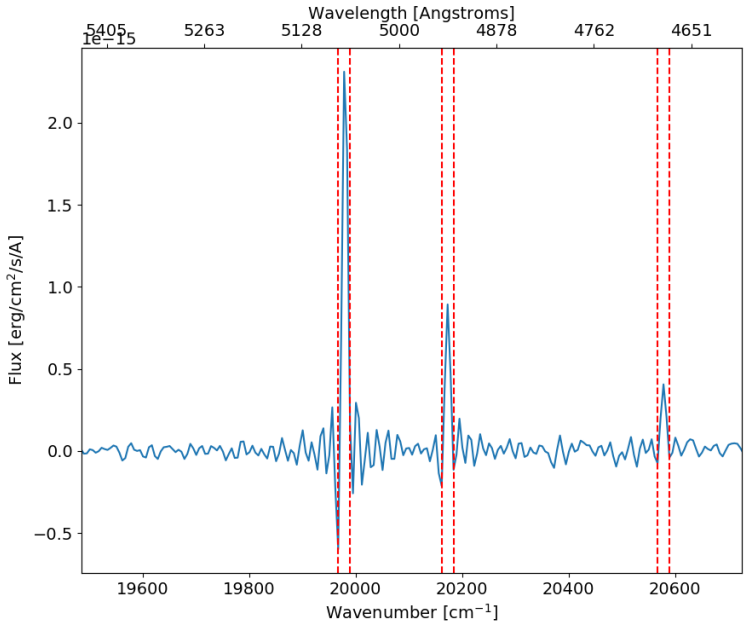

Figure 3.13: Example of the background subtracted spectrum of a source used for the flux correction analysis. To build the flux map of this source, we summed the (background subtracted) spectrum between the dashed red lines. This corresponds to ± 1 FWHM around the position of the detected lines. The created flux map is shown in Figure 3.14.

We know that for a 1D Gaussian probability distribution:

$$\mathrm{P}(X \leq z) = \Phi(z) = \frac{1}{\sqrt{2\pi}} \int_{-\infty}^{z} \mathrm{e}^{-\frac{t^2}{2}} \mathrm{d}t = \frac{1}{2}\left[1 + \mathrm{erf}\left(\frac{z}{\sqrt{2}}\right)\right]$$

and thus:

$$\begin{aligned}
\mathrm{P}(X \in [-z, z]) &= \frac{1}{\sqrt{2\pi}} \int_{-z}^{z} \mathrm{e}^{-\frac{t^2}{2}} \mathrm{d}t \\
&= \Phi(z) - \Phi(-z) \\
&= \frac{1}{2}\left[\mathrm{erf}\left(\frac{z}{\sqrt{2}}\right) - \mathrm{erf}\left(\frac{-z}{\sqrt{2}}\right)\right] \\
&= \mathrm{erf}\left(\frac{z}{\sqrt{2}}\right)
\end{aligned}$$

as erf is an odd function. The flux encapsulated in a box of side length r can then be rewritten as :

$$\mathrm{Flux}(r) = \mathrm{A} \times \mathrm{P}(X \in \left[\frac{-r}{2}, \frac{r}{2}\right]) \times \mathrm{P}(Y \in \left[\frac{-r}{2}, \frac{r}{2}\right]) \tag{3.1}$$

$$= \mathrm{A} \times \mathrm{erf}\left(\frac{\frac{r}{2} - x_0}{2\sigma_x\sqrt{2}}\right) \mathrm{erf}\left(\frac{\frac{r}{2} - y_0}{2\sigma_y\sqrt{2}}\right) \tag{3.2}$$

We fitted the growth function for each detection with this model. The total flux of the source is obtained as the limit of the fit at large r, i.e. the amplitude A ($\lim_{x\to\infty} \mathrm{erf}(x) = 1$).

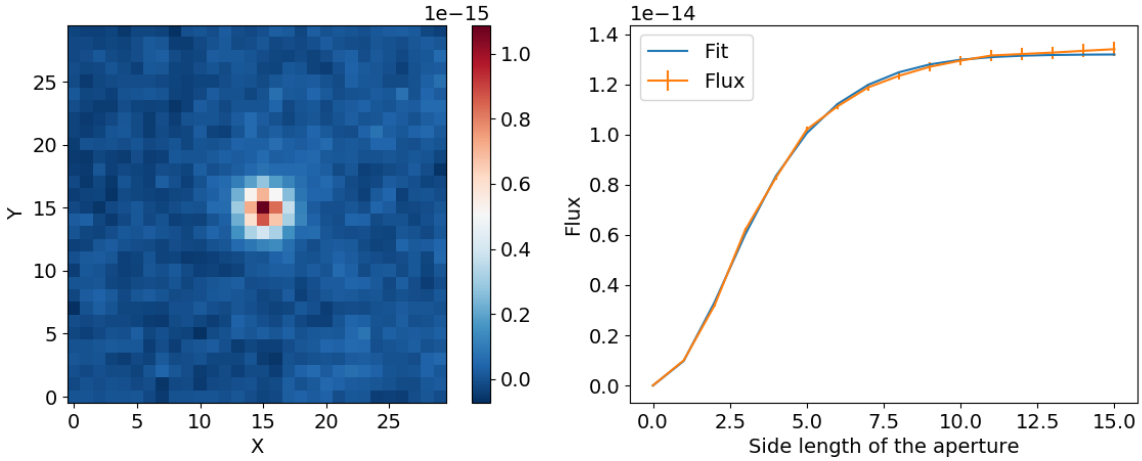

Figure 3.14: Left : Example of a flux map obtained by summing the detected lines (see Figure 3.13). Here, the 3 emission-lines are used to build the map. Right : Growth function computed with aperture photometry on the flux map and fit of this function with Eq. 3.1. The limit of the fit at large r gives the total flux of the source, while we fitted emission lines only in a box of side length 3. The ratio of the two gives the factor that should be applied to correct for aperture loss.

Because we fitted emission-lines only in a box of side length 3, the aperture loss correction factor is obtained as the ratio of the limit of the flux to the flux measured at $r = 3$, i.e. :

$$\text{Aperture\_FC} = \frac{\lim_{r\to\infty} \text{Flux}(r)}{\text{Flux}(r=3)} = \frac{\text{A}}{\text{Flux}(r=3)}$$

From the growth function fit, one can also estimate an equivalent spatial FWHM, defined as the value r at which the flux reaches half of its limit. Four our aperture loss correction, it is important to remove from the sample detections that are actually not point-like sources. We show in Figure 3.15 the histogram of the measured FWHM on our sample. An excess is visible above a FWHM of ~ 5, which can be related to the presence of extended sources. But this can also be explained by the presence of two sources close to each other, or a bad background subtraction (close to the center, the gradient is strong even in a 30×30 box). In those cases, the estimate on the flux limit is biased. We thus discard them by keeping only detections with a FWHM lower than 5 to compute the aperture correction.
The 2D map of correction factor is shown in Figure 3.16. The map shows a spherical structure, confirming that the effect is probably due to optical deformation in the instrument. Because of this, we choose to fit this map with Zernike polynomials, like for the velocity correction in Section 2.3.2. A 10^{th} order polynomial has been chosen this time. The fitted map, as well as the histogram of the residuals, is shown in Figure 3.16. The histogram shows a much more normal distribution, with a median of -0.03 and a standard deviation of 0.30.
This fitted map has been used to correct the flux of all our detections, and the residual error of 0.30 has been taken into account into the flux error estimation.
To compare with Ma18 estimates of 1.88 ± 0.07, we reproduced the same procedure on SN3 data. Considering only sources with a SNR on the Hα line higher than 10 (296 objects), we fitted a growth function with the model defined in Equation 3.1. Once corrected for too

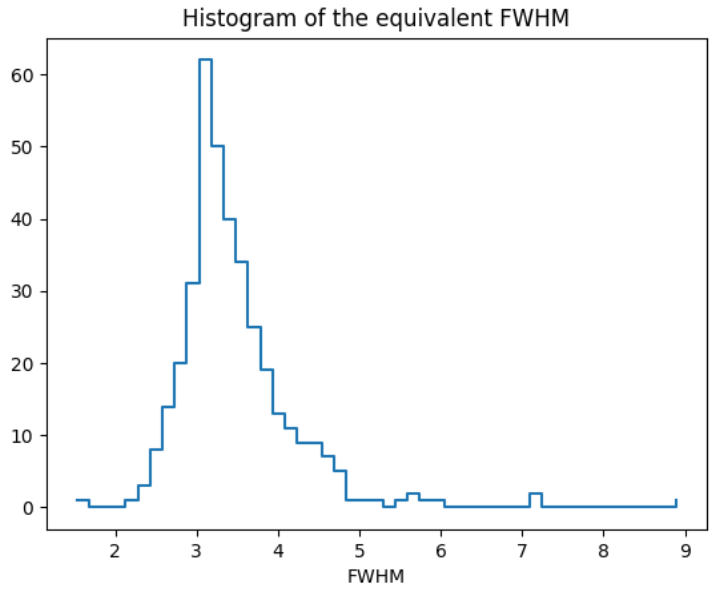

Figure 3.15: Histogram of the equivalent FWHM for detections in our sample. The FWHM has been estimated from the fit of the growth function, as the radius at which the flux reached half of its maximum. We see some outliers at FWHM > 5, that we discard for now to focus on point-like objects.

high FWHM objects (extended sources, close sources or strong background, see above), the aperture flux correction can be computed. We show in Figure 3.17 the 2D map of the correction factor as well as the histogram of its distribution. The median value of 1.84 is close to Ma18 estimate of 1.88 and validates the approach. We however see a much broader deviation from this value, due to high correction factors measured in the corners of the FOV, where the sources are particularly elongated. Like for SN2, a Zernike polynomial has been adjusted on the 2D map. The residual of the fit are centered on -0.36 with a dispersion of 0.248. This fitted 2D map represents more truthfully the correction factor across the whole FOV and has been preferred over Ma18 estimate to correct for aperture loss in the SN3 measurements. This will lead to a small bias when comparing our detections with Ma18 catalog (see Sec. 3.4).

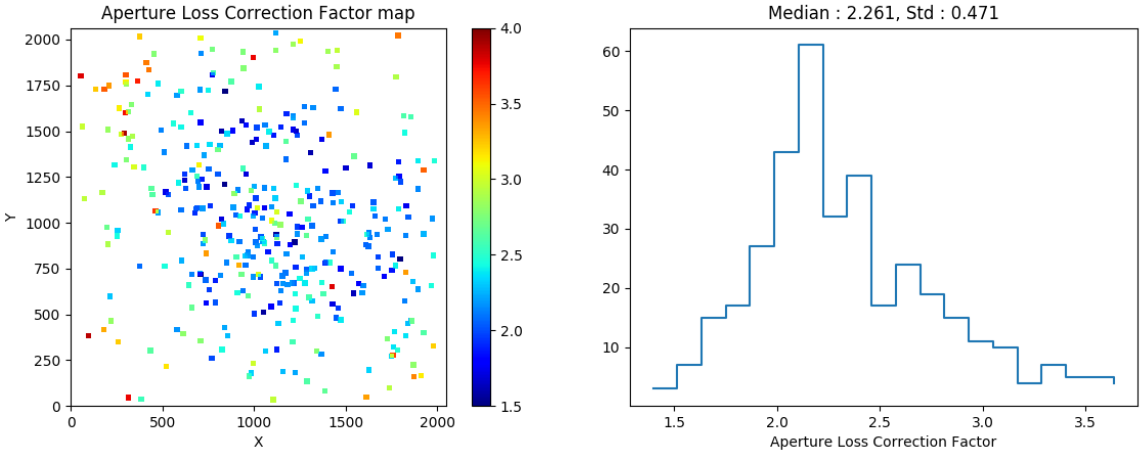

(a) (b)

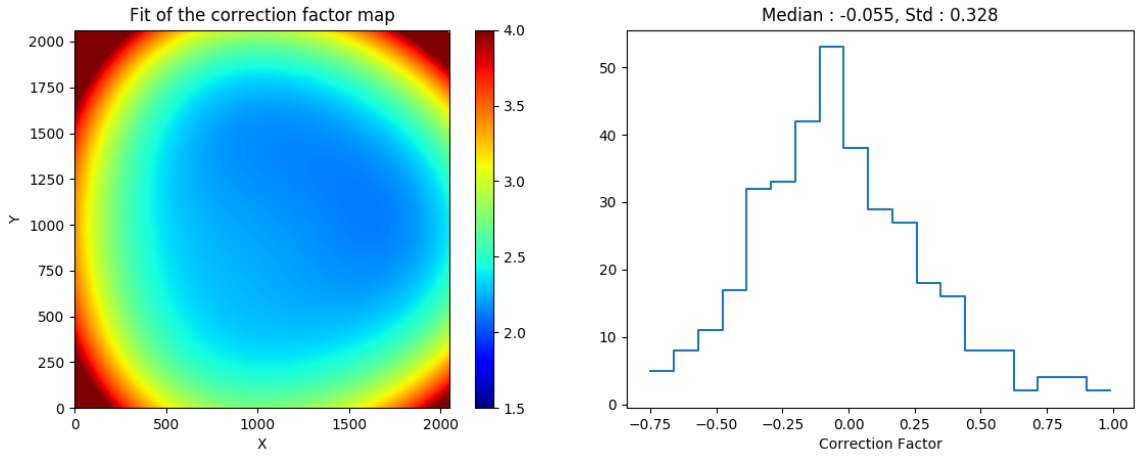

(c) (d)

Figure 3.16: Top row : map of the aperture loss correction factor in SN2 data, and histogram of its values. Bottow row : Zernike fit of the map, and histogram of the residuals. After the fit, the correction is recentered on -0.055 with a standard deviation of 0.324. This error on the correction factor has been included in all the uncertainties.

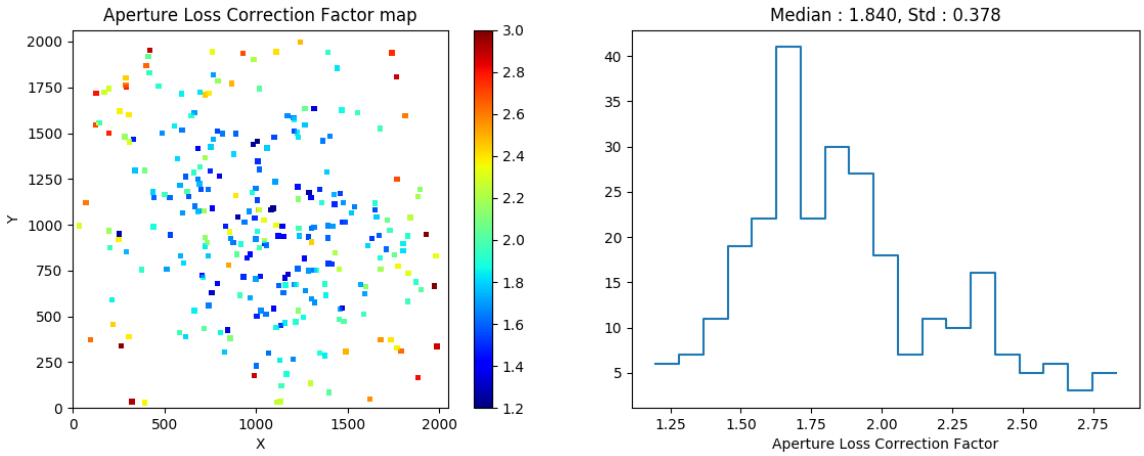

Figure 3.17: Map of the aperture loss correction factor in SN3 data, and histogram of its values. The median value is close to Ma18 estimate of 1.88, validating the approach. But the dispersion is much broader, due to the PSF elongation in the corner that we took into account. After fitting a 10^{th} order Zernike polynomial on the 2D map, the residuals are centered on -0.036 with a standard deviaiton of 0.248.

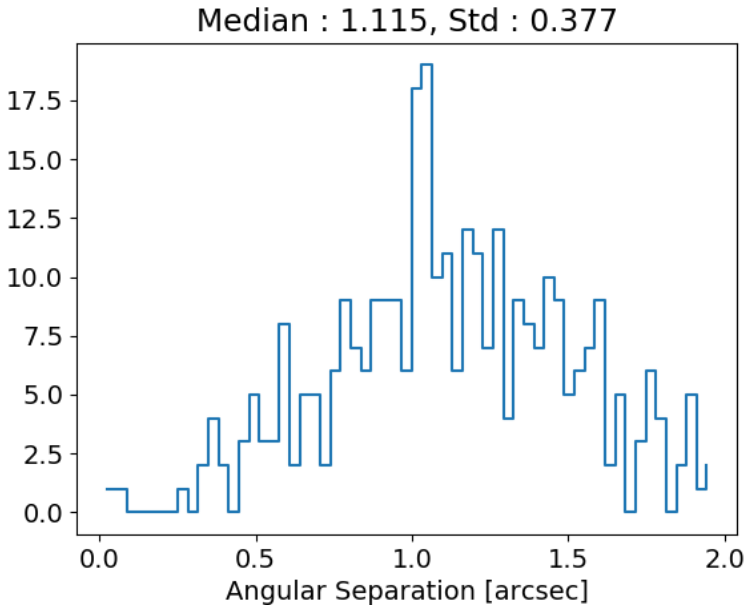

Figure 3.18: Histogram of the angular separation in arcseconds between positions measured in the SN2 cube and their matches in Me06 catalog. The median separation of ∼1.1" has already been observed between Me06 and Ha06 in the FOV we are cross-matching, and is a bias inherent to Me06 data. The standard deviation of ∼0.38" is compatible with Me06 uncertainty of ∼ 0.6".

3.4 Comparison with previous catalogs

To double check the quality of our calibrations and corrections, and to evaluate our completeness, we can compare these detections with previously cataloged PNe in M31.

3.4.1 Comparison with Merrett et al. (2006)

Merrett et al. (2006) has investigated PNe in M31 in a very large area (up to 1.5° away from the center), using a specifically designed instrument (Planetary Nebula Spectrograph) for the explicit study of [OIII]5007 emission-line objects. The catalog reports 338 detections in our FOV, what makes it an ideal sample to compare with our SN2 data. 318 cross-match were found with our catalog (94% overlap).
We show in Figure 3.18 a histogram of the angular separation. The separation seems to suffer from a systematic error of ∼ 1.1". Me06 has checked its astrometric calibration with Halliday et al. (2006) (hereafter Ha06), and quotes a systematic offset of ∼1" in the central fields, i.e. precisely where our cross-match has been performed, explaining our angular separation. Ha06 concludes that this offset can be present in either Ha06 or Me06 datasets, but our comparison tends to show that the bias comes from Me06. The dispersion of ∼0.38" is compatible with Me06 quoted dispersion of 0.6".
The velocity calibration can also be assessed. We show in Figure 3.19 a scatter plot of Me06 velocities against our measurements, as well as a histogram of the difference. The agreement with a one-to-one relation is correct. The median of the difference is centered on -0.62 km.s^{-1} with a standard deviation of 16.1 km.s^{-1} that is compatible with Me06

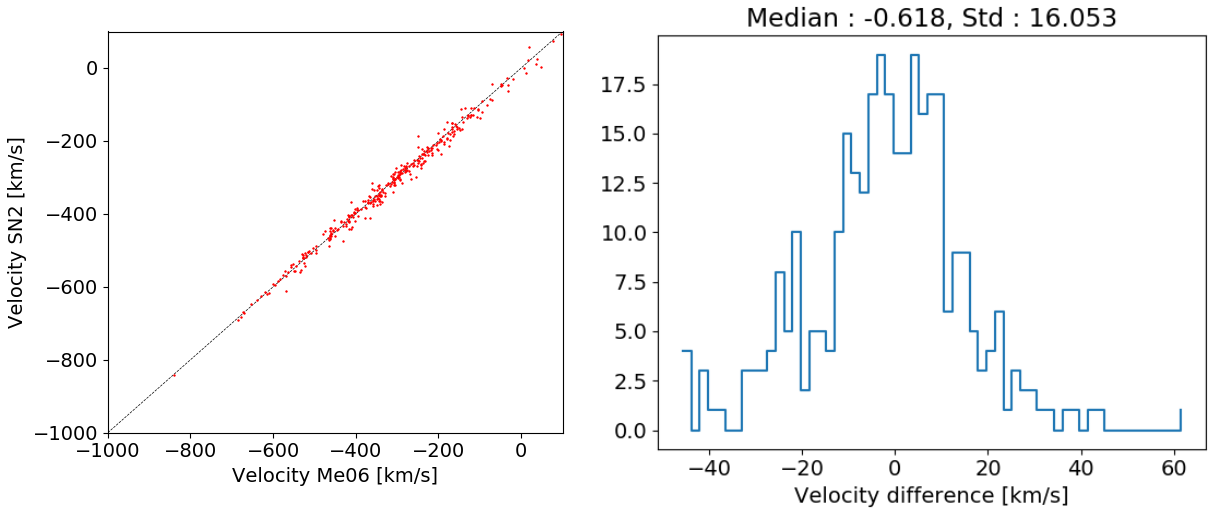

Figure 3.19: Left : Scatter plot of Me06 velocities against our measurements. The dashed black line represents the one-to-one relation, and is in good agreement with the data. Right : Histogram of the difference. The median of -0.62 km.s^{-1} shows no systematic bias in our velocity estimation, while the dispersion of 16.1 km.s^{-1} matches Me06 uncertainties of 17 km.s^{-1}.

uncertainties (17 km.s^{-1}). No bias seems to affect our velocity estimation.
Finally, the flux calibration can be estimated. Following the definition of Jacoby (1989), we computed from the flux in the [OIII]5007 line the relative m_{5007} magnitude as :

$$m_{5007} = -2.5 \log_{10}(F_{5007}) - 13.74$$

We show in Figure 3.20 the scatter plot of Me06 m_{5007} magnitudes against our estimation, as well as a histogram of the difference. There is a systematic bias of about 0.1 magnitudes, well above Me06 uncertainties of 0.06 magnitudes, and translating in a $\sim$ 9.6% overestimation of the flux. This bias is probably due to an incorrect modulation efficiency estimation in the reduction pipeline (see 2.1.3 and Martin and Drissen (2017)). This goes in the same direction as the conclusions of our flux calibration procedure, where an overestimation of $\sim$ 11% of the flux was found with respect to HST images in the very center of our FOV (see Section 2.3.3). The dispersion of 0.33 magnitudes translates to an flux uncertainty of $\sim$ 35% with respect to Me06, a bit higher than the 32% estimated after aperture flux correction. In the end, because we could not obtain a a good knowledge of the modulation efficiency calibration, and because the observed bias is anyway smaller than the associated uncertainties, we did not correct our measured fluxes in consequence. Further investigations need to be conducted to refine more our flux calibration.
We will discuss the completeness of the catalog in Section 4.2.

3.4.2 Comparison with Martin et al. (2018)

The best pairing for our SN3 detections is naturally Ma18 hand classified catalog, based on the exact same observations. No calibration effect can of course be detected from this comparison, but we can check the performance of our automated procedure. From the 533

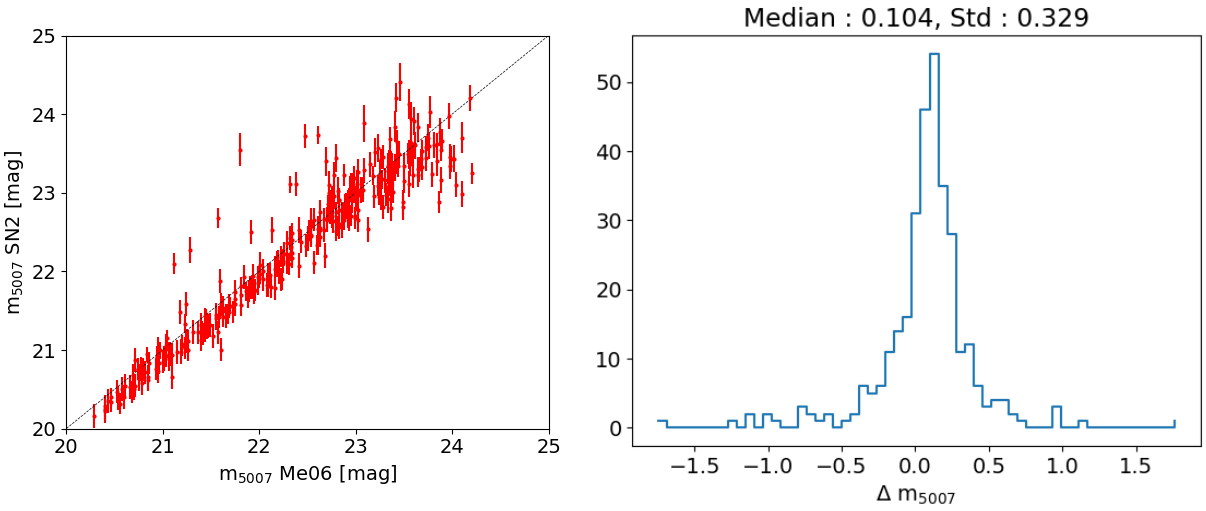

Figure 3.20: Left : Scatter plot of Me06 m_{5007} magnitudes against our measurement, with error bars. The dashed black line represents the one-to-one relation. Right : Histogram of the magnitude difference ($\Delta m = m_{5007}$ Me06 - m_{5007} SN2). There is a systematic offset of 0.1 magnitudes in our m_{5007} measure (well above Me06 uncertainties of 0.06 mag), implying an overestimation of the flux of $\sim 9.6\%$. This can be explained by an incorrect modulation efficiency estimation, that could not be firmly tested in Section 2.3.3.

objects having a detected Hα line, 445 could be found in Ma18.
Again, we compared the angular separation in the match and the correspondence in terms of velocities and measured flux, respectively in Figures 3.21 and 3.22. The angular separation shows a median error of 0.29" (less than one pixel scale) due to the necessity of rounding pixel positions when extracting spectra. Outliers having a larger separation (above 0.6") correspond to extended sources, where the visually determined position by Ma18 can be different than our automated SNR optimization.
Velocities are in very good agreement, with a median error of 0.34 km.s^{-1}. The dispersion of 3.3 km.s^{-1} is higher than the uncertainty quoted in Ma18 (2.21 km.s^{-1}), and could be due to the slight misalignment on the positions.
Concerning the flux, a linear fit of the scattered data indicates a slope of 0.949. This disagreement is actually due to our different method to estimate the aperture flux loss (see Section 3.3). When using the 1.88 value quoted by Ma18 instead of ours, the data becomes compatible with a line of slope 0.999.

These 445 cross-matches also imply that 352 sources from Ma18 catalog were not detected in the SN2 data, i.e. do not emit in the [OIII] or Hβ lines. Very Low Excitation (VLE) PNe as described in Frew and Parker (2010) can have no [OIII] emission. They could also be Hα stars as discussed by Prichard et al. (2017). The compared study of such stars with PNe would nicely complete the analysis of their implication on the stellar evolution and ISM enrichment of the galaxy, but is beyond the scope of this thesis.

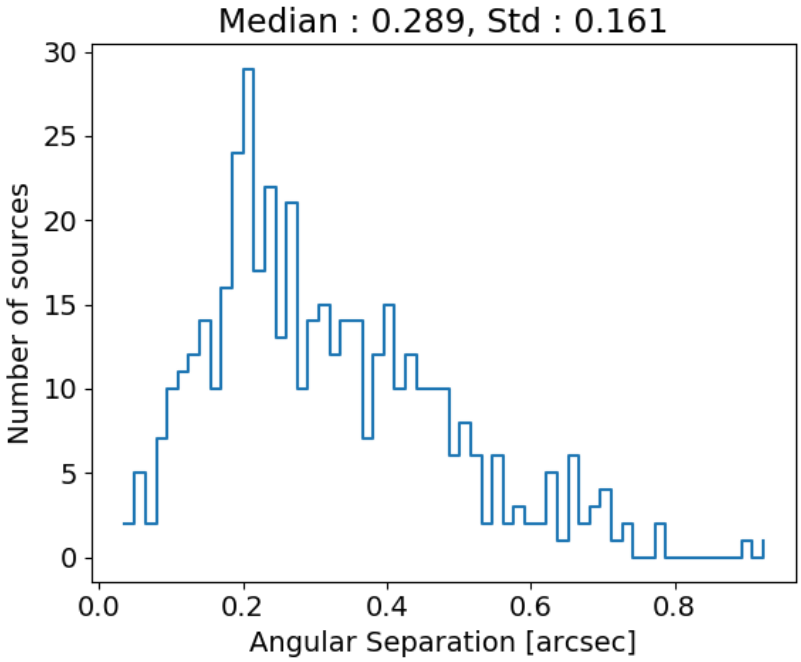

Figure 3.21: Histogram of the angular separation in arcseconds between our position estimates in the SN3 cube and their matches in Ma18 catalog. The median error of 0.29" comes from the rounding of pixel positions.

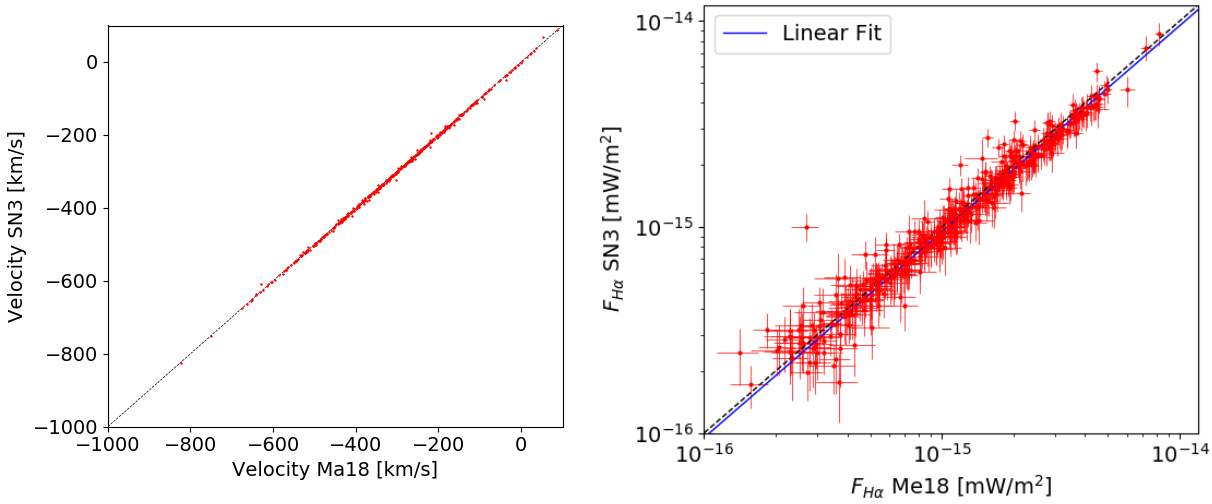

Figure 3.22: Left : Scatter plot of Ma18 velocity against our measurement. The data is in very good agreement with the dashed black line representing the one-to-one relation. The velocity difference is centered on 0.34 km.s^{-1} with a dispersion of 3.3 km.s^{-1}. Right : Scatter plot of the flux measured in the Hα line by Ma18 against our measure, with error bars. The blue line represents a linear fit of the data, with a slope of 0.949 (and an intercept of 7.09×10^{-45}, below the computer numerical precision). When using Ma18 aperture correction factor of 1.88 instead of our source-dependent estimate, the data becomes compatible with a line of slope 0.999.

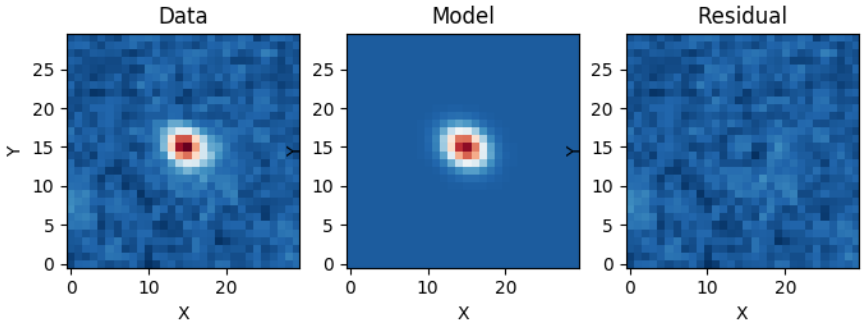

Figure 3.23: Example of the 2D fit of a source on the flux map computed as in Figure 3.14. The model used is a 2D Gaussian, and the goal is to measure the axis ratio between x and y FWHMs. Here, $\mathrm{FWHM}_x = 4.38$ and $\mathrm{FWHM}_y = 3.45$, implying a ratio of 1.27, i.e. a 27% elongation.

3.5 Separating extended sources

For now, our catalog contains both point-like and extended sources. In Section 3.3, we already used some criterion to discard non-point like emitters. But as mentioned there, this procedure also discarded real point-like sources having a close by bright neighbor, as well as those where the background gradient was badly estimated in the 30×30 flux map (especially in the close to the center where it varies a lot), inducing a bias in the growth function.
To improve the distinction, we would like to estimate the ratio of the elongation of the PSF in each direction. Even where the PSF is deformed, we should be able to distinguish between elongated point-like sources and other non-round sources like gas filaments or HII regions. In our flux growth model before, elongation on the x and y direction already appear as free parameters, but are strongly correlated. We therefore re-fitted a full 2D Gaussian function on the previously defined flux map (see Figure 3.14), to get better estimates of the x and y FWHMs (see an example in Figure 3.23). It appears that the worst deformations of genuine point-like sources can lead to a factor of about 2 between the two directions. The elongation seems to have a preferred orientation, as the PSF always appears to be stretched toward the center of the FOV. An improvement of the method would be to make our FWHM ratio cut depend of the position of the source in the cube. For now, sources with a FWHM ratio not included in the [0.5; 2] range in none of the 2 cubes were classified as extended (411 sources).

3.6 Limit of detection

For now, we considered a line as detected if its signal to noise ratio was higher than 3. This is kind of arbitrary and may not reflect the real nature of the detection. We tried to estimate a more sensible threshold by fitting the [OIII]5007 SNR histogram of our detections, which should show two distinct populations, noise and sources. We show in Figure 3.24 a Gaussian fit of the histogram. We observe a steep decrease in the number of detections between SNR 3 and 5, that is well fitted by a Gaussian, and that is probably populated by false detections. The fit indicates that our catalog is dominated by noise up

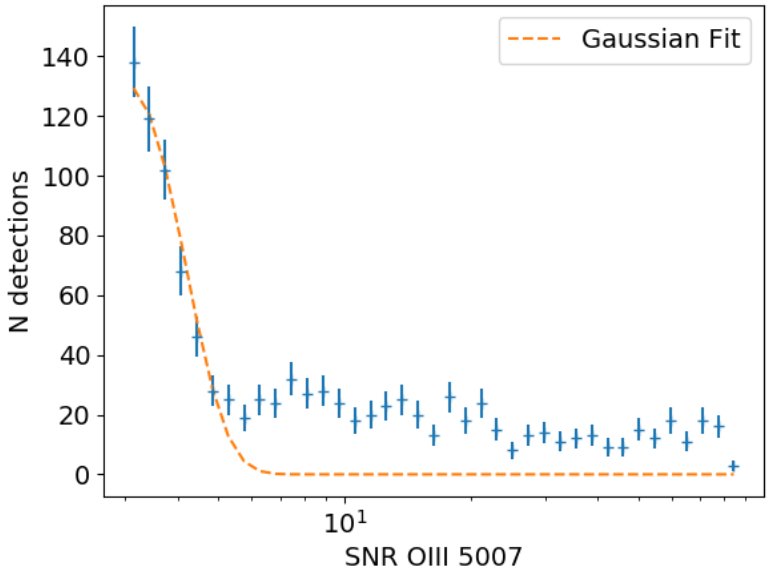

Figure 3.24: Histogram of the measured Signal to Noise ratio of the [OIII]5007 line of our detections. Error are assumed Poisson distributed, which is correct at low SNR where the bins are well populated. A Gaussian function efficiently fits a "false positive" population at SNR < 5. The noise is negligible from a SNR of 6 onwards.

to SNR ~ 5 and that detections are truthful above 6. To be able to discuss our detection limit later, we keep all data points in our catalog, while keeping in mind that below a SNR of 6 we might be looking at noise.

Chapter 4

Results

4.1 Diagnostic Diagrams

With the combined observations of our SN2 and SN3 filters, we are able for the first time to plot complete diagnostic diagrams for emission-line detections in M31. We present here the combination of 3 diagnosis diagrams, that have been used in the literature to efficiently classify PNe and separate contaminant population like Super Novae Remnants and HII regions.

4.1.1 SMB diagram

The Sabbadin, Minello, Bianchini (1977) (SMB) is described by Frew and Parker (2010) as a powerful tool to classify emission-like objects. We show in Figure 4.1 our detections plotted on this diagram.
We observe a shift of our data with respect to Galactic objects observed by Frew and Parker (2010), both in Hα/[NII] and Hα/[SII] ratio. In fact, we miss the Type I PNe identified in the Galaxy by Kingsburgh and Barlow (1994), that are expected to have strong [NII] emission. Jacoby and De Marco (2002) analyzed PNe in the Small Magellanic Cloud and found on the contrary an excess of Type I PNe. They found a correlation between an increase of the [NII]/Hα ratio (a possible characteristics of Type I PNe, known to be nitrogen rich) and the decrease of the PNe magnitude. They argue that these type of PNe, presumably descending from more massive stars, contain a fair amount of dust, lowering their apparent brightness. Because of the strong luminosity gradient of M31, our sensitivity is low and the completeness limit of our sample is $\sim 23.5\,\mathrm{mag}$ in the m_{5007} relative magnitude (see Section 4.2), with the faintest objects having $m_{5007} = 25$. We might thus miss this type of PNe if Jacoby and De Marco (2002) claims are valid.
But this is probably not the only reason. Indeed, these massive stars progenitors of Type I PNe must come from star forming regions. As discussed in the next section, we do detect signs of star formation in M31's bulge. Indeed, we do have compact HII region candidates (see Section 4.1.3), and we detect Hα gas in this region. However, this star formation activity is different from the large locus of star formation detected further in M31 disc e.g. in the 10-kpc ring (Amiri and Darling, 2016; Azimlu et al., 2011; Kang et al., 2011). It is probably similar to the very compact HII regions, detected by Urquhart et al. (2013), in the Galaxy, suggesting that the star formation activity is occurring in small gas complexes. This is supported by the detection of small molecular gas clumps in this region (Melchior and Combes (2017), Dassa-Terrier et al. in prep.). We can tentatively argue that M31's

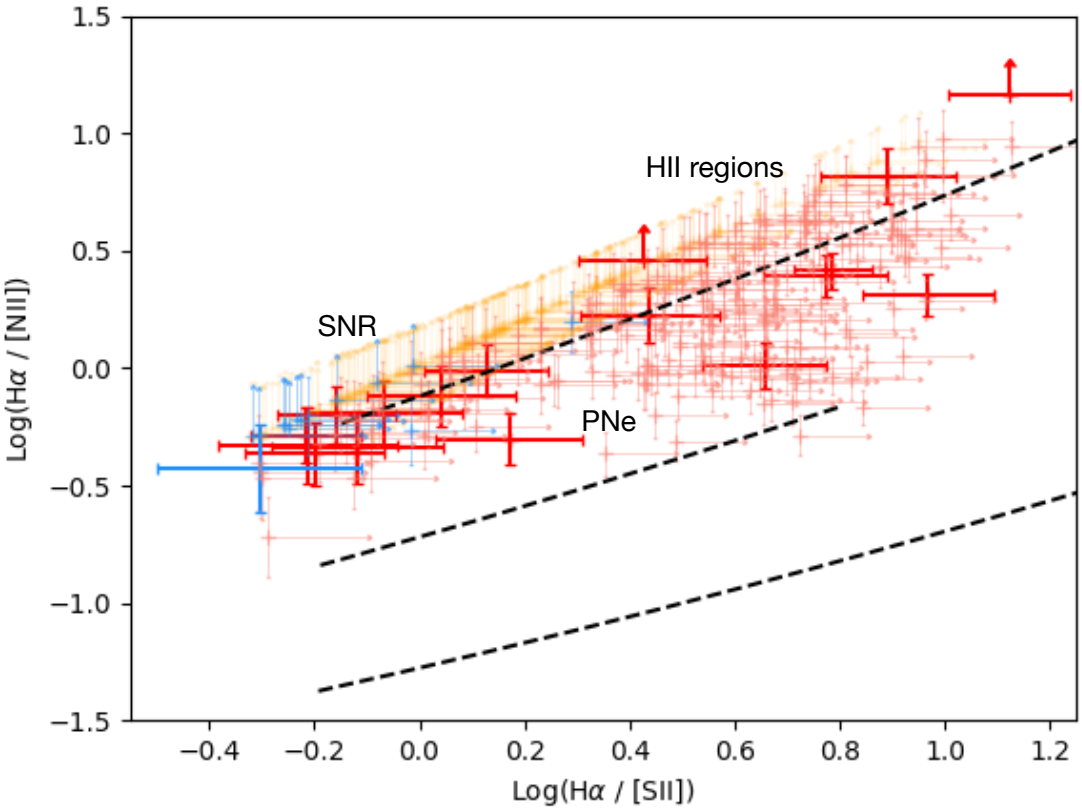

Figure 4.1: Our sources plotted on the SMB diagram (Sabbadin et al., 1977), with error bars. We used upper limits on the X axis when none of the [SII] doublet lines were detected, and upper limits on the Y axis when none of the [NII] doublet lines were detected. Orange data points have upper limits in both X and Y direction. Light red points only have an upper limit on the X axis. Red crosses have an upper limit of the Y axis or none. Blue color has been used for extended sources (see Section 3.5). Black dashed line have been replicated from Frew and Parker (2010). In particular, the middle one is supposed to indicate the position of Type I PNe and is not populated here.

bulge region having a low star formation activity, this region may lack of massive stars progenitors and thus of Type I PNe.

We can pursue using the SMB diagram as a classifier. First, the three detections having a Hα/[NII] ratio above the highest dashed line could be potential HII-regions. One of them also falls in the HII region of the BPT diagram (see Sec. 4.1.3). We flag these three sources.

The bottom left blue data point corresponds to a previously detected Supernovae Remnant, classified by Lee and Lee (2014) and confirmed in Ma18. We show its flux map and spectra in Figure 4.3. The other red detections in this area could also be Supernovae Remnants, and we flag them for now in consequence.

Due to the high uncertainty on the measurements, especially on the [SII] lines, no efficient classification can be made for the rest of the sources, and they are all considered at this point as PNe candidates. We show again in Figure 4.2 the SMB diagram with our categorized candidates.

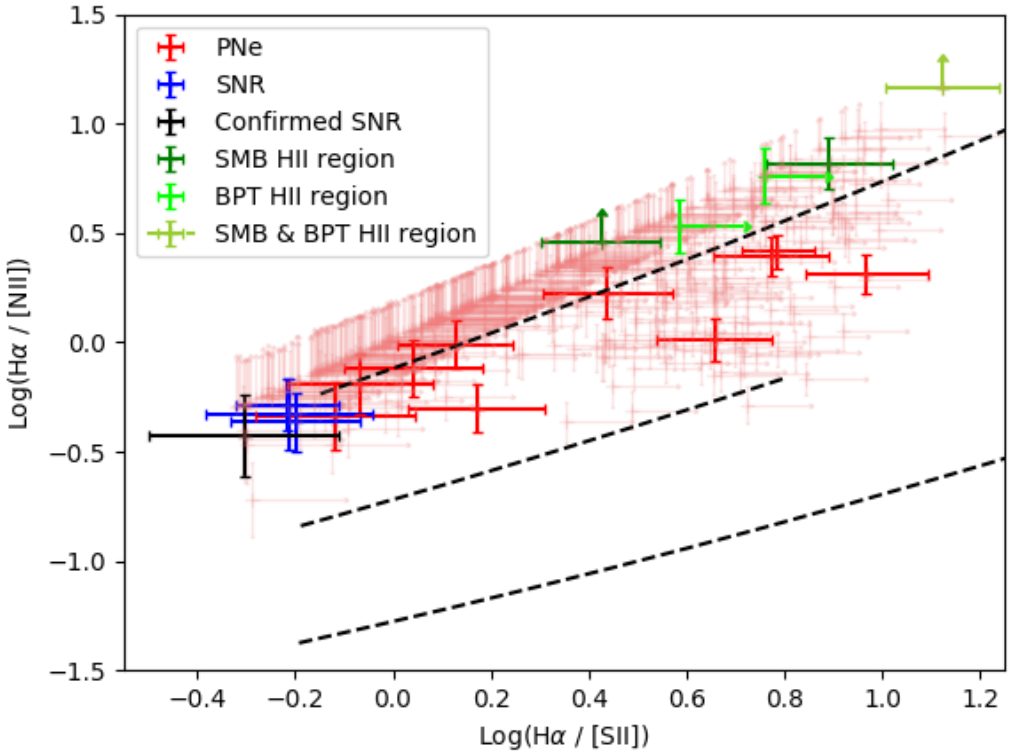

Figure 4.2: SMB diagrams with classified sources. The previously confirmed Supernovae Remnant is shown in black, and new candidates, based on this diagram, are shown in blue. We plot in dark green two HII regions candidates estimated from this diagram, and in light green two candidates estimated from the BPT analysis (see Sec. 4.1.3). The 'olive' data point is an object classified as Hii-region both in the SMB and BPT diagrams. All the other red dots are considered as potential PNe at this point.

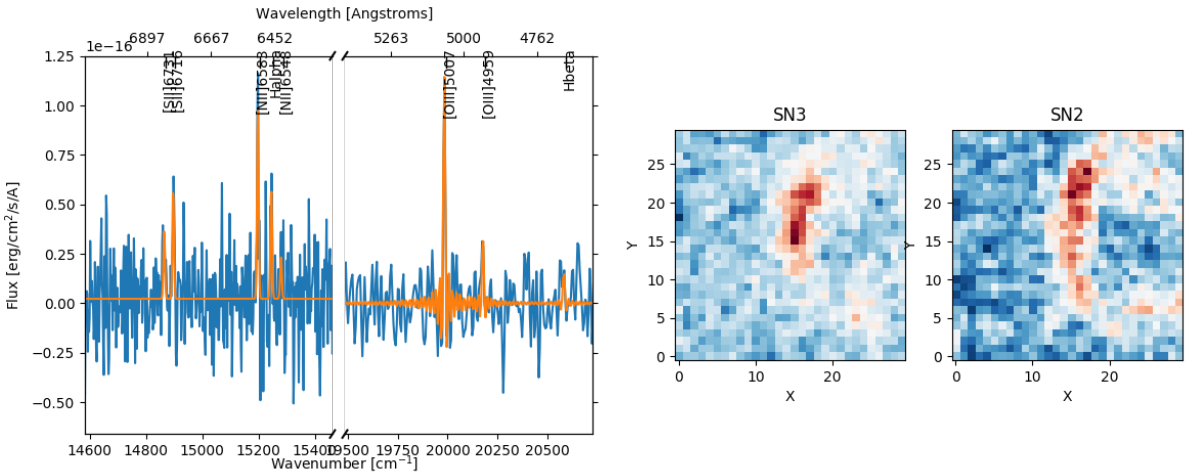

Figure 4.3: Left : Spectra of the Supernovae Remnant in both SN2 and SN3 cube. The orange line is ORCS fit of the lines. Right : Flux map obtained like in Section 3.3. This object has already been classified by Lee and Lee (2014) (#41) and Ma178 (SNR3).

4.1.2 [OIII]-Hα emission-line space

Me06 and Herrmann et al. (2008) have used cuts in the [OIII]-Hα emission-line space to define PNe regions. The idea behind this plot is that HII-regions usually have stronger Hα than [OIII]5007 emission, at least for the brightest objects. Indeed, Frew and Parker (2010) warns for very-low excitation PNe where Hα can dominate. One should thus be able to distinguish HII-regions from PNe in the brightest side of the diagram. However, a recent study of Davis et al. (2018) has shown how such a diagram can not disentangle PNe from Supernovae Remnants objects. We show in Figure 4.4 our detections plotted in this diagram. We converted Herrmann et al. (2008) classification curve from absolute to relative magnitude using

$$M[\mathrm{OIII}] = \mathrm{m}_{5007} - A_V - \mu \tag{4.1}$$

with an extinction of $A_V = 3.1E(B-V) = 0.19\,\mathrm{mag}$ with $E(B-V) = 0.062$ mag (from Schlegel et al. (1997)) and a distance modulus $\mu = 5\log D - 5 = 24.38$ mag with $D = 750$ kpc (from Freedman (2000)).
The HII-region candidate found in both SMB and BPT diagram is the only one falling under Herrmann et al. (2008) classification curve, arguing even more for its classification. The two SMB classified HII-regions fall however in the PNe zone, despite their relatively low m_{5007} magnitude. They become less plausible HII candidates. Nothing can be said about the two BPT classified HII regions, as they are very faint.
We confirm Davis et al. (2018) claims, as the confirmed and the 3 candidates Supernovae Remnants are all in the PNe region.

4.1.3 BPT Diagram

Finally, the Baldwin, Phillips & Terlevich (Baldwin et al., 1981) diagram is also an efficient tool to categorize our detections. It has been primarily used to separate star-forming galaxies (dominated by HII-regions where the ionization source are newly born stars), and

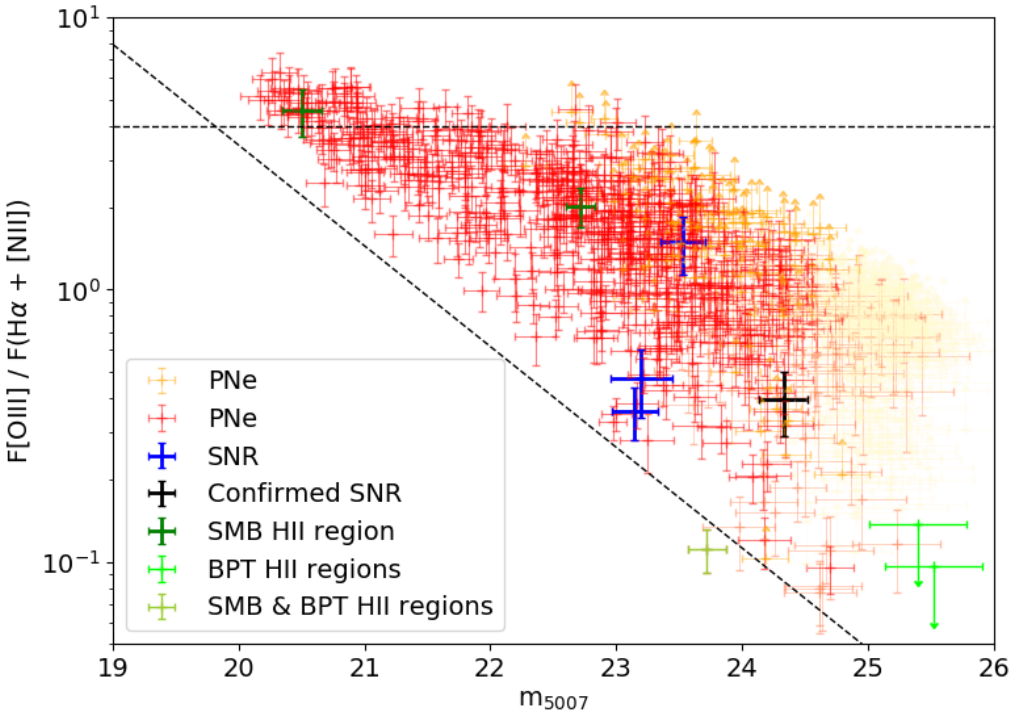

Figure 4.4: Flux ratio F([OIII]5007)/F(Hα + [N II]) with respect to the relative m_{5007} magnitude. The color-code is the same than 4.2. Data points in orange are the one having only an upper limit on the Hα + [NII] flux. Data with a signal ratio on the [OIII]5007 line below 6 are shown in fainter colors. Dashed black line is the one reported in Herrmann et al. (2008), converted in relative magnitude using the relation 4.1. We highlight the supernova remnants and HII regions candidates described in Section 4.1.1.

Active Galactic Nuclei (AGN) (where ionization comes from the hot accretion disk around the central Black Hole), but is also well suited to distinguish HII-regions from PNe (see Frew and Parker (2010) and Kniazev et al. (2008)). We show in Figure 4.5 a first BPT diagram, using the [NII]/Hα ratio.
As expected, our detections mostly fall in the PNe region. 13 sources lie below the dashed black line and present the characteristics of HII-regions, 3 of them having a measured velocity within less than 5 km.s^{-1} away from the gas velocity (measured on the background spectrum (see Sec 3.1.3)). This 3 objects could be young star forming regions still kinematically linked to the gas of the disk. One of them matches one of the identified HII region from the SMB diagram (see Sec. 4.1.1), and the two others have been plotted on previous diagrams (see Fig 4.2 and 4.4) and are consistent with their classification. We classify them definitely as HII-regions, and remove them from our PNe candidates sample. These point-like star forming regions have not been detected before, and may have been missed by surveys not having the combined spectral and spatial resolution we have. If these detections are confirmed, this is coherent with the detection of dense molecular gas in this region (Melchior and Combes, 2016), as well as small molecular clumps with IRAM interferometric observations (Melchior and Combes, 2017, Dassa-Terrier et al., in prep).

The case of two most right extended sources (blue with a lower limit on the [NII]/Hα ratio) is interesting: the top one is the supernovae remnant from Lee and Lee (2014) already discussed previously. The other one, after visual inspection of the flux map, is very extended spatially and could be a gas filament.
All the other sources are presumed to be PNe candidates. We plot again the BPT diagram to better identify the groups. The categories obtained with the SMB diagram (see Section 4.1.1) are plotted on top, with the same color code than in Figure 4.2. The two HII-region candidates identified in the SMB diagram fall in the PNe region, which confirms the previous [OIII]-Hα diagnosis (see Sec 4.1.2). [SII] lines are very weak and are detected only in a few sources (see Table 3.5). The SMB classification strongly relies on [SII] measurements, which can explain this biased classification. The HII-region matching SMB and BPT classifications is however conforted in its status.
The supernovae remnants classified on the SMB seems to gather in a well-defined region of the BPT. We found no strong classification of Supernovae Remnants based on BPT in the literature, but we note that Frew and Parker (2010) Supernovae Remnants were also found on this right hand side of the diagram. A detailed analysis of the sources detected in this region could strengthen the detection of several supernovae remnants.
Last, the BPT diagram using the [SII] emission-line is displayed in Figure 4.7. We only have 18 sources having a measured [SII] flux higher than 3σ, and the diagram is mostly populated by upper limits. Nevertheless, the classification of our HII-regions and supernovae remnants seems comforted.
In the end, and for the rest of the analysis, we put aside the 3 compact HII regions candidates found in the BPT diagram, as well as 4 the supernovae remnants (3 candidates and one confirmed) and the extended sources (the one having a FWHM ratio between x and y axis not in the range [0.5; 2], see Sec 3.5. We resume the classification numbers in Table 4.1.
Our final PNe sample thus consists of 766 source candidates, with 527 being confirmed by a Signal to Noise ratio higher than 3 in the [OIII]5007 line. This extends the previously known sample of Me06 in the same FOV by at least 60%. This large sample will enables us to conduct now a detailed study of the Planetary Nebulae Luminosity Function.

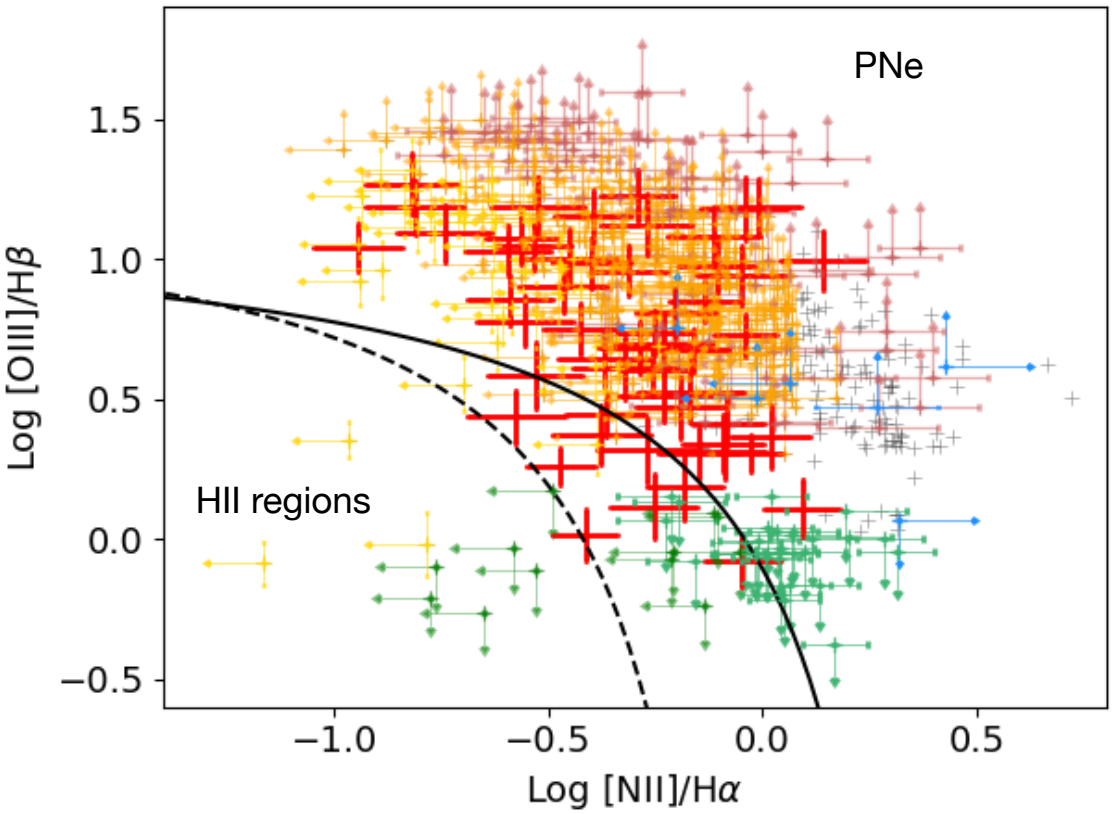

Figure 4.5: BPT diagram, showing the [OIII]/Hβ flux ratio versus [NII]/Hα flux ratio. Data with a SNR lower than 5 are displayed as faint black crosses. An upper or lower limit is displayed when the flux could not be measured at a SNR higher than 5. Faint red points indicates an upper limit on the Hβ and Hα or Hα only lines. Orange is for upper limit both on $H\beta$ and [NII] flux, and yellow for [NII] only. Green stands for an upper limit in the [OIII] flux and eventually [NII]. Blue corresponds to extended sources as defined in Sec 3.5. Finally, red crosses are data where all four fluxes could be determined. The classification curves come from Kewley et al. (2001) (filled black line) and Kauffmann et al. (2003) (dashed black line).

Category	Number of sources
Supernovae Remnants	4
HII compact regions	3
Point-like PNe candidates	766
Point-like PNe candidates with SNR [OIII]5007 $>$ 6	527

Table 4.1: Numbers of sources included in the different classified categories. The distinction of the PNe sample on the Signal to Noise ratio value is based on the analysis of Section 3.6.

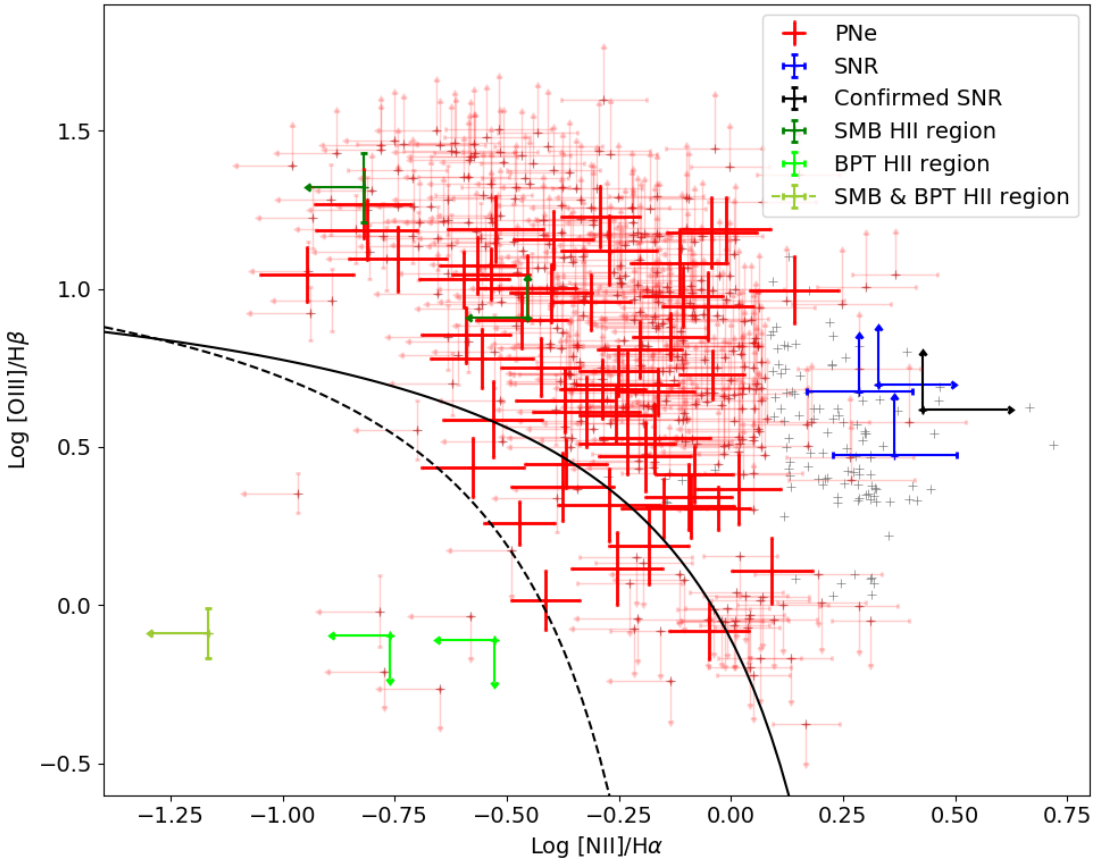

Figure 4.6: BPT diagram with our different source candidates, with the same color-code than in Figure 4.2. The two SMB classified HII-regions are discarded and considered as PNe, as they fail both the [OIII]-Hα and BPT classifications. Supernovae remnants seems to gather in a well defined region of the BPT, where Galactic supernovae remnants of Frew and Parker (2010) were also found.

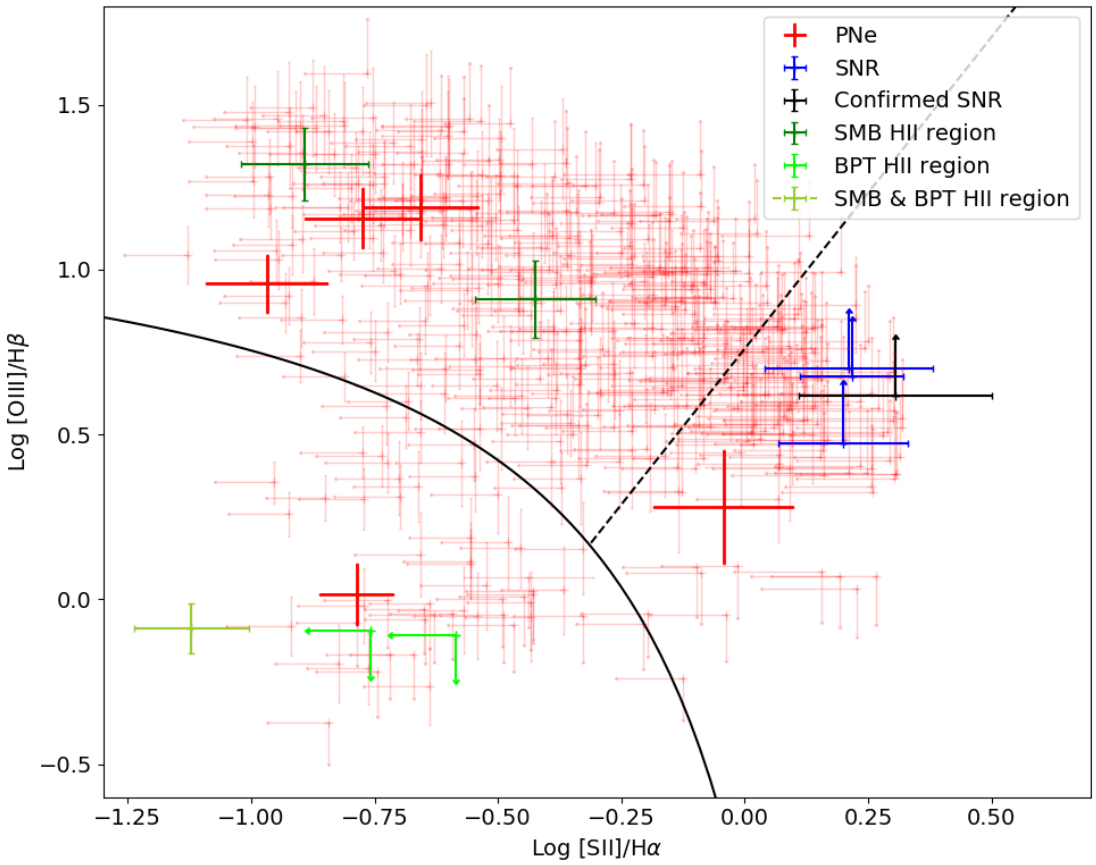

Figure 4.7: BPT diagram with the [SII] flux ratio. The color-code is the same than Fig 4.2. Classification curves come from Kewley et al. (2001). The diagram is mostly populated with upper limits and no strong statement can be made. Nevertheless, supernovae remnants and BPT classified HII-region seem to occupy well defined regions of the diagram, confirming their nature.

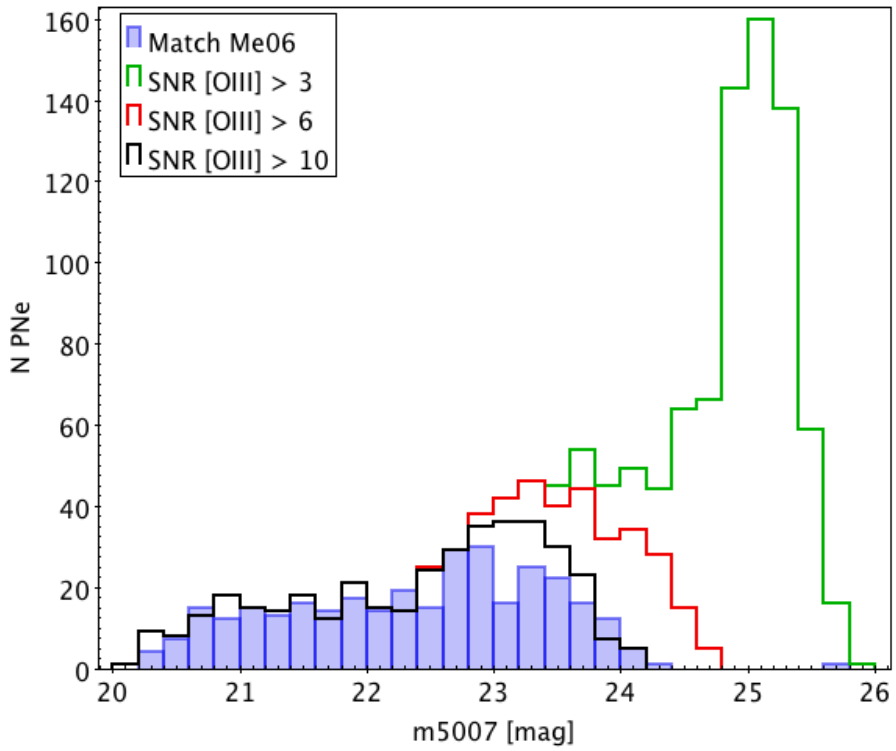

Figure 4.8: Distribution of the relative magnitude m_{5007} of our detections. In blue, Me06 magnitudes of the 318 sources matching our catalog. In green, red and black, our detections having respectively a signal to noise ratio higher than 3, 6 and 10.

4.2 Planetary Nebulae Luminosity Function

4.2.1 Completeness limit

We show in Figure 4.8 the distribution of the relative magnitudes m_{5007} for different threshold on the signal to noise ratio of the detections, and compared to m_{5007} magnitudes reported by Me06 that matched our detections. We remind from Section 3.6 that all sources are reliable above a SNR of 6, while they are strongly contaminated by noise between 3 and 5. Because of the strong luminosity gradient in M31, our completeness limit should be determined as a function of the position in the FOV. For now, one can estimate that we are complete to $m_{5007} \sim 23.5$ everywhere in the FOV, while still detecting objects up to $m_{5007} = 25$.

4.2.2 The bright-end cutoff of the PNLF

The Planetary Nebulae Luminosity Function (PNLF), describing the number density of PNe over a range of magnitudes, has a remarkably uniform shape, first proposed by (Ciardullo et al., 1989) as :

$$N(M_{5007}) \propto e^{0.307 M_{5007}} \left(1 - e^{3(M^*_{5007} - M_{5007})}\right) \tag{4.2}$$

where M_{5007} designates the absolute magnitude of the flux contained in the [OIII]5007 emission-line, and M^*_{5007} the bright-end cutoff of the population. This form has been

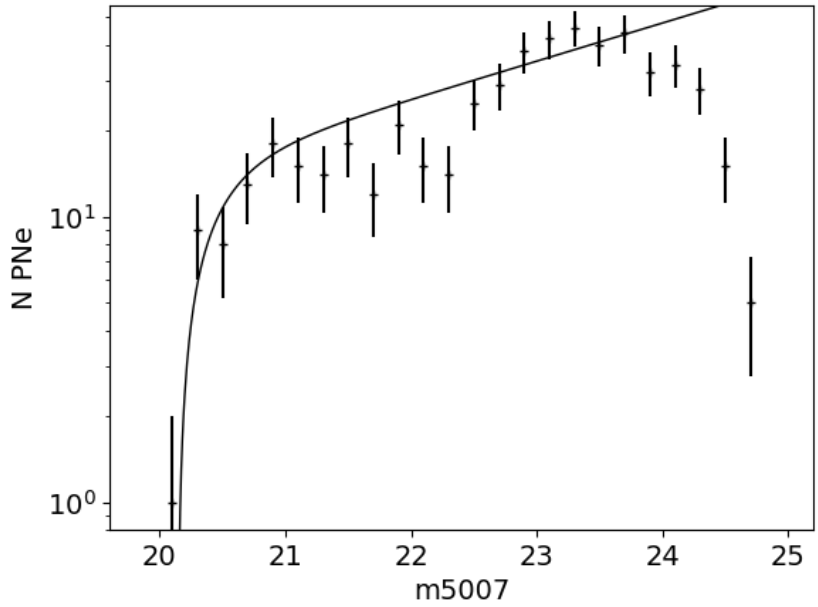

Figure 4.9: Fit of the PNLF. The distribution is populated by detections having a SNR in the [OIII]5007 higher than 6. Noise in the bins is estimated as Poisson distributed. We constrained the fit only on data up to our completeness limit, i.e. 23.5. From this fit, we estimated $m^*_{5007} = 20.14 \pm 0.248$.

used to successfully fit observations in many different systems. In particular, the value of the bright-end cutoff ($M^*_{5007} = 4.47$, Ciardullo (2012)) seems constant across all samples, independently of the galactocentric radius of the survey, and this has been used as a standard candle for distance measurements (e.g. Feldmeier et al. (1997) on spiral galaxies, Herrmann et al. (2008) on face-on galaxies), with a precision of $\sim 10\%$.
Because all our objects belong to Andromeda, and can be considered at the same distance, we can use this to fit shape to fit on relative magnitudes. We show in Figure 4.9 our fit of the PNLF.
The fitted bright-end cutoff of $m^*_{5007} = 20.14 \pm 0.248$ is in very good agreement with values estimated by Me06 (20.2 ± 1) and Ciardullo et al. (1989) (20.17). Using 4.1, one can even deduce back Andromeda's distance, as:

$$\log D = \frac{m^*_{5007} - M^*_{5007} - A_V + 5}{5}$$

yielding a distance $D = 765 \pm 87\,\mathrm{kpc}$, in very good agreement with literature values (e.g. $780 \pm 40\,\mathrm{kpc}$, de Grijs and Bono (2014)).
This universality is problematic. Marigo et al. (2004) have modeled the stellar evolution of PNe, and argue that the bright-end cutoff of the PNLF is populated by PNe whose progenitors are $\sim 2.5\mathrm{M}_\odot$ stars. Such stars are only present in systems of age $< 1\,\mathrm{Gyr}$, and are expected to be linked to the last burst of star formation. If this can be seen in galaxies with recent and on-going star formation, it is problematic to see such bright objects in old elliptical galaxies. For old stellar populations, Marigo et al. (2004) predicts a m_{5007} that could be 5 magnitudes dimmer, which is not observed. An alternative has been proposed

by Ciardullo et al. (2005) that part of the PNe originate from binary systems where mass is accreted from a companion, which could explain the presence of more massive progenitor in old stellar population. It would be interesting to compare our sample with X-ray emitting sources, that are often binary stars, to see if a spatial correlation can be found.
In the following, we further explore the PNe luminosity function and provides arguments that PNe associated to disc stellar populations are probably part of our catalog.

4.2.3 A PNLF made of two populations

The shape of the m_{5007} distribution requires more attention. Indeed, there is a departure from the fitted PNLF curve around ~ 22 mag, i.e. 2 mag below the brightest PNe. Such a dip in the PNLF has already been observed in the SMC and the LMC (Jacoby and De Marco (2002), Reid and Parker (2010)), and Rodríguez-González et al. (2015) have observed this bimodality in several galaxies including M31. Merrett et al. (2006) discuss a slight dip in the PNLF of M31 in the range 0.6°-0.8°, lying inside the 2.5 σ boundaries of the model. According to Jacoby and De Marco (2002), such a dip is usually the sign of a young population of PNe, and one could recover the time of the last star formation event from the position of the dip.
To fit the two-component PNLF, we used Rodríguez-González et al. (2015) approach. Because of the necessity to use most of the PNLF to fit the bimodal distribution (usually, only the bright end is used for the fit), they propose to consider the cumulated luminosity distribution and model it as:

$$N_c(m; m_1^*, m_{cut}, m_2^*) \propto \int_{m_1^*}^{min(m,m_{cut})} N_1(m'; m_1^*)\mathrm{d}m' + \int_{m_2^*}^{m} N_2(m'; m_2^*)\mathrm{d}m' \qquad (4.3)$$

where N_1, N_2 designates the classical distribution from Eq. 4.2. From this fit, one can recover the bright-end cutoffs of the two populations, as well as the magnitude cut separating the two components. Figure 4.10 displays results of such a fit on the cumulated distribution.
The two-mode model correctly fits the data up to the completeness of m_{5007} of 23.5, yielding the values $m_1^* = 20.23 \pm 0.07$, $m_{cut} = 22.67 \pm 0.22$ and $m_2^* = 19.97 \pm 0.03$. The bright-end cutoff of the brightest population corresponds to the one estimated previously. m_1^* and m_{cut} estimates are in good agreement with the one quoted in Rodríguez-González et al. (2015). The value found for m_2^* is however quite different from the one obtained by Rodríguez-González et al. (2015) (22.17 ± 0.49), and could be due to an error in the model implementation. This does not affect the magnitude cut that effectively mark the dip in the PNLF and in which we are interested here.
We used this fitted magnitude cut to separate our two populations and analyze their spatial distribution. We show in Figure 4.11 the two components plotted separately on an SDDS image of the FOV. The bright ($m_{5007} < 22.7$) PNe population does not exhibit the same spatial distribution at the faintest one ($m_{5007} > 22.7$), which is surprising in our FOV dominated by the bulge light (Courteau et al., 2011). The faint population seems to randomly populate the FOV, while the brightest shows a structure.
We discuss in the following different possible explanations.

Dust extinction

It has been long thought that due to the strong inclination of M31 disc (77 degrees, Corbelli et al. (2010)), dust extinction should be visible in the (spherical) bulge stellar population

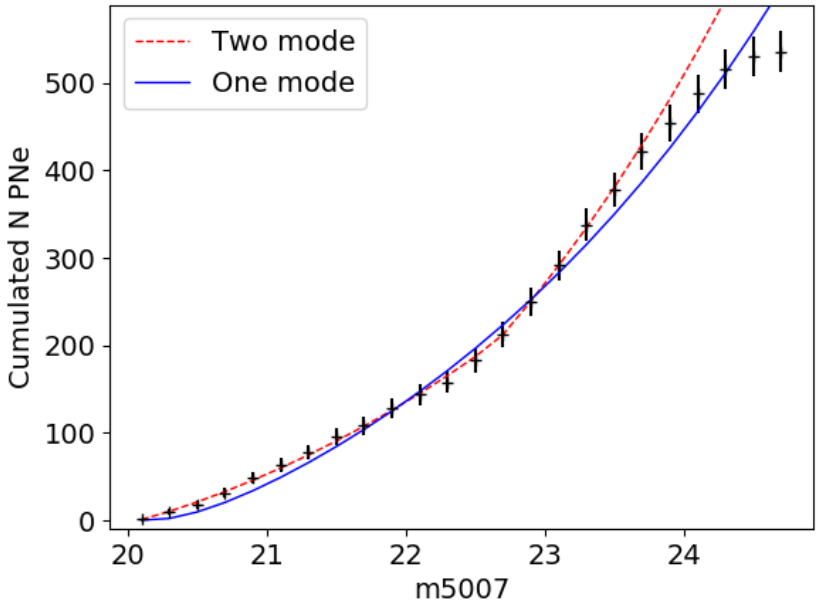

Figure 4.10: Fit of the cumulative PNLF with two different models. The one mode designates the integration of Eq 4.2, the two mode designates the model by Rodríguez-González et al. (2015) (see Eq. 4.3). Only sources with a SNR on the [OIII]5007 higher than 6 were used here.

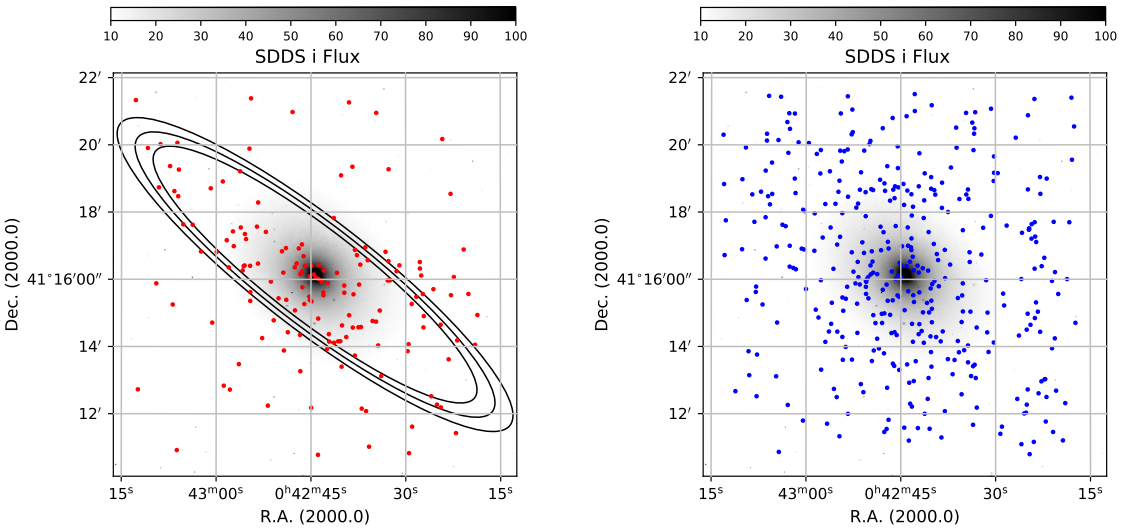

Figure 4.11: The spatial distribution of the bright (resp. faint) PNe population, i.e. with $m_{5007} < 22.7$ (resp. $m_{5007} > 22.7$) is plotted on the left (resp. right) panel over a SDSS image of the FOV in the i-band. We plotted ellipses with Andromeda's inclination and position angle ($i = 77°$, Corbelli et al. (2010), $PA = 38°$, de VAUCOULEURS (1958)) on top of the bright distribution to highlight its possible belonging to the disc.

for Novae (e.g. Shafter and Irby, 2001) and PNe (e.g. Merrett et al., 2006), and in the halo MACHO population used for gravitational microlensing searches (Crotts, 1992; Kerins et al., 2001, 2006). However, no clear asymmetry has been found. In addition, the inner region hosts very little gas (Braun et al., 2009; Chemin et al., 2009; Nieten et al., 2006) and hence very little dust and related extinction (Melchior and Combes, 2011; Melchior et al., 2000). Such an asymmetry has not searched for but has never been detected. An et al. (2004) have shown that there is an asymmetry in the variable stars distribution due to the main dust lanes present in the stellar disc. In parallel, the Novae distribution is known to follow the light distribution (Shafter and Irby, 2001). Ciardullo et al. (1987) and Capaccioli et al. (1989) found that Novae in the central region mainly come from the bulge. As there is very little gas in the bulge, this is coherent.
In addition, our results are consistent. Indeed, the faint PN component seems to follow the bulge light, with a symmetric distribution, while the bright PN component does not present a circular geometry. If the asymmetry of the bright component were due to the dust extinction, we would expect that it affects the bulge component.

Superimposition of halo debris

Numerous relics of past interactions have been detected in the outer parts of the Andromeda galaxy (McConnachie et al., 2009). The main disc exhibits an enhanced star formation activity in a ring at 10 kpc (Ford et al., 2013) and the central part is atypical. Different simulations efforts have been undertaken to understand the main streams detected in its outskirts. Hammer et al. (2018) explain the actual geometry with a single major merger, while the main paradigm suggests several minor-merger events (e.g. Bullock and Johnston, 2005; Fardal et al., 2013; Kirihara et al., 2014; Sadoun et al., 2014). Komiyama et al. (2018) studied the M31 stellar stream and halo structure with Subaru telescope. They found that the southern part of the stream is $\sim 20\,\mathrm{kpc}$ closer to us relative to the northern part. Miki et al. (2016) estimate the mass of the progenitor in the mass range 5-50$\times 10^8 M_\odot$. Hence, unless the progenitor galaxy has a mass comparable to M31, it is difficult to account for about 100 PN from the halo superimposed in front of the bulge. In addition, following Merrett et al. (2006), we do not detect any outliers in our PNe velocity distribution (see Fig 4.11) which could belong to the stellar streams.

Disentangling bulge and disc components

The spatial distribution of the bright and faint PNe populations could be related to M31's structure. In our FOV, the disc is superimposed on the bulge. We plotted ellipses having the same inclination and position angle as the disc on top of the bright PNe distribution. It seems that there is a little over-density of sources along these ellipses, indicating that such PNe could actually belong to the disc. On the other hand, the fainter population has a more random distribution, as expected for objects belonging to the old bulge. This tentative explanation would solve the bright-end cutoff universality issue, as no bright young PNe actually populate the old bulge; they come from the disc, where star formation is in process and where such PNe could form. A careful statistical analysis of the bright PNe distribution, both spatially and kinematically, is needed to bring to light an eventual rotation pattern of the sources, that would prove their belonging to the disc. Such an analysis is strongly dependent on Andromeda's inclination.

Chapter 5

Prospects

5.1 Preliminary Results

The background spectrum, that we have been trying to disentangle from genuine source spectrum since Section 3.1, is a mine of information to study both the stellar population of M31 bulge (in absorption) and its gas content (in emission). Features observed in the background spectrum can in principle be directly related to physical properties of the population, especially age and metallicity. In practice as we will later discuss, this depends on the spectral coverage of the spectra. Dong et al. (2015), for example, has discussed photometric evidences for a metal-rich 300 Myr-1 Gyr intermediate-age population. They estimate that such a stellar population is contributing to 2% (resp. 1%) to the stellar flux at 680 pc (resp. 80 pc). This is very weak and account for the previous lack of direct detection of star formation in this region. Our spectroscopic data contain information on both the stellar and gas contents, and could hence provide new arguments on this subject. Relying the stellar and gas kinematics extracted from VIRUS-W data with 3 arcsec resolution, Opitsch et al. (2017) have recently found evidence of triaxiality of the bulge and claimed the presence of a bar in M31 bulge. This results is based on the mis-alignment of the stellar profile in the bulge region with respect to the main disc. This has been observed since a long time.Beaton et al. (2007) discussed it on the basis of near-infrared data. It is very clear on the Figure 1 of Courteau et al. (2011) that this is probably a bar relic, as the current distribution of gas displays multiple components along the line of sight. Opitsch et al. (2017) report the detection of two peaks in the [OIII]5007 emission line, but they restrict this gas stellar kinematics to a decomposition into 2 disks. In Melchior and Combes (2011, 2016), a few lines of sight have been studied in molecular gas. Two main components have been detected along the minor axis separated by more than 200 km/s on both side of the systemic velocity, while in a bar velocities close to the systemic velocity are expected. The authors discussed that these multiple components could be accounted for by the superimposition of an inner disc and the 0.7 kpc inner ring detected by Block et al. (2006). The gas kinematics in this region is clearly complex. Our two data cubes will provide access to the kinematics but also to the diagnostic diagrams, which should allow a new analysis of this region. It will enable to further explore several still opened questions, e.g. the nature of the ionization processes (i.e. shocks or starburst). There is also some questioning on the rotation of the bulge. Bekki (2010) discuss the origin of the rotational kinematics in the globular cluster system. How does this compare with the stellar kinematics we derive from stellar population? Can we disentangle bulge and disc

components?
The work presented here aimed at solving these questions by studying the background spectra present in our data. Only preliminary results have been obtained, and more work needs to be applied to asses all the claims.

5.1.1 Stellar Population

To extract stellar parameters, we used the algorithm Nburst described in Chilingarian et al. (2006), which has been used to successfully analyze more than 800 000 galaxy spectra from the Sload Digital Sky Survey (SDSS) (Chilingarian et al., 2017). It consists of the generalization of the pPXF method (Cappellari and Emsellem, 2004): on top of fitting the Line-of-sight Velocity Distribution (LOSVD), the algorithm can adjust the star formation history (SFH) of the galaxy. We explicit shortly how the method is constructed.
The procedure is based on the minimization of a χ^2 defined as:

$$\chi^2 = \sum_{N_\lambda} \frac{(F_i - P_{1p}(T_i(SFH) \otimes \mathcal{L}(v, \sigma, h_3, h_4) + P_{2q}))^2}{\Delta F_i}$$

where $T_i(SFH) = \sum_{Nbursts} k_i T_i(t_n, Z_n)$. It takes as input F_i : the flux in a given spectral channel, and ΔF_i the associated uncertainty, and fits the following parameters :

- $\mathcal{L}(v, \sigma, h_3, h_4)$ the LOSVD, depending on the velocity (v), velocity dispersion (σ) and Gauss-Hermite coefficient (h_3,h_4 measuring asymmetries in the profile.
- $T_i(SFH)$ is the linear combination of $Nbursts$ (hence the name) Simple Stellar Population (SSP) templates, depending on age t_n and metallicity Z_n. PEGASE.HR Le Borgne et al. (2004) models computed on a grid of ages and metallicities have been used.
- P_{1p} and P_{2q}, Legendre polynomials accounting from difference in shape between the galaxy spectrum and the SSPs.

As output, one can then get kinematics of the stellar population (velocity, dispersion and asymmetries), as well as the population age and metallicities (eventually of the many star bursts) fitting at best our spectrum.
To be correctly used as input by Nburst, our data needed to be adapted. First, a strong SNR is needed for a correct adjustment of the stellar background features. To reach a SNR ≤ 20 everywhere except in the NW SE corners we had to degrade our spatial resolution to ~ 9.6", by binning spectra in 30×30 boxes. To reduce the influence of sources, the spatial median of these 30×30 spectra was chosen over the mean. A better approach would be to use a SNR dependent binning like the Voronoi method (Cappellari, 2009), and to mask pixels affected by resolved sources. This will be implemented for the publication of this work.
Second, Nburst expects input spectra to be sampled on a regular wavelength axis, meaning that our spectra need to be re-interpolated on such a grid. But this also means a transformation of our LSF : as the ratio $\frac{\Delta\lambda}{\lambda} = \frac{\Delta\sigma}{\sigma}$ is conserved, with λ, σ being respectively wavelengths and wavenumbers, and $\Delta\lambda$, $\Delta\sigma$ the respective line FWHM, one gets that $\Delta\lambda = \frac{\Delta\sigma\lambda}{\sigma} = \Delta\sigma\lambda^2$, i.e. the FWHM is wavelength dependent. As the FWHM also depends on the position on the cube, a full FWHM datacube had to be processed, and Nburst to be adapted in consequence.

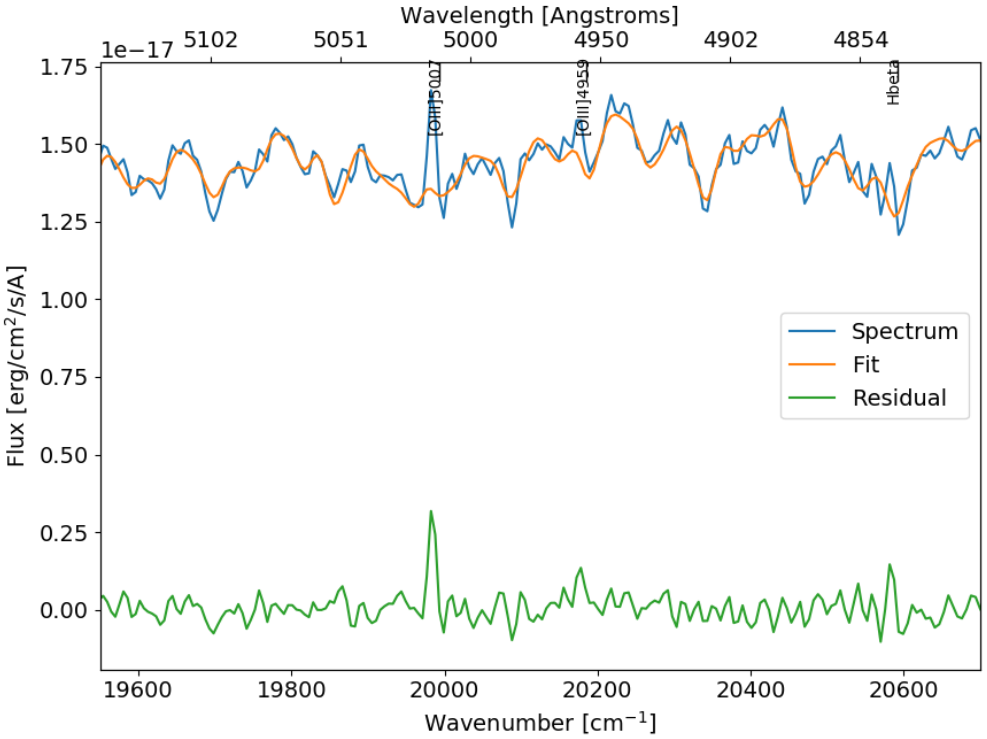

Figure 5.1: Example of a spectrum, its Nburst fit and the residual in the SN2 bandpass. Nburst fits the strong stellar features, and the residuals contains the gas emission. Emission-lines of interest are displayed at Andromeda's systemic velocity.

Last, during the minimization process, SSPs needs to be convolved with the observations LSF, to be matched as closely as possible with the observed spectra. Nburst has been designed to work on the SDSS LSF, i.e. a Gauss-Hermite function. The unsual sinc LSF of the SITELLE instrument has thus been implemented in Nburst, to disentangle LSF effects from stellar features.
A full pipeline has been developed to process these 3 steps directly within then ORCS framework.
We show in Figure 5.1 an example of a spectrum and its Nburst fit in the SN2 bandpass. The fit evaluates correctly the stellar features, and the gas emission is clearly visible in the residuals. The fitted stellar kinematic parameters are meaningful, and maps of the stellar velocity and velocity dispersion are shown in Figure 5.2. Andromeda rotation is visible in the velocity map. Both maps are comparable to Opitsch et al. (2017) and Saglia et al. (2010) in terms of order of magnitudes, validating the fit.
However, deriving other quantities like age and metallicity of the population is different and we did not obtained reliable values yet. First, the small spectral range of our spectra contain little characteristics absorption features constraining the model, preventing these robust estimations. A simultaneous analysis of SN2 and SN3 data would increase our spectral coverage. Fitting SN3 data automatically is still complex. Even less stellar features are present in this redder cube, and the data are contaminated by a lot of sky emission lines and a possible Galactic Hα contribution. Removing these lines is complicated because some of them overlap genuine M31 signals. Besides, combining the two cubes requires a

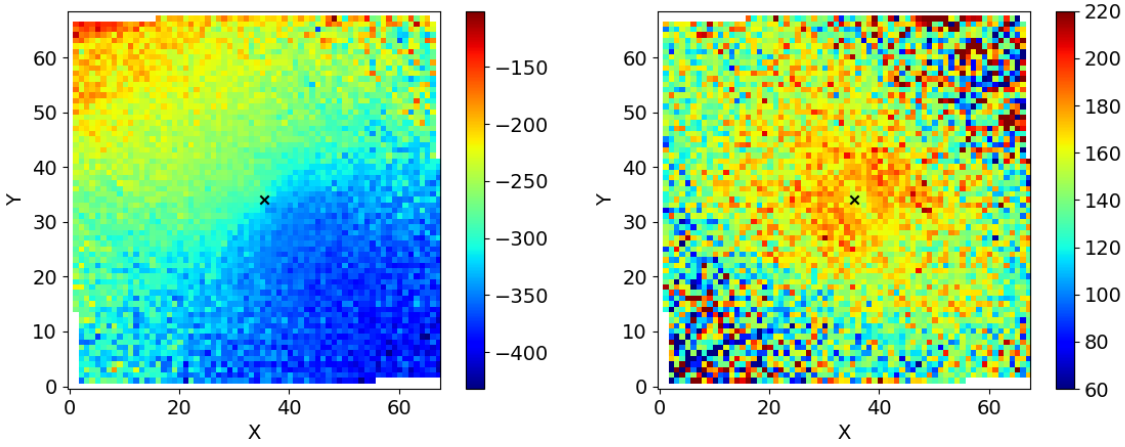

Figure 5.2: Left : Stellar velocity as determined by Nburst from the SN2 data. Right : Velocity dispersion measured with Nburst on this same data. Colormap units are km.s^{-1}. M31 center in displayed as a black cross. The X and Y units corresponds to the coarse binning used to obtain a high SNR in the spectra. The fits seems to have been successful, except in the top right and bottom left corners where the SNR is the lowest. Andromeda rotation is recovered, as well as the systemic velocity of $\sim$ -300 km.s^{-1}. In addition, we detect a sigma-drop in the center.

careful alignment of them, both astrometrically and spectrally speaking that has not been achieved yet. Last, because of the much lowest SN2 resolution, combining the cubes would also mean heavily degrading the SN3 data to match SN2 wavelength grid, and we would lose the benefits of the original resolution. Further investigations need to be conducted to solve these issues.

One possibility considered but not fully exploited is to include in the analysis slit spectra (Saglia et al., 2010), and add external constraints, taking into account that most of the received light originates from an old stellar population ($\geq$12 Gyr, Saglia et al., 2010)

This kinematic field has to be fully analyzed. Indeed, we would like to see if we detect a rotation compatible with the main disc or if we do see the superimposition of several components. We do detect the sigma drop in the central part. Following , this is compatible with an inner disc. This is in good agreement with the molecular component detected within 100 pc of supermassive the black black (Dassa-Terrier et al., in prep) and in the infrared with Herschel data (Smith, Marsh, Eales, 2017, EWASS conference). However, in order to strengthen this result and the subsequently gas analysis, we plan to study the effect of metallicity templates. Koleva et al. (2008) discussed the possible degeneracy between the velocity dispersion and the metallicity. We are also aware that possible template mismatches can introduce biases in the gas analysis. In particular, as the gas emission lines are relatively weak and above a strong stellar background, a small template mismatched can easily bias the [NII]/Hα line ratio.

5.1.2 Gas kinematics

Gas emission lines and particularly [OIII]5007 can be seen in Nburst residuals. We were able to fit it, and the obtained gas velocity map is shown in Figure 5.3. The velocity is very

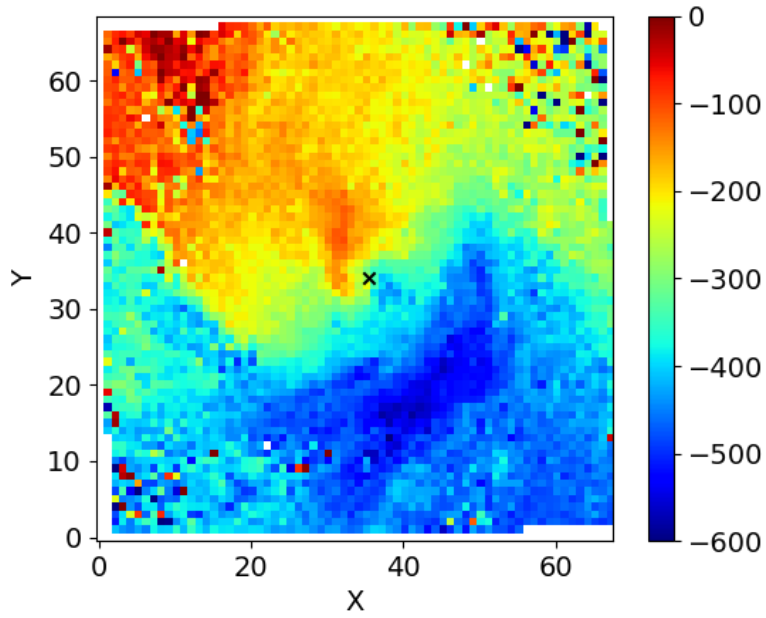

Figure 5.3: Gas Velocity map obtained with the fit of [OIII]5007 emission line on the residuals of Nburst fit. The color-map unit is in km.s^{-1}, and the galaxy center id displayed as a black cross. The kinematic structure is very different than the stellar one.

different than the stellar velocity discussed above. We can identify the S-shape discussed by Opitsch et al. (2017).
We did not performed yet the double emission-line peaks analysis. This requires an optimization of the binning, and an optimal use of the spectral resolution. Depending on the geometry of the emitting regions, coarse binning could introduce some confusion and prevent the detection of several lines. The resolution of the SN2 data cube is less favorable than for the SN3 data cube. This requires to solve the issue of combining the 2 data cubes. The flux estimation of each line will also be difficult. Due to problems encountered to constrain SSP models explained above, the continuum absorption, especially around Hα and Hβ, is not well estimated, and emission-line fluxes can be strongly affected. A careful check of possible template mismatch is also required in order to limit possible systematic effects.

5.2 Further identification of sources

Prichard et al. (2017) identified different types of H_α emitting stars in M31 disc. On the basis of PHAT photometry, they identified five categories of H_α stars: B-type main-sequence (MS) stars, 'transitioning'-MS (T-MS) stars, red core He burning (RHeB) stars, non-C-rich asymptotic giant branch (AGB) stars, and C-rich AGB stars. While we could select sources passing their spectral cuts, it will be difficult to identify our sources on PHAT images, because our SN2 and SN3 filters do not overlap the PHAT filters. A complementary analysis needs to be done to check if it is possible to retrieve some photometry for our

candidates. For each source, the color-magnitude diagram of the region associated to each source should be studied in order to find if it is possible to identify its nature. It will be interesting to confirm if we do detect compact HII regions or H_α stars.
After this work, complementary observations will have to be considered to further identify the candidates detected here. For instance, symbiotic stars are difficult to disentangle from planetary nebulae. In these binary systems, the gas comes from a giant companion instead of the PNe progenitor itself. These binary stars are probably progenitors of type Ia supernovae. Usually, they exhibit a strong Hα and weak or no [NII] and [SII] lines Shara et al. (2017): we have such sources, but we cannot be conclusive about their nature. Mikołajewska et al. (2014) have detected 35 such stars in the main disc, outside the central region. They are characterized by a low [OIII]/Hβ line ratio. These authors use [OIII]4363 to identify them. In principle, symbiotic stars have a Hα magnitude larger than brighter than 21. This is above our sensitivity and we should be able to detect them in the field of view.

5.3 Studying the feed-back of the supermassive black hole

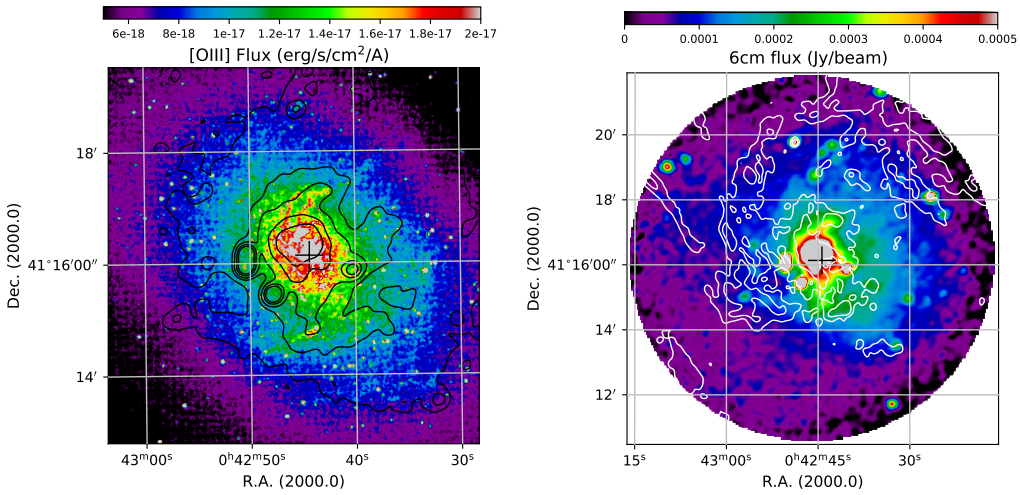

Figure 5.4: Existing observations on the central field of Andromeda. The left panel displays the [OIII] emission detected with SITELLE. The black contours correspond to the 6 cm radio continuum map with contours at 0.1, 0.2, 0.3, 0.45 and 0.6 mJy. We detect [OIII] filaments that ressemble the narrow filamentary structures detected at 20 cm close to Sgr A in the Galactic centre (Yusef-Zadeh et al., 1984) The right panel displays a 6 cm radio continuum map from Gießübel and Beck (2014) with a resolution of 15 arcsec. The white contours correspond to the dust emission at 8 μm from Block et al. (2006) cross corresponds to the position of the black hole. We can note the asymmetry of the radio continuum, the off-centered dust inner ring. The overdensity of gas in the East-South part usually considered to be a shock seems to deliminate the radio continuum emission, which is more extended on the other side. There is a North-South structure in the very center, while the main disk shows a position angle of 35 deg.

A preliminary analysis of the gas emission has been performed. This requires an optimization with Nburst stellar background subtraction, but already provides an overview of

the main features. We have thus discovered structures that evoke filaments and bubbles detected in AGN outflows. Li et al. (2011) discussed that the activity of the actual black hole in the heart of Andromeda is very weak $10^{-10}L_{Edd}$, while they have detected a weak outburst at $10^{-8.5}L_{Edd}$. Given the mass of the black hole ($1.4 \times 10^8 M_{sol}$, Bender et al. (2005)), it is probable that it has known a significant activity in the past. Similarly, the star formation activity is very weak ($0.3M_{sol}$/yr,Rahmani et al. (2016)), and this central part of this galaxy is ideal to investigate a posteriori the mechanisms that quench star formation and the black hole activity. In Figure 5.4, we display existing observations of this region in radio, infrared as well as our [OIII] map in the optical. The region is strongly asymmetric. As discussed by Block et al. (2006), the dust distribution detected at 8μm reveals 2 off-centered rings, possibly due to a frontal collision with M32. Similarly, the radio-continuum measured at 6 cm by Gießübel and Beck (2014) and at 20 cm by Galvin et al. (2012) is shifted towards the North-West direction. It seems that the gas concentrates in an arc, already discussed by Jacoby (1989) as due to shocks, and stops the synchrotron radiation. Radio continuum data suggest that there is a North-South structure (reminiscent of a past jet?), and sub-structures at the limit of sensitivity and resolution.
As displayed in Figure 5.4, the 6 cm (5 GHz) flux is about 0.2 mJy. Gießübel and Beck (2014) have measured the spectral index in the very centre at the level of -0.4 ± 0.03 and then reaches -1. Hoernes et al. (1998) observed a similar behaviour between 6.2 cm and 20 cm. This variation of spectral index is typical of ageing synchrotron emission, as observed on other scales by Carilli and Barthel (1996) for Cygnus A. For the central field of M31, we would thus expect at 150 MHz a flux of 1 to 7 mJy. In addition, this synchrotron spectral ageing could be the consequence of previous AGN activity, i.e. that the M31's black hole had a larger accretion rate in a recent past. Low frequency observations are ideal to explore this past activity. It is probable that these relics are stronger than expected from an extrapolation of the high frequency measurements and benefit from a slope steepening as observed e.g. by Orrù et al. (2010). This steepening is expected due to the loss of energy of the most energetic of the relativistic electrons.
We proposed observations with the international LOFAR instrument in order to identify the true origin of the [OIII] filament and bubble structures, just discovered with the CFHT/SITELLE Fourier spectrograph. It would be the first time this region is sampled in radio continuum with such a resolution. It has been observed previously by Gießübel et al. (2013) at 350 MHz with a 4 arcmin resolution. With a 15" resolution, Gießübel and Beck (2014) have shown that the central regions are decoupled from the rest of the disk, and have a different structure for their magnetic field and dynamos.

Chapter 6

Conclusion

We presented in this thesis the analysis of two spectral data-cubes obtained with the SITELLE instrument at CFHT, centered on the bulge of the Andromeda galaxy. We performed a thorough calibration of the data and developed a sophisticated method to detect emission-line point-like sources.
We used diagnostic diagrams to classify the detections, and identified 766 Planetary Nebulae candidates confirmed with emission-line diagnosis diagrams. This extends previous studies of this field of view by 100%.
The Planetary Nebulae Luminosity Function has been analyzed in details, revealing an unseen so far bimodal population distribution. We show that the cut in magnitude in the PNLF allows to distinguish between two spatially distinct populations. The brighter population shows a disc pattern and is presumably belonging to the disc of Andromeda, while the fainter population is more randomly distributed, indicating it belongs to the bulge. Further kinematic analysis will enable to validate this statement.
Based on the data calibration, we also started the work toward extracting stellar population parameters of M31 bulge. We will be able to compare the kinematics of the stellar background with the bimodal PNe kinematics presented here. We will also be able to revisit in details the presence of a bar as claimed by Opitsch et al. (2017) and to investigate the complex morphology of the different known gas components (inner disc, inner ring). The diffuse gas properties, especially the presumed double kinematic components, will hopefully be assessed. Partial results have already shown the presence of gas filaments that could be linked to the central Black Hole activity, and has led to an observation time proposal with the LOFAR instrument to assess the presence of synchrotron emission near the center of the galaxy.

Acknowledgements

I would like to thank Marcella Carollo for introducing me with Françoise Combes and Anne-Laure Melchior to work on such an insightful project. I would like to particularly thank Anne Laure Melchior, who was truly supportive, patient and a good listener for my proposal on the Project, and who tried to guide me throughout this journey. The exchanges we had on the development of the project made me challenge my way of thinking, but always for good. I thank the LERMA group for hosting me for 6 months at Observatoire de Paris. I was very well welcomed, and I would like to thank everyone for their knowledge-sharing that made my lunch break always so interesting. I am grateful to Igor Chilingarian, Ivan Zolothukin and Ivan Katkov who took time to explain Nburst's functionality and gave a kick start to this Master Thesis. Last, a specially warm thank to Laurent Drissen and Thomas Martin, for their sharing of all the tips about SITELLE instrument. The time spent in Québec with Thomas helped me to unlock so many aspects of the project, that would have stayed gray area otherwise.

Bibliography

Amiri, N. and Darling, J. (2016). Water Masers in the Andromeda Galaxy: II. Where Do Masers Arise? *The Astrophysical Journal*, 826(2):136.

An, J. H., Evans, N. W., Hewett, P., Baillon, P., Calchi Novati, S., Carr, B. J., Crézé, M., Giraud-Héraud, Y., Gould, A., Jetzer, P., Kaplan, J., Kerins, E., Paulin-Henriksson, S., Smartt, S. J., Stalin, C. S., and Tsapras, Y. (2004). The POINT-AGAPE Survey - I. The variable stars in M31. *Monthly Notices of the Royal Astronomical Society*, 351(3):1071–1098.

Azimlu, M., Marciniak, R., and Barmby, P. (2011). A NEW CATALOG OF H II REGIONS IN M31. *The Astronomical Journal*, 142(4):139.

Baldwin, J. A., Phillips, M. M., and Terlevich, R. (1981). Classification parameters for the emission-line spectra of extragalactic objects. *Publications of the Astronomical Society of the Pacific*, 93:5.

Barrows, R. S., Comerford, J. M., Zakamska, N. L., and Cooper, M. C. (2017). Observational Constraints on Correlated Star Formation and Active Galactic Nuclei in Late-stage Galaxy Mergers. *The Astrophysical Journal*, 850(1):27.

Beaton, R. L., Majewski, S. R., Guhathakurta, P., Skrutskie, M. F., Cutri, R. M., Good, J., Patterson, R. J., Athanassoula, E., and Bureau, M. (2007). Unveiling the Boxy Bulge and Bar of the Andromeda Spiral Galaxy. *The Astrophysical Journal*, 658(2):L91–L94.

Bekki, K. (2010). ROTATION AND MULTIPLE STELLAR POPULATION IN GLOBULAR CLUSTERS. *The Astrophysical Journal*, 724(1):L99–L103.

Belfiore, F., Maiolino, R., Maraston, C., Emsellem, E., Bershady, M. A., Masters, K. L., Yan, R., Bizyaev, D., Boquien, M., Brownstein, J. R., Bundy, K., Drory, N., Heckman, T. M., Law, D. R., Roman-Lopes, A., Pan, K., Stanghellini, L., Thomas, D., Weijmans, A.-M., and Westfall, K. B. (2016). SDSS IV MaNGA – spatially resolved diagnostic diagrams: a proof that many galaxies are LIERs. *Monthly Notices of the Royal Astronomical Society*, 461(3):3111–3134.

Bender, R., Kormendy, J., Bower, G., Green, R., Thomas, J., Danks, A. C., Gull, T., Hutchings, J. B., Joseph, C. L., Kaiser, M. E., Lauer, T. R., Nelson, C. H., Richstone, D., Weistrop, D., and Woodgate, B. (2005). HST STIS Spectroscopy of the Triple Nucleus of M31: Two Nested Disks in Keplerian Rotation around a Supermassive Black Hole. *The Astrophysical Journal*, 631(1):280–300.

Block, D. L., Bournaud, F., Combes, F., Groess, R., Barmby, P., Ashby, M. L. N., Fazio, G. G., Pahre, M. A., and Willner, S. P. (2006). An almost head-on collision as the origin of two off-centre rings in the Andromeda galaxy. *Nature*, 443(7113):832–834.

Bradley, L., Sipocz, B., Robitaille, T., Vinícius, Z., Tollerud, E., Deil, C., Barbary, K., Günther, H. M., Cara, M., Busko, I., Droettboom, M., Bostroem, A., Bray, E., Bratholm, L. A., Pickering, T. E., Craig, M., Barentsen, G., Pascual, S., Conseil, S., Adonath, Greco, J., Kerzendorf, W., de Val-Borro, M., StuartLittlefair, Ogaz, S., Lim, P. L., Ferreira, L., D'Eugenio, F., and Weaver, B. A. (2017). astropy/photutils: v0.4.

Braun, R., Thilker, D. A., Walterbos, R. A. M., and Corbelli, E. (2009). A WIDE-FIELD HIGH-RESOLUTION H I MOSAIC OF MESSIER 31. I. OPAQUE ATOMIC GAS AND STAR FORMATION RATE DENSITY. *The Astrophysical Journal*, 695(2):937–953.

Bullock, J. S. and Johnston, K. V. (2005). Tracing Galaxy Formation with Stellar Halos. I. Methods. *The Astrophysical Journal*, 635(2):931–949.

Capaccioli, M., della Valle, M., Rosino, L., and D'Onofrio, M. (1989). Properties of the nova population in M31. *The Astronomical Journal*, 97:1622.

Cappellari, M. (2009). Voronoi binning: Optimal adaptive tessellations of multi-dimensional data.

Cappellari, M. and Emsellem, E. (2004). Parametric Recovery of Line-of-Sight Velocity Distributions from Absorption-Line Spectra of Galaxies via Penalized Likelihood. *Publications of the Astronomical Society of the Pacific*, 116(816):138–147.

Carilli, C. and Barthel, P. (1996). Cygnus A. *Astronomy and Astrophysics Review*, 7(1):1–54.

Carnall, A. C., McLure, R. J., Dunlop, J. S., and Davé, R. (2017). Inferring the star-formation histories of massive quiescent galaxies with BAGPIPES: Evidence for multiple quenching mechanisms. *ArXiv e-prints*.

Chemin, L., Carignan, C., and Foster, T. (2009). H I KINEMATICS AND DYNAMICS OF MESSIER 31. *The Astrophysical Journal*, 705(2):1395–1415.

Chilingarian, I., Prugniel, P., Sil'Chenko, O., and Koleva, M. (2006). NBursts: Simultaneous extraction of internal kinematics and parametrized SFH from integrated light spectra. *Proceedings of the International Astronomical Union*, 2(S241):175–176.

Chilingarian, I. V., Zolotukhin, I. Y., Katkov, I. Y., Melchior, A.-L., Rubtsov, E. V., and Grishin, K. A. (2017). RCSED—A Value-added Reference Catalog of Spectral Energy Distributions of 800,299 Galaxies in 11 Ultraviolet, Optical, and Near-infrared Bands: Morphologies, Colors, Ionized Gas, and Stellar Population Properties. *The Astrophysical Journal Supplement Series*, 228(2):14.

Ciardullo, R. (2010). The Planetary Nebula Luminosity Function: Pieces of the Puzzle. *Publications of the Astronomical Society of Australia*, 27(02):149–155.

Ciardullo, R. (2012). The Planetary Nebula Luminosity Function at the dawn of Gaia. *Astrophysics and Space Science*, 341(1):151–161.

Ciardullo, R., Ford, H. C., Neill, J. D., Jacoby, G. H., and Shafter, A. W. (1987). THE SPATIAL DISTRIBUTION AND POPULATION OF NOVAE IN M31. *The Astrophysical Journal*, 318:520–530.

Ciardullo, R., Jacoby, G. H., Ford, H. C., and Neill, J. D. (1989). Planetary nebulae as standard candles. II - The calibration in M31 and its companions. *The Astrophysical Journal*, 339:53.

Ciardullo, R., Sigurdsson, S., Feldmeier, J. J., and Jacoby, G. H. (2005). Close Binaries as the Progenitors of the Brightest Planetary Nebulae. *The Astrophysical Journal*, 629(1):499–506.

Coenda, V., Martínez, H. J., and Muriel, H. (2018). Green valley galaxies as a transition population in different environments. *Monthly Notices of the Royal Astronomical Society*, 473(4):5617–5629.

Concas, A., Popesso, P., Brusa, M., Mainieri, V., Erfanianfar, G., and Morselli, L. (2017). Light breeze in the local Universe. *Astronomy & Astrophysics*, 606:A36.

Corbelli, E., Lorenzoni, S., Walterbos, R., Braun, R., and Thilker, D. (2010). A wide-field H I mosaic of Messier 31. *Astronomy and Astrophysics*, 511:A89.

Courteau, S., Widrow, L. M., McDonald, M., Guhathakurta, P., Gilbert, K. M., Zhu, Y., Beaton, R. L., and Majewski, S. R. (2011). THE LUMINOSITY PROFILE AND STRUCTURAL PARAMETERS OF THE ANDROMEDA GALAXY. *The Astrophysical Journal*, 739(1):20.

Crane, P. C., Dickel, J. R., and Cowan, J. J. (1992). Detection of an unresolved nuclear radio source in M31. *The Astrophysical Journal*, 390:L9.

Crotts, A. P. S. (1992). M31 - A unique laboratory for gravitational microlensing. *The Astrophysical Journal*, 399:L43.

Davis, B. D., Ciardullo, R., Feldmeier, J. J., and Jacoby, G. H. (2018). The Planetary Nebula Luminosity Function (PNLF): Contamination from Supernova Remnants. *Research Notes of the AAS*, 2(1):32.

de Grijs, R. and Bono, G. (2014). CLUSTERING OF LOCAL GROUP DISTANCES: PUBLICATION BIAS OR CORRELATED MEASUREMENTS? II. M31 AND BEYOND. *The Astronomical Journal*, 148(1):17.

de VAUCOULEURS, G. (1958). The Local Supercluster of Galaxies. *Nature*, 182(4648):1478–1480.

Dong, H., Li, Z., Wang, Q. D., Lauer, T. R., Olsen, K. A. G., Saha, A., Dalcanton, J. J., and Williams, B. F. (2015). Photometric evidence of an intermediate-age stellar population in the inner bulge of M31. *Monthly Notices of the Royal Astronomical Society*, 451(4):4126–4138.

Drissen, L., Bernier, A.-P., Rousseau-Nepton, L., Alarie, A., Robert, C., Joncas, G., Thibault, S., and Grandmont, F. (2010). SITELLE: a wide-field imaging Fourier transform spectrometer for the Canada-France-Hawaii Telescope. *SPIE Astronomical Telescopes + Instrumentation*, 7735(July 2010):77350B–77350B–10.

Driver, S. P., Hill, D. T., Kelvin, L. S., Robotham, A. S. G., Liske, J., Norberg, P., Baldry, I. K., Bamford, S. P., Hopkins, A. M., Loveday, J., Peacock, J. A., Andrae, E., Bland-Hawthorn, J., Brough, S., Brown, M. J. I., Cameron, E., Ching, J. H. Y., Colless, M., Conselice, C. J., Croom, S. M., Cross, N. J. G., De Propris, R., Dye, S., Drinkwater, M. J., Ellis, S., Graham, A. W., Grootes, M. W., Gunawardhana, M., Jones, D. H., van Kampen, E., Maraston, C., Nichol, R. C., Parkinson, H. R., Phillipps, S., Pimbblet, K., Popescu, C. C., Prescott, M., Roseboom, I. G., Sadler, E. M., Sansom, A. E., Sharp, R. G., Smith, D. J. B., Taylor, E., Thomas, D., Tuffs, R. J., Wijesinghe, D., Dunne, L., Frenk, C. S., Jarvis, M. J., Madore, B. F., Meyer, M. J., Seibert, M., Staveley-Smith, L., Sutherland, W. J., and Warren, S. J. (2011). Galaxy and Mass Assembly (GAMA): survey diagnostics and core data release. *Monthly Notices of the Royal Astronomical Society*, 413(2):971–995.

Fang, J. J., Faber, S. M., Koo, D. C., and Dekel, A. (2013). A LINK BETWEEN STAR FORMATION QUENCHING AND INNER STELLAR MASS DENSITY IN SLOAN DIGITAL SKY SURVEY CENTRAL GALAXIES. *The Astrophysical Journal*, 776(1):63.

Fardal, M. A., Weinberg, M. D., Babul, A., Irwin, M. J., Guhathakurta, P., Gilbert, K. M., Ferguson, A. M. N., Ibata, R. A., Lewis, G. F., Tanvir, N. R., and Huxor, A. P. (2013). Inferring the Andromeda Galaxy's mass from its giant southern stream with Bayesian simulation sampling. *Monthly Notices of the Royal Astronomical Society*, 434(4):2779–2802.

Feldmeier, J. J., Ciardullo, R., and Jacoby, G. H. (1997). Planetary Nebulae as Standard Candles. XI. Application to Spiral Galaxies. *The Astrophysical Journal*, 479(1):231–243.

Ford, G. P., Gear, W. K., Smith, M. W. L., Eales, S. A., Baes, M., Bendo, G. J., Boquien, M., Boselli, A., Cooray, A. R., De Looze, I., Fritz, J., Gentile, G., Gomez, H. L., Gordon, K. D., Kirk, J., Lebouteiller, V., O'Halloran, B., Spinoglio, L., Verstappen, J., and Wilson, C. D. (2013). HERSCHEL EXPLOITATION OF LOCAL GALAXY ANDROMEDA (HELGA). III. THE STAR FORMATION LAW IN M31. *The Astrophysical Journal*, 769(1):55.

Fraser-McKelvie, A., Brown, M. J. I., Pimbblet, K., Dolley, T., and Bonne, N. J. (2018). Multiple mechanisms quench passive spiral galaxies. *Monthly Notices of the Royal Astronomical Society*, 474(2):1909–1921.

Freedman, W. L. (2000). The Hubble constant and the expansion age of the Universe. *Physics Reports*, 333-334:13–31.

Frew, D. J. and Parker, Q. A. (2010). Planetary Nebulae: Observational Properties, Mimics and Diagnostics. *Publications of the Astronomical Society of Australia*, 27(02):129–148.

Gaia Collaboration (2016). Gaia Data Release 1. *Astronomy & Astrophysics*, 595:A2.

Galvin, T., Filipovic, M., Crawford, E., Tothill, N., Wong, G., and De Horta, A. (2012). 20 cm VLA Radio-Continuum Study of M31 - Images and Point Source Catalogues. *Serbian Astronomical Journal*, 184:41–68.

Gießübel, R. and Beck, R. (2014). The magnetic field structure of the central region in M 31. *Astronomy & Astrophysics*, 571:A61.

Gießübel, R., Heald, G., Beck, R., and Arshakian, T. G. (2013). Polarized synchrotron radiation from the Andromeda galaxy M 31 and background sources at 350 MHz. *Astronomy & Astrophysics*, 559:A27.

Greisen, E. W. and Calabretta, M. R. (2002). Representations of world coordinates in FITS. *Astronomy & Astrophysics*, 395(3):1061–1075.

Halliday, C., Carter, D., Bridges, T. J., Jackson, Z. C., Wilkinson, M. I., Quinn, D. P., Evans, N. W., Douglas, N. G., Merrett, H. R., Merrifield, M. R., Romanowsky, A. J., Kuijken, K., and Irwin, M. J. (2006). Planetary nebula velocities in the disc and bulge of M31. *Monthly Notices of the Royal Astronomical Society*, 369(1):97–119.

Hammer, F., Yang, Y. B., Wang, J. L., Ibata, R., Flores, H., and Puech, M. (2018). A 2-3 billion year old major merger paradigm for the Andromeda galaxy and its outskirts. *Monthly Notices of the Royal Astronomical Society*, 15(January):1–15.

Hatfield, P. W. and Jarvis, M. J. (2017). Environmental quenching and galactic conformity in the galaxy cross-correlation signal. *Monthly Notices of the Royal Astronomical Society*, 472(3):3570–3588.

Herrmann, K. A., Ciardullo, R., Feldmeier, J. J., and Vinciguerra, M. (2008). Planetary Nebulae in Face-On Spiral Galaxies. I. Planetary Nebula Photometry and Distances. *The Astrophysical Journal*, 683(2):630–643.

Hoernes, P., Berkhuijsen, E., and Xu, C. (1998). Radio-FIR correlations within M 31. *Astronomy and Astrophysics*, 334:57–70.

Jacoby, G. H. (1989). Planetary nebulae as standard candles. I - Evolutionary models. *The Astrophysical Journal*, 339:39.

Jacoby, G. H. and De Marco, O. (2002). A Survey for Very Faint Planetary Nebulae in the SMC. I. Identification, Confirmation, and Preliminary Analysis. *The Astronomical Journal*, 123(1):269–278.

Kang, Y., Rey, S.-C., Bianchi, L., Lee, K., Kim, Y., and Sohn, S. T. (2011). A Comprehensive GALEX Ultraviolet Catalog of Star Clusters in M31 and a Study of the Young Clusters. *The Astrophysical Journal Supplement Series*, 199(2):37.

Kauffmann, G., Heckman, T. M., Tremonti, C., Brinchmann, J., Charlot, S., White, S. D. M., Ridgway, S. E., Brinkmann, J., Fukugita, M., Hall, P. B., Ivezić, Ž., Richards, G. T., and Schneider, D. P. (2003). The host galaxies of active galactic nuclei. *Monthly Notices of the Royal Astronomical Society*, 346(4):1055–1077.

Kaviraj, S., Shabala, S. S., Deller, A. T., and Middelberg, E. (2015). The triggering of local AGN and their role in regulating star formation. *Monthly Notices of the Royal Astronomical Society*, 452(1):774–783.

Kerins, E., Carr, B. J., Evans, N. W., Hewett, P., Lastennet, E., Le Du, Y., Melchior, A.-L., Smartt, S. J., and Valls-Gabaud, D. (2001). Theory of pixel lensing towards M31 – I. The density contribution and mass of MACHOs. *Monthly Notices of the Royal Astronomical Society*, 323(1):13–33.

Kerins, E., Darnley, M. J., Duke, J. P., Gould, A., Han, C., Jeon, Y.-B., Newsam, A., and Park, B.-G. (2006). The Angstrom Project: a microlensing survey of the structure and composition of the bulge of the Andromeda galaxy. *Monthly Notices of the Royal Astronomical Society*, 365(4):1099–1108.

Kewley, L. J., Dopita, M. A., Sutherland, R. S., Heisler, C. A., and Trevena, J. (2001). Theoretical Modeling of Starburst Galaxies. *The Astrophysical Journal*, 556(1):121–140.

Kingsburgh, R. L. and Barlow, M. J. (1994). Elemental abundances for a sample of southern galctic planetary nebulae. *Monthly Notices of the Royal Astronomical Society*, 271(2):257–299.

Kirihara, T., Miki, Y., and Mori, M. (2014). Puzzling outer-density profile of the dark matter halo in the Andromeda galaxy. *Publications of the Astronomical Society of Japan*, 66(6):L10.

Kniazev, A. Y., Pustilnik, S. A., and Zucker, D. B. (2008). Spectroscopy of two PN candidates in IC 10. *Monthly Notices of the Royal Astronomical Society*, 384(3):1045–1052.

Koleva, M., Prugniel, P., Ocvirk, P., Le Borgne, D., and Soubiran, C. (2008). Spectroscopic ages and metallicities of stellar populations: validation of full spectrum fitting. *Monthly Notices of the Royal Astronomical Society*, 385(4):1998–2010.

Komiyama, Y., Chiba, M., Tanaka, M., Tanaka, M., Kirihara, T., Miki, Y., Mori, M., Lupton, R. H., Guhathakurta, P., Kalirai, J. S., Gilbert, K., Kirby, E., Lee, M. G., Jang, I. S., Sharma, S., and Hayashi, K. (2018). Stellar Stream and Halo Structure in the Andromeda Galaxy from a Subaru/Hyper Suprime-Cam Survey. *The Astrophysical Journal*, 853(1):29.

Lauer, T. R., Faber, S. M., Groth, E. J., Shaya, E. J., Campbell, B., Code, A., Currie, D. G., Baum, W. A., Ewald, S. P., Hester, J. J., Holtzman, J. A., Kristian, J., Light, R. M., Ligynds, C. R., O'Neil, E. J., J., and Westphal, J. A. (1993). Planetary camera observations of the double nucleus of M31. *The Astronomical Journal*, 106:1436.

Le Borgne, D., Rocca-Volmerange, B., Prugniel, P., Lançon, A., Fioc, M., and Soubiran, C. (2004). Evolutionary synthesis of galaxies at high spectral resolution with the code PEGASE-HR. *Astronomy & Astrophysics*, 425(3):881–897.

Lee, J. H. and Lee, M. G. (2014). A NEW OPTICAL SURVEY OF SUPERNOVA REMNANT CANDIDATES IN M31. *The Astrophysical Journal*, 786(2):130.

Leisy, P., Corradi, R. L. M., Magrini, L., Greimel, R., Mampaso, A., and Dennefeld, M. (2005). Planetary nebulae in the dwarf galaxy NGC 6822: Detection of new candidates. *Astronomy & Astrophysics*, 436(2):437–442.

Li, Z., Garcia, M. R., Forman, W. R., Jones, C., Kraft, R. P., Lal, D. V., Murray, S. S., and Wang, Q. D. (2011). THE MURMUR OF THE HIDDEN MONSTER: CHANDRA 'S DECADAL VIEW OF THE SUPERMASSIVE BLACK HOLE IN M31. *The Astrophysical Journal*, 728(1):L10.

Lilly, S. J., Fevre, O. L., Renzini, A., Zamorani, G., Scodeggio, M., Contini, T., Carollo, C. M., Hasinger, G., Kneib, J.-P., Iovino, A., Le Brun, V., Maier, C., Mainieri, V., Mignoli, M., Silverman, J., Tasca, L. A. M., Bolzonella, M., Bongiorno, A., Bottini, D., Capak, P., Caputi, K., Cimatti, A., Cucciati, O., Daddi, E., Feldmann, R., Franzetti, P., Garilli, B., Guzzo, L., Ilbert, O., Kampczyk, P., Kovac, K., Lamareille, F., Leauthaud, A., Borgne, J. L., McCracken, H. J., Marinoni, C., Pello, R., Ricciardelli, E., Scarlata, C., Vergani, D., Sanders, D. B., Schinnerer, E., Scoville, N., Taniguchi, Y., Arnouts, S., Aussel, H., Bardelli, S., Brusa, M., Cappi, A., Ciliegi, P., Finoguenov, A., Foucaud, S., Franceschini, R., Halliday, C., Impey, C., Knobel, C., Koekemoer, A., Kurk, J., Maccagni, D., Maddox, S., Marano, B., Marconi, G., Meneux, B., Mobasher, B., Moreau, C., Peacock, J. A., Porciani, C., Pozzetti, L., Scaramella, R., Schiminovich, D., Shopbell, P., Smail, I., Thompson, D., Tresse, L., Vettolani, G., Zanichelli, A., and Zucca, E. (2007). zCOSMOS: A Large VLT/VIMOS Redshift Survey Covering $0 < z < 3$ in the COSMOS Field. *The Astrophysical Journal Supplement Series*, 172(1):70–85.

Madau, P. and Dickinson, M. (2014). Cosmic Star-Formation History. *Annual Review of Astronomy and Astrophysics*, 52(1):415–486.

Maillard, J. P., Drissen, L., Grandmont, F., and Thibault, S. (2013). Integral wide-field spectroscopy in astronomy: The Imaging FTS solution. *Experimental Astronomy*, 35(3):527–559.

Marigo, P., Girardi, L., Weiss, A., Groenewegen, M. A. T., and Chiosi, C. (2004). Evolution of planetary nebulae. *Astronomy & Astrophysics*, 423(3):995–1015.

Martin, T. and Drissen, L. (2017). Calibrations of SITELLE's first data release. *MNRAS*, 13(June):1–13.

Martin, T., Drissen, L., and Joncas, G. (2015). ORBS, ORCS, OACS, a Software Suite for Data Reduction and Analysis of the Hyperspectral Imagers SITELLE and SpIOMM. *Astronomical Data Analysis Software an Systems XXIV (ADASS XXIV)*, 495:327.

Martin, T. B., Drissen, L., and Melchior, A.-L. (2018). A SITELLE view of M31's central region – I. Calibrations and radial velocity catalogue of nearly 800 emission-line point-like sources. *Monthly Notices of the Royal Astronomical Society*, 473(3):4130–4149.

McConnachie, A. W., Irwin, M. J., Ibata, R. A., Dubinski, J., Widrow, L. M., Martin, N. F., Côté, P., Dotter, A. L., Navarro, J. F., Ferguson, A. M. N., Puzia, T. H., Lewis, G. F., Babul, A., Barmby, P., Bienaymé, O., Chapman, S. C., Cockcroft, R., Collins, M. L. M., Fardal, M. A., Harris, W. E., Huxor, A., Mackey, A. D., Peñarrubia, J., Rich, R. M., Richer, H. B., Siebert, A., Tanvir, N., Valls-Gabaud, D., and Venn, K. A. (2009). The remnants of galaxy formation from a panoramic survey of the region around M31. *Nature*, 461(7260):66–69.

Melchior, A.-L. and Combes, F. (2011). Molecular gas in the inner 0.7 kpc-radius ring of M 31. *Astronomy & Astrophysics*, 536:A52.

Melchior, A.-L. and Combes, F. (2016). Dense gas tracing the collisional past of Andromeda. *Astronomy & Astrophysics*, 585:A44.

Melchior, A.-L. and Combes, F. (2017). Exhaustion of the gas next to M31's supermassive black hole. *Astronomy & Astrophysics*, 607:L7.

Melchior, A.-L., Viallefond, F., Guelin, M., and Neininger, N. (2000). Detection of CO in the inner part of the bulge of M31. *Monthly Notices of the Royal Astronomical Society*, 312(3):L29–L33.

Merrett, H. R., Merrifield, M. R., Douglas, N. G., Kuijken, K., Romanowsky, A. J., Napolitano, N. R., Arnaboldi, M., Capaccioli, M., Freeman, K. C., Gerhard, O., Coccato, L., Carter, D., Evans, N. W., Wilkinson, M. I., Halliday, C., and Bridges, T. J. (2006). A deep kinematic survey of planetary nebulae in the Andromeda galaxy using the Planetary Nebula Spectrograph. *Monthly Notices of the Royal Astronomical Society*, 369(1):120–142.

Merritt, D., Ferrarese, L., and Joseph, C. L. (2001). No Supermassive Black Hole in M33? *Science*, 293(5532):1116–1118.

Miki, Y., Mori, M., and Rich, R. M. (2016). COLLISION TOMOGRAPHY: PHYSICAL PROPERTIES OF POSSIBLE PROGENITORS OF THE ANDROMEDA STELLAR STREAM. *The Astrophysical Journal*, 827(1):82.

Mikołajewska, J., Caldwell, N., and Shara, M. M. (2014). First detection and characterization of symbiotic stars in M31. *Monthly Notices of the Royal Astronomical Society*, 444(1):586–599.

Mould, J. (2013). The Bulge of M31. *Publications of the Astronomical Society of Australia*, 30:e027.

Mutch, S. J., Croton, D. J., and Poole, G. B. (2011). THE MID-LIFE CRISIS OF THE MILKY WAY AND M31. *The Astrophysical Journal*, 736(2):84.

Nieten, C., Neininger, N., Guélin, M., Ungerechts, H., Lucas, R., Berkhuijsen, E. M., Beck, R., and Wielebinski, R. (2006). Molecular gas in the Andromeda galaxy. *Astronomy & Astrophysics*, 453(2):459–475.

Noll, R. J. (1976). Zernike polynomials and atmospheric turbulence. *Journal of the Optical Society of America*, 66(3):207.

Opitsch, M., Fabricius, M. H., Saglia, R. P., Bender, R., Blaña, M., and Gerhard, O. (2017). Evidence for non-axisymmetry in M31 from wide-field kinematics of stars and gas.

Orrù, E., Murgia, M., Feretti, L., Govoni, F., Giovannini, G., Lane, W., Kassim, N., and Paladino, R. (2010). Low-frequency study of two giant radio galaxies: 3C 35 and 3C 223. *Astronomy and Astrophysics*, 515:A50.

Parker, Q. A., Acker, A., Frew, D. J., Hartley, M., Peyaud, A. E. J., Ochsenbein, F., Phillipps, S., Russeil, D., Beaulieu, S. F., Cohen, M., Koppen, J., Miszalski, B., Morgan, D. H., Morris, R. A. H., Pierce, M. J., and Vaughan, A. E. (2006). The Macquarie/AAO/Strasbourg H Planetary Nebula Catalogue: MASH. *Monthly Notices of the Royal Astronomical Society*, 373(1):79–94.

Prichard, L. J., Guhathakurta, P., Hamren, K. M., Dalcanton, J. J., Dorman, C. E., Seth, A. C., Williams, B. F., Damon, G. A., Ilango, A., and Ilango, M. (2017). Emission-line stars in M31 from the SPLASH and PHAT surveys. *Monthly Notices of the Royal Astronomical Society*, 465(4):4180–4203.

Rahmani, S., Lianou, S., and Barmby, P. (2016). Star formation laws in the Andromeda galaxy: gas, stars, metals and the surface density of star formation. *Monthly Notices of the Royal Astronomical Society*, 456(4):4128–4144.

Reid, W. A. and Parker, Q. A. (2010). A new population of planetary nebulae discovered in the Large Magellanic Cloud - III. The luminosity function. *Monthly Notices of the Royal Astronomical Society*, 405:no–no.

Rodríguez-González, A., Hernández-Martínez, L., Esquivel, A., Raga, A. C., Stasińska, G., Peña, M., and Mayya, Y. D. (2015). A two-mode planetary nebula luminosity function. *Astronomy & Astrophysics*, 575:A1.

Sabbadin, F., Minello, S., and Bianchini, A. (1977). Sharpless 176: a large, nearby planetary nebula. *Astronomy and Astrophysics*, 60:147–149.

Sadoun, R., Mohayaee, R., and Colin, J. (2014). A single-merger scenario for the formation of the giant stream and the warp of M31. *Monthly Notices of the Royal Astronomical Society*, 442(1):160–175.

Saglia, R. P., Fabricius, M., Bender, R., Montalto, M., Lee, C.-H., Riffeser, A., Seitz, S., Morganti, L., Gerhard, O., and Hopp, U. (2010). The old and heavy bulge of M 31. *Astronomy and Astrophysics*, 509:A61.

Schlegel, D., Finkbeiner, D., and Davis, M. (1997). Maps of Dust IR Emission for Use in Estimation of Reddening and CMBR Foregrounds. In *American Astronomical Society Meeting Abstracts*, volume 29 of *Bulletin of the American Astronomical Society*, page 1354.

Shafter, A. W. and Irby, B. K. (2001). On the Spatial Distribution, Stellar Population, and Rate of Novae in M31. *The Astrophysical Journal*, 563(2):749–767.

Shara, M. M., Drissen, L., Martin, T., Alarie, A., and Richard Stephenson, F. (2017). When does an old nova become a dwarf nova? Kinematics and age of the nova shell of the dwarf nova AT Cancri. *Monthly Notices of the Royal Astronomical Society*, 465(1):739–745.

Shupe, D. L., Moshir, M., Li, J., Makovoz, D., Narron, R., and Hook, R. N. (2005). The SIP Convention for Representing Distortion in FITS Image Headers. *Astronomical Data Analysis Software and Systems XIV ASP Conference Series*, 347.

Stetson, P. B. (1987). DAOPHOT - A computer program for crowded-field stellar photometry. *Publications of the Astronomical Society of the Pacific*, 99:191.

Tody, D. (1993). IRAF in the Nineties. In Hanisch, R., Brissenden, R., and Barnes, J., editors, *Astronomical Data Analysis Software and Systems II*, volume 52 of *Astronomical Society of the Pacific Conference Series*, page 173.

Urquhart, J. S., Thompson, M. A., Moore, T. J. T., Purcell, C. R., Hoare, M. G., Schuller, F., Wyrowski, F., Csengeri, T., Menten, K. M., Lumsden, S. L., Kurtz, S., Walmsley, C. M., Bronfman, L., Morgan, L. K., Eden, D. J., and Russeil, D. (2013). ATLASGAL — properties of compact HII regions and their natal clumps. *Monthly Notices of the Royal Astronomical Society*, 435(1):400–428.

Woo, J.-H., Son, D., and Bae, H.-J. (2017). Delayed or No Feedback? Gas Outflows in Type 2 AGNs. III. *The Astrophysical Journal*, 839(2):120.

York, D. G., Adelman, J., Anderson, Jr., J. E., Anderson, S. F., Annis, J., Bahcall, N. A., Bakken, J. A., Barkhouser, R., Bastian, S., Berman, E., Boroski, W. N., Bracker, S., Briegel, C., Briggs, J. W., Brinkmann, J., Brunner, R., Burles, S., Carey, L., Carr, M. A., Castander, F. J., Chen, B., Colestock, P. L., Connolly, A. J., Crocker, J. H., Csabai, I., Czarapata, P. C., Davis, J. E., Doi, M., Dombeck, T., Eisenstein, D., Ellman, N., Elms, B. R., Evans, M. L., Fan, X., Federwitz, G. R., Fiscelli, L., Friedman, S., Frieman, J. A., Fukugita, M., Gillespie, B., Gunn, J. E., Gurbani, V. K., de Haas, E., Haldeman, M., Harris, F. H., Hayes, J., Heckman, T. M., Hennessy, G. S., Hindsley, R. B., Holm, S., Holmgren, D. J., Huang, C.-h., Hull, C., Husby, D., Ichikawa, S.-I., Ichikawa, T., Ivezić, Ž., Kent, S., Kim, R. S. J., Kinney, E., Klaene, M., Kleinman, A. N., Kleinman, S., Knapp, G. R., Korienek, J., Kron, R. G., Kunszt, P. Z., Lamb, D. Q., Lee, B., Leger, R. F., Limmongkol, S., Lindenmeyer, C., Long, D. C., Loomis, C., Loveday, J., Lucinio, R., Lupton, R. H., MacKinnon, B., Mannery, E. J., Mantsch, P. M., Margon, B., McGehee, P., McKay, T. A., Meiksin, A., Merelli, A., Monet, D. G., Munn, J. A., Narayanan, V. K., Nash, T., Neilsen, E., Neswold, R., Newberg, H. J., Nichol, R. C., Nicinski, T., Nonino, M., Okada, N., Okamura, S., Ostriker, J. P., Owen, R., Pauls, A. G., Peoples, J., Peterson, R. L., Petravick, D., Pier, J. R., Pope, A., Pordes, R., Prosapio, A., Rechenmacher, R., Quinn, T. R., Richards, G. T., Richmond, M. W., Rivetta, C. H., Rockosi, C. M., Ruthmansdorfer, K., Sandford, D., Schlegel, D. J., Schneider, D. P., Sekiguchi, M., Sergey, G., Shimasaku, K., Siegmund, W. A., Smee, S., Smith, J. A., Snedden, S., Stone, R., Stoughton, C., Strauss, M. A., Stubbs, C., SubbaRao, M., Szalay, A. S., Szapudi, I., Szokoly, G. P., Thakar, A. R., Tremonti, C., Tucker, D. L., Uomoto, A., Vanden Berk, D., Vogeley, M. S., Waddell, P., Wang, S.-i., Watanabe, M., Weinberg, D. H., Yanny, B., and Yasuda, N. (2000). The Sloan Digital Sky Survey: Technical Summary. *The Astronomical Journal*, 120(3):1579–1587.

Yusef-Zadeh, F., Morris, M., and Chance, D. (1984). Large, highly organized radio structures near the galactic centre. *Nature*, 310(5978):557–561.